申报	系列：教学科研
	专业：农业工程
	职称：副教授

业绩成果材料

（申报人的业绩成果材料包括论文、科研项目、获奖以及其他成果等）

单　位（二级单位）__数学与信息学院__

姓　名　　**张素敏**

材料核对人：　　单位盖章：

核对时间：

华南农业大学制

目　录

一、教学研究业绩

1.教改论文：乡村振兴背景下新农科人才计算机应用能力培养路径研究 5

2.教改论文：基于“互联网+”和 AI 的非计算机类本科专业“Java 语言程序设计”课程的改革与实践..... 15

二、科研项目

1.主持：

1.1 智慧牧场监测应用示范项目的立项通知（合同）及有关佐证材料 22

1.2 基于视频跟踪的泄露气体监测与报警项目的立项通知（合同）及有关佐证材料 25

2.主参：

2.1 主参：大规模无线传感网络可维护性理论初探 32

2.2.主参：牲畜非接触式智能识别技术研究与示范..... 33

三、论文、著作等

1.检索证明 34

2.以第一作者发表本专业论文情况

2.1. On the Equivalence of HLLE and LTSA 36

2.2. Pig body weight prediction based on weight waveform graph 49

3.以通讯作者发表本专业论文情况

3.1.Point cloud-based pig body size measurement featured by standard 66

四、科研成果

1.知识产权
1.1.专利授权证书：一种牲畜表面点云智能分割方法及其系统 78
1.2 专利授权证书：一种基于椭圆拟合的原木板材孔洞缺陷检测与定位方法 80
1.3 专利授权证书：一种基于原木弯曲度的木材切分点定位方法和装置 82
1.4 专利授权证书：基于色彩化点云多视角关键点定位的牛只体尺测量方法 84
1.5 专利授权证书：一种基于双目光学图像的水下三维全景重构方法和系统 85
1.6 专利授权证书：一种牲畜体重测量方法、装置、系统及计算机设备 86
1.7 专利授权证书：一种基于三维曲面的原木直径测算方法 87
1.8 专利授权证书：一种区域限定的改进三次 B 样条插值修补方法 89
1.9 专利授权证书：一种基于深度学习的仔猪乳头计数方法 91
1.10 专利授权证书：一种基于三维重构牲畜体点云的标准姿态鉴定方法 93
1.11 专利授权证书：一种牲畜体积计算方法、系统、可读存储介质 95
1.12 软件著作权：基于多传感的全方位牲畜智测系统 ... 97
2.专利转化合同 98

五、其他业绩

1.指导学生学科竞赛
1.1.第九届互联网省赛银奖 112
1.2 第十六届蓝桥杯全国软件和信息技术专业人才大赛广东赛区 C/C++程序设计大学 B 组二等奖 113
1.3 第十六届蓝桥杯全国软件和信息技术专业人才大赛广东赛区 C/C++程序设计大学 B 组三等奖 117
2.个人荣誉
2.1.优秀班主任证书 119

农业科技与信息

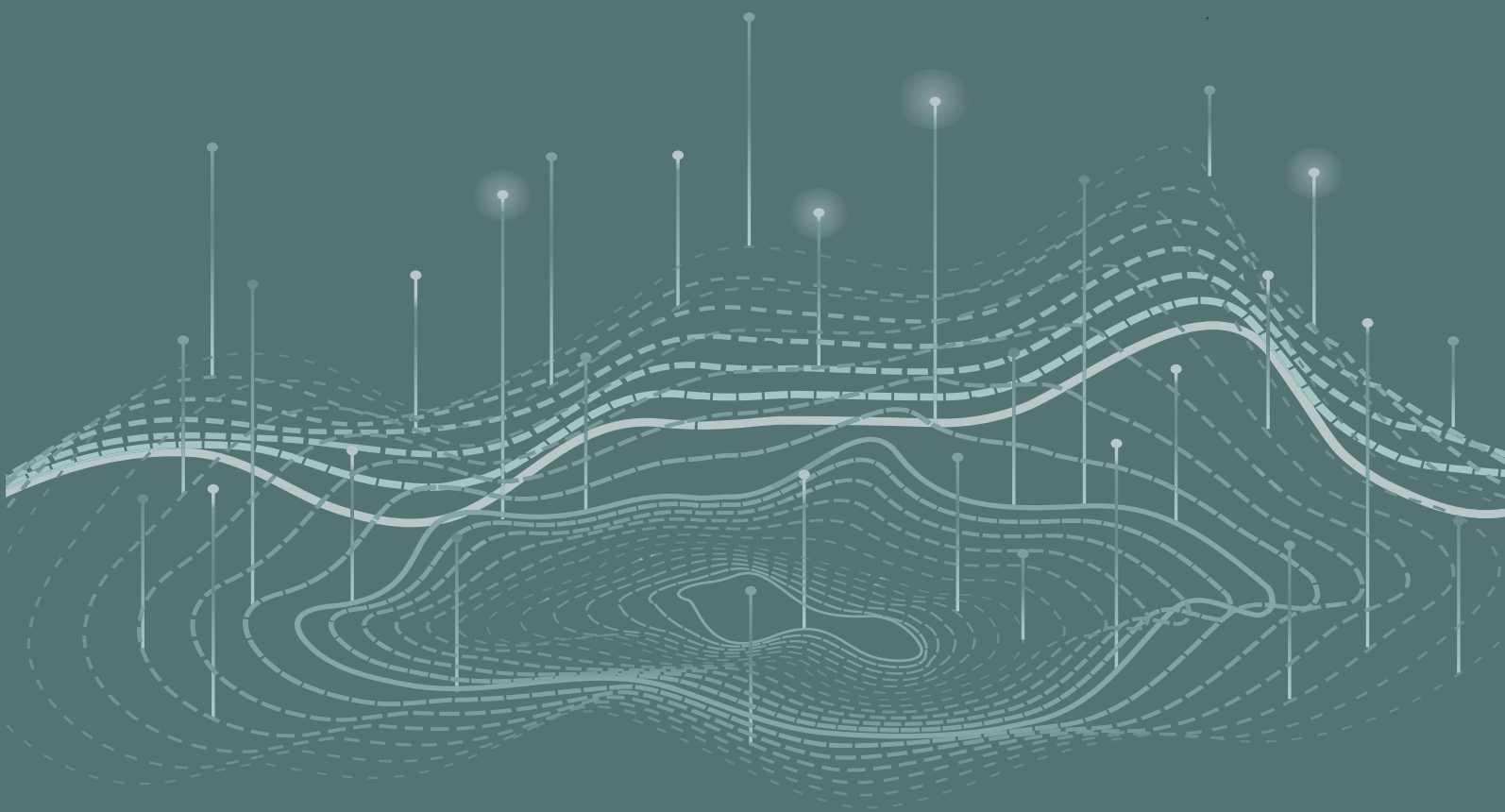
甘肃省农业农村厅 主管
甘肃农业杂志社 主办

中文科技期刊数据库（全文版）收录期刊
中国知网全文收录期刊

ISSN 1003-6997
CN 62-1057/S

农业科技与信息

Agricultural Science-technology and Information



二〇二四年第十二期 总第六七七期

ISSN 1003-6997
12>
9 771003 699249

2024年12月
第12期 总第677期

主管：甘肃省农业农村厅
主办：甘肃农业杂志社
出版：《农业科技与信息》编辑部
1984年创刊

国际标准连续出版物号：ISSN 1003-6997
国内统一连续出版物号：CN 62-1057/S
中文科技期刊数据库（全文版）收录期刊
中国知网全文收录期刊

学术编委会

主　任：赵贵宾
编　委：文　霞　齐广平　刘长仲　李世成
李　彤　李含琳　李城德　张仁陟
张保军　张　富　赵武云　晋小军
徐秉良　柴　强　颉建明　韩舜愈
窦学诚　翟丹云
（以姓氏笔画排名）

投稿邮箱：nykjyxx@126.com
投稿网址：www.gsqikan.com
印　刷：甘肃新秦艺数字印刷有限公司
发　行：甘肃省邮政公司
（全国各地邮政公司均可订阅）
邮发代号：54-60
定　价：25元/期；300元/年
广告发布登记编号：620100013
地　址：甘肃省兰州市城关区武都路498号
邮政编码：730030
开户银行：中国农业银行兰州金穗支行
户　名：甘肃农业出版传媒有限公司
账　号：27011501040006458
出版日期：2024年12月30日

农业科技与信息

Agricultural Science-technology and Information

2024年第12期（总第677期）　月刊

总 编 辑：刘国华
执行主编：魏　翔
编辑部主任：张琼琼
本期责编：祁凡琳
编　　辑：祁凡琳　赵怀霞　魏　薇
校　　对：张　璐
本期美编：黄志勇
编辑部电话：0931-8470326

编　　务：周玉洁
投稿热线：0931-8473316

法律顾问：甘肃佳函律师事务所　刘林山律师

声　明

1.本刊所展示的信息，其真实性、准确性和合法性由信息发布人负责。本刊不提供任何保证，不承担任何法律责任。

2.本刊秉持原创首发立场，杜绝一稿多投和抄袭、剽窃他人作品行为，因上述问题引发的法律纠纷及相关后果皆由作者承担，本刊概不负责。

3.本刊已许可中国学术期刊（光盘版）电子杂志社在中国知网及其系列数据库产品中，以数字化方式复制、汇编、发行、信息网络传播本刊全文。

4.本刊已许可甘肃农业出版传媒有限公司在“甘味云”APP等数字化平台，以数字化方式汇编本刊全文。

5.本刊未授权任何个人和单位开展论文征稿活动，请作者投稿时将稿件统一发送至我刊投稿邮箱，认准我刊唯一官方投稿网站，作者向本刊提交文章发表的行为即视为同意我社上述声明。

农业科技与信息

目 次 Contents

第12期（总第677期） 2024年12月

【作物科学】

玉米全膜覆盖+节水滴灌水肥一体化及小麦覆土穴播一膜两用栽培技术……刘小平（001）

永靖县旱地马铃薯品种（系）引进与评价

……张志伟，张庆全，王玲琼，史旦旦，杨彧红，李永亚，冯坤蓉（005）

冬小麦-冬播马铃薯-春玉米-夏大豆“四种四收”高效栽培技术

……李旭霞，孟总彦，张文智，郭 芳，杨小江，杨 波（010）

钢架大棚薄皮甜瓜无公害栽培技术……高清龙（014）

15个朝天椒新品种比较试验……于珍珠（019）

菘蓝水肥一体化栽培技术……聂小英（023）

水果胡萝卜种植密度及施肥量试验……陈 敏，王德卿（026）

【资源环境】

基于GIS的自然灾害农业承灾体脆弱性评价

——以河西走廊区域为例……余 瀚，李 彤，闫 鹏，孟志华（030）

临夏州耕地质量现状与提升措施……戚瑞生，史英红，满本菊（036）

【林木园艺】

川东地区乡土景观元素在公园城市建设中的表达路径……李雪芬，邓小辉（040）

不同立地条件对食叶草生长特性的影响研究

……何 倩，韩 芬，王 辅，王可壮，王安民，靳雪琴，李文文（046）

小陇山林区辽东栎径级结构对海拔的响应情况……张亚雄，孙丽娟（051）

园林花卉色彩搭配与现代城市景观设计融合存在的问题及对策……王晓静（054）

希望蔓绿绒组培苗和穴盘苗生产技术……刘爱媚，黄荣辉，陈春满，郑贵朝（058）

【植物保护】

浅析武威市粘虫发生特点与监测防控技术……李 平，景亮亮，杨先悦，苏俊平，段 峰（063）

合水县核桃举肢蛾发生规律、原因及防治措施……高　辉，赵国庆（067）
桃园越冬昆虫诱虫带诱集效果调查……张译文，王卫成，牛茹萱，王晨冰（071）

【智慧农业】

基于区块链技术的水资源运行监控系统设计……段彦斌（080）
基于特征融合与改进TDNN的西瓜成熟度识别……王　颖，刘琰昕，毛璐宇，周　成（084）

【乡村社会】

中国式乡村生态治理现代化基本内涵、现实境遇及实践进路……郭璐娜（087）
乡村振兴战略视域下乡村环境内发性治理路径研究……常梦涵，陈卓武（092）

【农经管理】

紫叶矮樱钢架大棚穴盘扦插催根育苗技术……李　庚（098）
正宁县夯实乡村振兴基础的对策及建议……师亚宏（102）
瓜州县蜜瓜产业发展现状及对策……张建军，汤　茹（107）
高台县持续壮大新型农村集体经济的探索与思考……程宏斌（112）
甘肃省临泽县中药材产业发展现状及对策……刘晓刚（117）
全产业链背景下甘谷县中药材产业发展现状与对策……姚升维（121）
皋兰软儿梨产业发展探析……魏文江，周彦兵（125）
酒泉市发挥供销合作社服务乡村振兴独特作用研究……闫　亮（129）
西峰区蔬菜产业发展现状及对策……田虎兴，宋展树，卢　晶（134）
基于SWOT分析的兰州市七里河区百合产业优化策略研究……杜小龙（138）

【教育培训】

新质生产力背景下甘肃寒旱农业物联网应用型人才培养探析……王一平（143）
农民终身教育创新生态系统构建及对策
——以甘肃省为例……岳贝凡，王华林（147）
乡村振兴背景下新农科人才计算机应用能力培养路径研究……张素敏，尹　令，刘汉兴（151）

期刊基本参数：CN 62-1057/S*1984*m*16*160*zh*P*25.00*1020*35*2024-12

彩页及广告索引

封二：珍惜粮食　公益广告
封三：“甘味”农产品　公益广告
封四：全面推进乡村振兴　公益广告

乡村振兴背景下新农科人才计算机应用能力培养路径研究

张素敏，尹　令，刘汉兴

（华南农业大学 数学与信息学院，广州 510642）

摘　要：当前，我国处于乡村振兴取得决定性进展、实现农业农村现代化的关键建设时期，也是我国农业新质生产发展的急速推进期，亟需大量复合型新农科人才。新农科人才既是推动农业新质生产发展的引擎，也是实现乡村振兴战略目标的主力军。在传统的农业高等教育体系下，新农科人才的计算机应用能力培养面临诸多挑战。本文针对乡村振兴中新农村建设的信息化、数字化、智慧化需求及新农科建设现状和农业新质生产发展需要，从知识体系构建、多元平台建设、AI智能应用拓展、学科交叉创新培养、学科竞赛培训方面探索新农科人才计算机应用能力的培养路径，为培养出同时满足新农科发展要求和乡村全面振兴需求的多层次新农科人才提供参考。

关键词：人才培养路径；新农科；乡村振兴；计算机应用能力

中图分类号：G642；TP3-05　**文献标识码：**A　**文章编号：**1003-6997（2024）12-0151-06

乡村振兴和农业新质生产力发展亟需大批既具有专业农林科技知识又掌握计算机应用技能的新农科人才。新农科人才通过运用所学的科学知识、专业技能进行农业科技创新、农村数智化建设，可以促进农业新质生产力发展，早日实现农业强、农村美、农民富的伟大目标。

农科类院校是培养新农科人才的主要阵地，广大农村是新农科人才未来施展才华、为国建功的主战场。培养德才兼备、全面发展的复合型新农科人才是当前农科类院校人才培养的首要任务和历史使命。新农科人才不但应具有农业新质生产力发展所需的农业科学技术，还应该掌握自动化、智能化、数字化等实现农村数智化所需的计算机科学技术。因此，培养新农科人才计算机应用能力是新农科人才培养中亟需解决的根本问题之一。

1　乡村振兴与农业新质生产力发展的关键

2017年10月18日的党的十九大报告中首次提出乡村振兴战略，农业农村农民问题是关系国计民生的根本性问题，必须始终把解决好“三农”问题作为全党工作重中之重[1]。习近平总书记在2017年12月28—29日召开的中央农村工作会议上

作者简介：张素敏，博士，讲师，主要从事计算机语言程序设计课程教学与计算机通识教育研究。

E-mail：suminzhang@scau.edu.cn

收稿日期：2024-11-01

明确提出“走中国特色社会主义乡村振兴道路的重大任务,为亿万农民描绘了一幅美丽乡村的现代图景,是振兴乡村的总纲领,是新时代做好“三农”工作的路线图”[2]。中共中央、国务院印发的《乡村振兴战略规划（2018—2022年）》中提出“到2020年，乡村振兴的制度框架和政策体系基本形成，各地区各部门乡村振兴的思路举措得以确立，全面建成小康社会的目标如期实现。到2022年，乡村振兴的制度框架和政策体系初步健全。探索形成一批各具特色的乡村振兴模式和经验，乡村振兴取得阶段性成果。到2035年，乡村振兴取得决定性进展，农业农村现代化基本实现。到2050年，乡村全面振兴，农业强、农村美、农民富全面实现”[3]。现阶段，我国正处于乡村振兴取得决定性进展的关键期和攻坚阶段，也是农业新质生产力发展的急速推进期，广大农村实现现代化是现阶段农村工作的核心任务。

乡村振兴，关键在人才，人才振兴是乡村振兴的重要前提和支撑[4]。但从现实情况来看，由于传统农业人才培育理念陈旧、农业人才培养模式不完善、农业人才评价体系不健全等原因，导致现代农业人才培育工作相对滞后[5]。当前，部分地区乡村振兴工作滞后的主要原因是缺乏发展引路人、产业带头人、政策明白人。因此，当前人才振兴工作的核心内容是如何培养多层次农科人才，为各类人才成长为乡村振兴的职业经理人、经纪人、致富能人奠定基础。农科类高校作为重要的农业人才培养基地，必须加强新农科人才计算机通识的普及与应用，将大数据、人工智能、物联网、云计算、区块链等信息科技通识普及到各本科专业，培养出同时具有扎实的计算应用能力和专业技能的复合型新农科人才，为我国广大农村实现产业兴旺、生态宜居、乡风文明、治理有效、生活富裕提供人才储备。

2　新农科专业建设及人才培养现状

2022年8月31日，教育部办公厅印发的《新农科人才培养引导性专业指南》（以下简称《指南》）中指出，新农科人才培养面向粮食安全、生态文明、智慧农业、营养与健康、乡村发展等五大领域，设置智慧农业等12个新农科专业，主要培养各专业急需的复合型人才、创新拔尖人才和卓越人才[6]。当前，国内近百所高校开设了《指南》设置的部分专业，截至本文发稿，国内高校主要开设了12个新农科专业中的11个，具体开设详情如表1所示。由表1可知，以中国农业大学、西北农林科技大学为代表，几乎所有农林类高校均开设了1个或多个新农科专业；以上海交通大学、华南理工大学为代表的以工科为主的高校也开设了新农科专业。由此可见，加强新农科建设在“985”强校和农林类高校中都获得了共识，我国新农科专业建设和人才培养正处于全面展开的高速发展时期，并取得了良好的开局。

尽管《指南》提出的新农科专业建设和人才培养面向粮食安全、生态文明、智慧农业、营养与健康、乡村发展五大领域，但各高校根据自身条件主要侧重于粮食安全、智慧农业、营养与健康三个领域进行新农科建设，在生态文明和乡村发展领域的专业建设与投入较少。因此，我国的新农科专业建设和人才培养还存在各领域发展不均衡的问题。进一步分析可知，《指南》中设置的12个新农科专业中，开设食品营养与健康和智慧农业专业的高校数量最多，分别为67所、25所；开设生物育种科学、土地科学与技术、农业智能装备工程和兽医公共卫生4个专业的高校数量也在10～20所；开设生物育种技术、生物质科学与工程、生态修复学、国家公园建设与管理、乡村治理4个专业的高校数量均为个位数；尚无高校开设全球农业发展治理专业。图1详细展示了国内高校在新农科专业建设上的布局，是各高校在传统学科优势和专业积累基础上通过慎重抉择形成的结果。

新农科专业建设和人才培养也表现出智能

表1　新农科专业在国内大学的开设情况

领域	专业	开设高校数量	代表性高校
粮食安全	生物育种科学	18	中国农业大学、西北农林大学、华南农业大学等
	生物育种技术	3	北京农学院、新疆农业大学、大连海洋大学
	土地科学与技术	12	中国科学技术大学、国防科技大学、佛山大学等
生态文明	生物质科学与工程	4	中国农业大学、西南大学、湖南城市学院等
	生态修复学	1	南京林业大学
	国家公园建设与管理	2	北京林业大学、东北林业大学
智慧农业	智慧农业	25	南京农业大学、西北农林科技大学、上海交通大学等
	智慧林业	14	南京林业大学、西北农林科技大学、中南林业科技大学
	智慧畜牧科学与工程	15	西北农林科技大学、华南农业大学、河南农业大学等
	农业智能装备工程	20	中国农业大学、西北农林大学、南京农业大学等
营养与健康	食品营养与健康	67	华南理工大学、中国海洋大学、西北农林科技大学等
	兽医公共卫生	12	中国农业大学、南京农业大学、西南大学等
乡村发展	乡村治理	5	海南大学、福建农林大学、河南农业大学等
	全球农业发展治理	0	暂无

数据来源：中国教育在线网站（www.gaokao.cn）。



图1　国内高校开设新农科专业各领域占比分布情况

化和复合型两大特征，各专业建设和人才培养更加信息化、智能、智慧，各新农科专业均增加了信息学科相关课程，从而印证了新农科专业建设的发展方向。同时，新农科各专业的人才培养注重学科交叉、应用创新，着力培养德、智、体、美、劳全面发展且具有深厚人文底蕴与自然科学基础、扎实专业知识、实践能力和国际视野的新农科人才，从而满足相关领域发展和乡村振兴的需求。

综上所述，在国家政策指引下，我国各高校掀起了新农科建设和人才培养热潮，建设现状可总结为以下几点。一是全国各大高校根据自身学科优势分别开设了新农科专业，其中不但有农林高校，而且还有理工类或综合类院校，新农科专业建设和人才培养取得了良好开局。第二，新农科专业建设和人才培养不均衡。营养与健康、智慧农业和粮食安全领域取得了较好的发展，乡村发展和生态文明领域发展相对滞后。第三，新农科建设中，国内高校对不同新农科专业开设的选择和布局不均衡。食品营养与健康、智慧农业专业赢得发展先机，少数专业较为冷门，开设院校极少。第四，新农科建设和人才培养中强调学科交叉和应用创新，着力培养复合型、创新拔尖型、卓越型多层次人才。第五，新农科建设要顺应第四次产业技术革命的智能化特征，以此赋能新农科各专业，在不同的专业和领域实现智能化、智慧化、信息化。第六，国内高校根据自己的学科专长、政策指引、社会需求和乡村振兴需要，在传统农林专业优势学科基础上

派生了新农科专业，当前新农科专业和方向的建设和人才培养呈现出百家争鸣、百花齐放的发展态势。

3　新农科专业人才计算机应用能力培养存在的问题

3.1 新农科专业对于程序语言和工具的偏好和侧重不同

不同编程语言和工具在解决实际问题时具有各自的特点与优势，因此一类编程语言和工具不可能适合不同新农科专业在其领域内的所有应用需求。以智慧种植为例，相关专业主要利用计算机进行作物数据分析或可视化分析，较适合采用擅长数据可视化的编程语言（如R语言）。当需要根据照片分析作物病虫害发生情况时，通常会使用MATLAB软件进行计算机辅助实验进行相关的图像处理工作。因此，新农科专业的程序设计等通识课程若采用单一或少数编程语言及工具将无法满足新农科专业实际的应用需求。

3.2 授课教师缺乏农林科学知识，难以指导新农科专业交叉应用

程序设计等通识课程需要由具有丰富计算机教育背景的授课教师任教，但是传统的计算机专业教育背景的教师通常缺乏农林科学知识，因此在面对一些学科交叉应用时会出现概念不清、思路不对，结论不佳的情况。以智慧养殖为例，通过视频监控自动监测动物行为，并对其异常行为进行预警是当前的研究热点之一。动物的早期疫病、发情等行为特征较为复杂，并具有一定隐蔽性和偶然性，不具备动物科学背景、缺乏经验的计算机通识教师无法分辨出动物的行为细节，导致实现动物行为自动识别分类的智能化监测较为困难。

3.3 授课教师获取相关数据集困难，难以在教学内容中拓展新农科实例

目前，农业领域的公共共享数据集较少，规模化的植物数据采集代价较高，且由于动物行为的不可控，动物数据集获取难度更大。因此，任课教师在新农科专业的通识课程授课过程中增加新农科应用实例还面临缺乏相关数据集的窘境。以智慧林业为例，在森林资源智慧监测和评估中，通常要获取评估区域的卫星遥感图像、地图数据、统计数据等不同类型的数据进行集成和分析，以综合评估森林资源，但获取这些数据不同类型的专业设备非常昂贵，数据获取难度大。因此在相关专业学生的计算机通识课程中扩充此类应用实例较难。

3.4 农科类专业学生缺乏信息科学知识，无法应用计算机知识进行应用创新

在面向新农科专业学生的计算机通识课程教学中，应鼓励学生基于该课程进行应用创新，但大部分新农科学生缺乏信息学科基础知识。以智慧农业专业为例，实现作物环境的自动检测和控制是智慧农业常见任务，实现这一任务的工作基础是搭建传感器网络实时获取环境数据，因此需要具有各类传感器设备的接口标准、通信协议和数据格式转换的基础知识。智慧农业专业的低年级学生因缺乏相关知识，无法搭建传感器网络顺利获取数据，导致相关应用创新实验无法开展，无法进行下一步应用创新研究工作。

4　新农科人才计算机应用能力培养路径

新农科建设和人才培养具有层次高、多学科交叉以及促进农业智能化、农村现代化等特点，计算机通识课程对于新农科专业应用创新、农业智能化、农村现代化，智慧乡村建设具有非常重要的基础作用，新农科专业的计算机通识、数据库应用等课程既是新农科人才掌握计算机软件开发知识和信息处理技能的基础课程，也是其培养计算思维、创新思维的启蒙课程，还是其学习本专业相关信息化、智能化、智慧化课程的先行课程，应重点学习。为了夯实新农科专业人才计算机应用能力，培养他们的计算思维、创新思维，必须深入探讨如何合理规划计算机通识课程的内

容和实验内容、优化教学过程与考核方法、提升教学效果和人才培养质量等问题，形成新农科人才的计算机应用能力培养路径，助力新农科建设和新农科人培养。

4.1 构建计算机通识知识体系

第一，以计算机通识课程内容为核心，从思政教育、计算思维培养、人工智能启蒙多个维度扩充知识广度、拓宽课程知识体系，提升新农科人才的综合素质。将社会主义核心价值观、家国情怀、航天精神、工匠精神等思政元素，迭代、递归、模块化等计算思维，神经网络、机器学习等AI基础知识与计算机通识课程相结合，扩大学生基础知识口径，提升学生综合素养。第二，围绕计算机应用经典问题，拓展基础软件、程序开发、物联网、云计算、大数据和人工智能应用技能，针对每一类经典应用问题设置多样化的学习途径和典型应用场景，通过解决典型场景下的应用问题提升知识理论水平和应用技术技能。第三，可搭建多学科共建的虚拟教研室、校企合作实践平台以及运用“科技小院”项目等创新模式，提高新农科人才计算机应用创新能力。

综上所述，针对新农科人才应用能力培养，应构建合理的知识体系，从多维度拓宽新农科人才的知识广度和深度，建立如图2所示的计算机通识课程体系，为新农科人才培养提供合理的知识体系和灵活的学习方式，满足新农科人才培养的多目标需求。

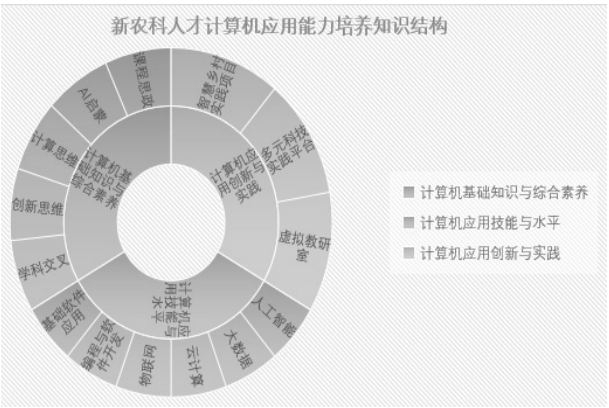


图2　计算机通识课程体系

4.2 推进多元平台建设

新农科专业建设和人才培养要求其具有基础的计算机应用能力，即熟练应用office等办公软件、数据库管理软件等技能。高阶应用能力培养需求则涵盖了C/C++/Python/R/Matlab等不同计算机语言编程能力以及计算机物联网、云计算、大数据和人工智能等与智慧农业紧密相关的计算机应用技能培养。由于不同的新农科专业不同层次的需求存在一定差异，为了满足所有专业人才提升计算机应用能力的要求，应通过构建多元平台，基于多元平台提供个性化的能力提升课程以及定制化的能力提升方案，满足不同专业和层次人才培养的不同要求。

4.3 利用人工智能赋能计算机应用能力培养

新农科人才计算机应用能力提升的主要目标是提升其利用计算机进行学习、科研、办公等方面的数字化、自动化、智能化处理能力。当前，随着社会信息化、数字化程度的提升，智能化应用的地位日渐凸显。无论是传统种植、养殖行业还是生物育种等，都正经历数字化、智能化转型升级。因此新农科人才的计算机应用能力提升不仅要着眼当前，更应面向未来，紧跟AI领域前沿成果应用，促进新农科行业和专业的发展。

4.4 注重学科交叉创新

新农科背景下，全面推进乡村振兴需要大量掌握智慧农林专业知识和技能的科技人才。智慧农林主要是将现代科学技术与农林种植、畜牧养殖相结合，从而实现农业、林业、畜牧业无人化、自动化、智能化发展；计算机应用能力作为信息学科的基础技能，是掌握无人化、自动化和智能化技术的先修课和基础课。因此，计算机应用能力是农林科技人才掌握智慧农林科技、实现农林科技创新的基本能力。

智慧农林人才科技创新包括理论创新、实践创新、应用创新。由于本科阶段的农林人才理

论水平有限，难以实现创新，所以新农科专业本科生的科技创新主要集中在实践或应用创新。以动物科学为例，智慧测定、智慧监测和智慧养殖等创新思想和方法最终都通过对应的程序编码以软件或系统的形式呈现出来，主要创新成果包括发明专利、软件著作权、论文3种形式，但无论哪种创新，都离不开计算机应用能力的加持。因此，扎实的计算机机应用功底是相关创新工作的关键。

4.5 基于计算机应用能力提升各类学科竞赛的竞技水平

各类计算机应用类学科竞赛或融合计算机应用内容的学科竞赛都需要过硬的计算机应用技巧和利用计算机应用能力解决实际问题的能力。诸如ACM国际大学生程序设计竞赛、蓝桥杯全国软件和信息技术专业人才大赛等比赛主要考核参赛者分析问题、运用计算思维解决问题、实践编程等计算机编程方面的实践能力。在这类比赛中获得奖项既是对其编程能力的肯定，也是对其计算机综合应用能力的嘉奖。如新农科专业学生在自己本专业教师与计算机专业教师的联合指导下参加各类竞赛，运用计算机技术和新农科专业技术相结合解决新农科专业的实际问题，可以进一步提升学生创新能力和计算机应用水平，取得更高级别的个人荣誉与教学成果。

5　结语

在提升农林科技水平，培养复合型、创新型农林人才，促进农业新质生产发展的目标下，农林高校作为新农科教育、农业科学研究、农林人才培养的排头兵，应提高站位，肩负起时代赋予的使命，为党育才，培育满足全面实现乡村振兴所需的各类农林人才。我国在实施乡村振兴战略时，应面向经济全球化和正在兴起的第四次产业革命，探索实施“新农科”教育[7]。加强计算机应用能力培养课程的教学改革，提升新农科人才的计算机应用能力，将为我国新农科专业建设和人才创新能力提升奠定坚实基础，为农业新质生产发展创造人才条件。面向新农科专业的计算机应用能力培养应该从知识体系构建、多元平台建设、AI智能应用拓展、学科交叉创新培养、学科竞赛培训等多个维度展开，授课教师应该面向未来，以高度的责任感和先进人才培养理念对该课程进行改革，提升新农科人才计算机应用能力，为早日实现乡村振兴贡献力量。

参考文献

[1] 习近平.决胜全面建成小康社会夺取新时代中国特色社会主义伟大胜利[N].人民日报,2017-10-28(1).

[2] 王雯慧.中央农村工作会议:走中国特色的社会主义乡村振兴道路[J].中国农村科技,2018(1):8.

[3] 中国政府网.乡村振兴战略有了五年时间表[EB/OL].(2018-09-27)[2024-10-27].https://www.gov.cn/xinwen/2018-09/27/content_5325640.htm.

[4] 光明网.人才培养助力乡村振兴，激发农村经济新活力[EB/OL].(2024-05-09)[2024-10-27].https://topics.gmw.cn/2024-05/09/content_37312499.htm.

[5] 光明网.乡村振兴视域下现代农业人才的培育路径[EB/OL].(2023-12-01)[2024-10-27].https://gongyi.gmw.cn/2023-12/01/content_37002973.htm.

[6] 中华人民共和国教育部.教育部办公厅关于印发《新农科人才培养引导性专业指南》的通知[EB/OL].(2022-09-05)[2024-10-27].http://www.moe.gov.cn/srcsite/A08/moe_740/s3863/202209/t20220919_662666.html.

[7] 董维春,梁琛琛,刘晓光.从传统到现代的高等农业教育:兼论中国“新农科”教育[J].中国农史,2018,37(6):33-45.

（编辑　祁凡琳）

基于“互联网+”和AI的非计算机类本科专业“Java语言程序设计”课程的改革与实践

张素敏,尹 令,黄 琼,陈湘骥
(华南农业大学 数学与信息学院,广东 广州 510642)

[摘 要] 从“互联网+”、AI视角出发,提出构建“Java语言程序设计”通识课程多元知识学习平台和资源体系,为学习Java的本科生提供一个开放、共享、便捷的Java程序设计学习框架,实现学习过程各环节的自动化管理和课程成绩的智能化评价,提升本科生的Java语言程序开发能力和编程素养,提高“Java语言程序设计”课程教学质量,为各本科专业复合型科技人才培养奠定基础。

[关键词] “Java语言程序设计”; AI;互联网+;课程改革
[中图分类号] G642 [文献标志码] A [文章编号] 2096-9503(2025)01-0041-06 [收稿日期] 2024-10-27

一、“Java语言程序设计”课程的性质与目标

传统的计算机编程通识课程面向不同专业背景和学习基础的学生进行统一授课,缺乏个性化设计,课程考核的要求较低,只要求学生掌握程序设计课程的基础内容并通过期末考试即可。随着图像识别、语音识别、文本智能处理、自动驾驶等人工智能技术在各领域的广泛应用,很多专业和方向的学生急需掌握计算机编程技能,特别是以学科交叉、创新应用为特征的非计算机类本科专业和方向,对计算机编程技能的需求更为迫切,且这种需求具有跟其学科背景紧密关联的特征,这对计算机编程通识课程提出了新的要求。

非计算机类本科专业“Java语言程序设计”课程是面向非计算机类本科专业本科生开设的编程类通识公共基础课,旨在使学生初步掌握Java程序设计语言,能够采用计算思维分析问题,能够使用编程工具编写程序并完成问题求解、数据处理或相关应用,为他们今后在专业学习中进行科学研究和工程应用打下坚实的基础,为各专业培养思想过硬、编程基础扎实、编码能力突出、视野开阔的新工科、新农科人才奠定良好基础。

二、非计算机类本科专业“Java语言程序设计”课程教学现状

调研发现,各大高校在程序设计等信息基础课程教与学中均存在不少问题。有些教师认为本科阶段的“Java语言程序设计”教学,存在“教学内容陈旧,缺少新技术教学”“教学模式落后,影响学习效果”“教学资源有限,缺乏个性化教学”“融合程度不高,学科发展和大学生创新能力培养受限”“考核方式不完善,大学生能力难以全面考评”等问题[1]。一些教师认为学生学习程序设计课程时存在“上课走神或许并非‘故意’”“理论与经验世界的割裂”“个体基础认知体系的差异”“有限的学习时间与学业挑战的矛盾”等问题[2]。外国专家学者认为学生学习编程存在学习障碍,并强调学习障碍的内在原因。国内学者则强调外因,认为“造成编程学习障碍的因素,有编程本身的学科性问题,也有教法的问题,还有学习者自身情感的问题”,并列举了各类问题的具体表现,最后提出了解决各类问题的策略[3]。还有部分教师认为高校计算机通识教育发展中存在“学生与课程的黏合度不紧密”“教育改革成效不明显”“毕业生信息技术应用能力与岗位需求能力的匹配度问题”等问题,并提出了走出困境的计算机通识教育创新建设框架及实施策略[4]。计算机通识课程从学习角度看存在“学习方法”和“学习资源”问题,从教学角度看存在“碎片化思维问题”和“能力培养问题”,解决这些问题需要对课程进行资源构建和教学设计[5]。

综上所述,可知当前非计算机类本科专业程序设计课程作为大学低年级通识课程,依然存在较多问题,具体表现为以下五个方面。

(一)学生缺乏学习兴趣,畏难情绪严重,缺乏学习动力

目前,计算机程序设计公共基础课程内容和学生所学专业弱相关,使得学生误以为程序设计课程和自

[基金项目] 广东省高等教育教学改革项目“大规模远程在线考核关键技术研究”(项目编号:粤教高函〔2020〕20号);华南农业大学2022年课程思政示范项目“数字电路与逻辑设计教学团队—课程思政示范团队”。

[作者简介] 张素敏(1977—),男,华南农业大学数学与信息学院/软件学院讲师,主要从事计算机视觉、智慧农业、Java/C/Python程序设计课程教学和研究。

中国知网 https://www.cnki.net

身专业学习无关,对程序设计的学习毫无兴趣。兴趣是最好的老师,一旦学生对所学课程缺乏兴趣,将导致学生失去学习热情,缺乏学习动力,无法自驱学习,最后造成学生被动学习和消极学习的局面,教与学的效果难免不佳。

(二)过分强调理论,缺乏编程训练,动手能力差

将过多的教学学时和学习精力用于对程序设计语言语法规则的讲授和学习,实际的动手写代码、程序调试训练不够,导致学生动手就错,无法正确编写、调试程序。

(三)缺乏算法设计素养训练,无法养成计算思维

缺乏程序设计算法素养训练,难以养成计算思维。对于经典的递推、排序、递归、迭代、查找等算法缺乏训练,导致学生面对较复杂的问题束手无策,无法采用计算思维解决实际问题。

(四)教学资源一成不变,教学案例不能与时俱进

教学平台单一,数据和信息不能及时更新,无法紧跟专业发展热点。程序设计教学平台中的课程内容和实训内容一成不变,一方面无法紧跟专业发展热点,不利于学生掌握程序设计在其所学专业中实现新应用、解决新问题的方法,另一方面也造成部分学生弄虚作假,提交往届学生遗留的代码蒙混过关,实际能力没有提高。

(五)师生沟通不畅,不能及时答疑解惑

教与学交流效率不高,难以及时答疑解惑,不能实现教学相长。由于缺乏有效的师生交流渠道,教师无法及时了解学生对知识的实际掌握情况,学习存疑的学生也无法及时得到老师的答疑解惑。

三、基于"互联网+"和AI的非计算机类本科专业"Java语言程序设计"课程改革路径

针对上述"Java语言程序设计"课程教学存在的诸多问题,亟须打破学习条件限制和资源访问壁垒,创新教学模式,采用多样化教学方法,提升课程教学质量和效果。本文提出基于互联网+构建融合课程思政、计算思维引导、人工智能启蒙和Java编程能力培养的多元知识平台和资源体系,为本科生提供一个开放、共享、便捷的Java语言程序设计学习过程,实现学习记录、实验管理、问题答疑、课程考核和成绩评价的自动化、智能化(图1)。

如图所示,"Java语言程序设计"课程教学改革路径是:围绕"Java语言程序设计"课程内容,从课程思政、计算思维、AI启蒙和编程技能四个维度,整合慕课、微课、实训、直播等多种资源,通过慕课实现基础知识的介绍,采用微课解析课程的重点、难点和疑点,利用实训平台在线判断学生程序对错,督促学生编码,提升动手能力,结合直播、论坛、QQ群或微信群等方式实现及时的答疑解惑,连通ChatGPT、文心一言等智能语言处理工具实现AI答疑,结合AI大数据分析手段实现学习过程记录、实验管理、问题答疑、课程考核、成绩评价的自动化记录、智能化分析。

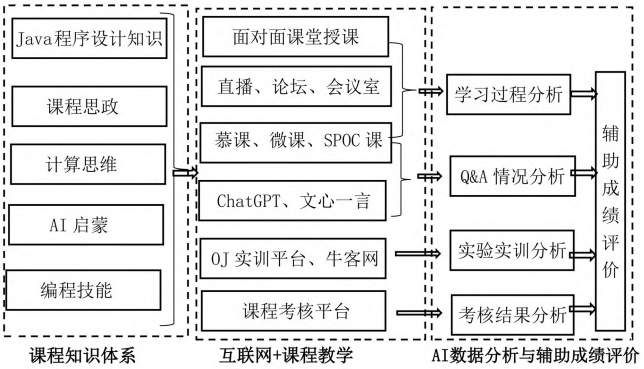


图1 基于"互联网+"和AI的"Java语言程序设计"课程改革路径

四、"Java语言程序设计"课程改革的具体措施

(一)坚持课程思政,提高学生思想文化素养

将"Java语言程序设计"课程教学与课程思政紧密融合,用正确的思想引导人。具体而言,"Java语言程序设计"课程应该以社会主义核心价值观为中心,有效融入家国情怀、道德伦理意识、敬岗爱业精神、科研创新精神、航天精神、工匠精神等最为核心的思政元素,坚定各类专业学生的理想信念与专业认同感,提高创新精神和实践能力,在"Java语言程序设计"课程内容学习的潜移默化中,培养出既具有专业的学科知识和信息科学技术,又具有正确的世界观、人生观、价值观的复合型高素质人才。

(二)加强学科交叉,优化课程内容和实例,提高学习兴趣

传统的《Java语言程序设计》对Java语言的程序设计问题进行了全面介绍,更适合计算机相关专业学习。目前各非计算机类本科专业的程序设计课程课时有限,且各专业需要程序完成的计算问题和信息处理问题侧重不同,因此传统的《Java语言程序设计》教材对非计算机类本科专业来说难度较大,实用性不强。

为此,非计算机类本科专业"Java语言程序设计"课程的授课应充分考虑学生专业领域、编程基础、学时安排等问题,通过营造开放包容的课程建设氛围,组织多学科教师联合编写课程教材,设计灵活的课程知识体系与多样化实践内容,搭建支持多途径学习的综合学习平台,组建跨学科教学师资队伍等措施优化教学内容,促进多学科交叉,从而降低非计算机类本科专业学习程序设计的难度,提升学生学习兴趣(图2)。

中国知网 https://www.cnki.net

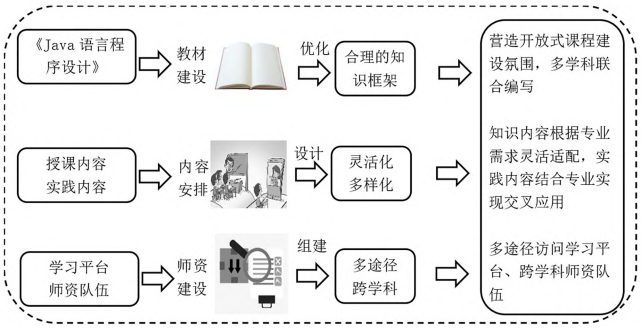


图 2　课堂内容和案例调整思路

(三)以学生为中心,因材施教

1. 因材施教,多目标培养

以学生为中心,根据课程内容难易程度,将课程内容划分为入门知识、核心内容、提高争优和挑战自我四个级别。对于以复合型人才为培养目标的学生,只需要掌握入门知识和核心内容,通过期末考核要求即可;对于以复合型高级人才为培养目标的学生,则增加一些重点、难点、疑点和较难的编程训练,帮助这类学生期末考核取得优异的成绩,并鼓励其参加计算机等级考试以获取证书;对于以拔尖创新人才、卓越人才为培养目标的学生,则鼓励其挑战自我,一方面引导其挑战竞赛任务,能力优异者鼓励其参加“蓝桥杯程序设计大赛”“ACM 大学生程序设计大赛”,另一方面培养其解决实际问题的创新能力,鼓励其参加“‘大创’项目”“互联网+”“挑战杯”等创新创业竞赛。通过多目标培养,实现其他专业和信息科学技术的学科交叉,增强学生的创新能力和创新意识,培养出更多既具有丰富的本专业知识,又掌握信息技术等前沿科技的复合型、拔尖创新、卓越科技人才。

2. 根据课程内容特点,多方法教学

根据程序设计课程内容的难度和重要程度,将课程理论知识分为基本语法、简单算法、简单实例,核心知识、经典算法、典型实例,重点、难点、疑点知识三类;将实验动手技能培养分为基础技能、中等技能和高级技能。考虑到程序设计公共基础课程理论课时和实验课时的有限性,采用自学与授课相结合、线上与线下互补、研讨与参与协同等多方法结合的方式,共同完成理论知识传授和实践技能培养(表 1)。

3. 注重师生交流,多途径答疑解惑

为及时有效解决学生学习过程中出现的问题,可采用网络直播,建立助学 QQ 群、微信群、公众号、小程序,开发答疑论坛、AI 智能答疑系统,连通 ChatGPT 或文心一言自然语言处理平台等多途径进行师生交流,及时解决学生学习过程中的疑惑,实现师生高效沟通(图 3)。

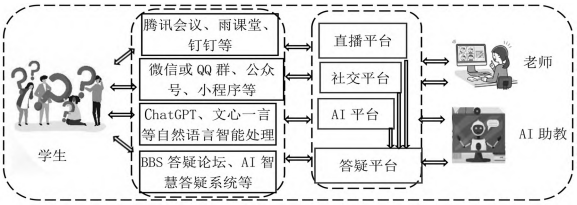


图 3　多途径答疑实施思路

针对学生作业或实验中难度较大的题目或学生提问集中的问题,为避免学生对同一问题反复提问、教师反复回答,教师可以通过直播的方式进行集中答疑,并将讲解内容录制存储在答疑平台,供后续的学生学习。学生个人的疑问可以通过社交软件留言,先由有能力回答的同学在群中进行解答,教师视情况再予以补充,在群中提出问题和回答问题的同学可对其进行一定的平时成绩奖励;群内的所有问题同样归档到答疑平台,供有相同疑问的同学查询。通过一定时间对大量问题及解答的累积沉淀,在答疑平台形成疑

表 1　多方法教学实施方案

课程内容	知识与技能分类	知识与技能详情	授课方法
理论知识	基本语法、简单算法、简单实例	数据类型、常量、变量、表达式、顺序程序,单分支、双分支等	中国大学 MOOC、网易云课堂 Cours163 等
	核心知识、经典算法、典型例题	多分支程序、多重循环程序、数组与字符串、函数、对象与封装	研讨式反转课堂、参与式课堂辩论等
	重点、难点、疑点	排序与查找、递归、指针、结构体、继承与多态、链表	微课、小规模限制性授课(SPOC)
实践技能	编程基础技能	程序基本结构、程序调试过程、程序输入与输出,顺序、分支、循环程序,冒泡与快速排数、最大公约数、最小公倍数、素数、数组、字符串、函数等	程序设计在线判别(OJ)平台与实验课堂相结合
	编程中等技能	排列与组合,二维数组、链表、队列、堆栈,文件、多媒体、数据库和网络等	竞赛培训实验平台
	编程高等技能	类、对象、继承、多态;树、图、动态规划;并发和多线程;软件架构和设计模式等	创新创业项目实训平台

中国知网　https://www.cnki.net

难问题及解答大数据,基于该数据可以进一步构建自动答疑 AI 大模型、训练出 AI 助教,之后学生的疑难问题就可以通过 AI 助教完成解答,答疑平台从基本的 BBS 答疑论坛升级为 AI 智能答疑系统,教师只需要定期对答疑系统不能解决的问题进行处理即可。

(四)注重实践,增加 AI 应用,激发学习兴趣

1. 注重实践,基于 OJ 在线判别程序设计系统督促学生完成编程训练

提高编程能力是一个熟能生巧、由量变到质变的过程,因此提高程序编写水平最直接的办法就是多动手练习,只有经过反复大量的编程训练才能练就过硬的编程本领。在编程实践环节,教师少、学生多,及时了解学生编程的效果和进度十分困难,尤其是部分缺乏学习自觉性的学生实验实践不认真,教师的督促措施非常有限。为了解决这一问题,基于 OJ 在线判别程序设计系统应运而生。一方面,该系统可以根据实验实践需求,设置编程实践任务,学生登录系统获取任务后进行程序编码并提交至 OJ 系统,系统将对正确的程序给出通过提示,反之则提示错误,从而督促学生按质按量完成编程实践;另一方面,该系统具有课堂练习、考试和竞赛功能,学习能力和进度层次不同的学生,除了完成基础实验实践外,还可以根据自己的情况,自主选择课堂练习或考试、竞赛等,进一步提升自己的编程实践能力。

由于 OJ 系统主要提供的是常见的、经典的编程任务,在使用过程中发现部分学生以提交老生遗留代码或身边同学所写代码的作弊行为来逃避独立编程训练,因此,应定期升级、更新编程任务,为不同学生差别化设置编程任务,避免作弊行为的发生,提升 OJ 系统督促学生编程训练的效果。

2. 增加 AI 应用,交叉融合,激发学习兴趣

部分非计算机类本科专业学生对学习“Java 语言程序设计”公共基础课提不起兴趣的原因是觉得程序设计在他们的专业学习中几乎用不上,认为学会了也没用,自然对该课程的学习提不起兴趣,甚至产生抵触心理,最终导致学习效果不好。如果对这些专业的学生课程在教学中增加一些 AI 编程的应用实例,解决他们专业的实际问题,可以大大提高学生的学习兴趣,提高他们学习的主动性。

以林学专业和动物科学专业为例,在程序设计实践课程中,分别增加与其专业强相关的 AI 编程任务,激发学生的编程热情。比如林学专业中,增加原木直径、截面积、材积计算、原木自动裁弯取直、木板空洞定位与修补这类跟林木相关的 AI 编程任务后,该专业学生的学习积极性显著提高,更多学生开始主动思考如何用程序解决林学专业其他的智慧林业问题。在动物科学专业的程序设计实践课中,通过提供一些与动物相关的数据,要求学生编程完成自动计算猪、牛、羊等动物的体长、体高以及预测动物体重等工作,引导学生思考如何在智慧养殖中实现动物的智慧测定。

(五)建立全过程覆盖、重点突出的课程综合评价体系

“Java 语言程序设计”课程评价的基本要求是考核过程公平、公正、公开,考核方法科学合理、操作方便,考核内容全面覆盖、重点突出,考核数据真实可靠、准确无误。要达到上述要求,必须构建一个功能完善的课程综合评价体系来记录考核过程数据、规范考核内容,确保考核方法严格执行,为学生提供严谨、权威、客观的课程成绩。

非计算机类本科专业的“Java 语言程序设计”课程综合考核体系应该以程序设计基础知识、方法、技能为基础,理论与实践并重,兼顾课程思政、计算思维、AI 启蒙等多方面进行综合评价;考核手段应该基于互联网+综合学习平台的各类学习过程数据、课堂记录数据、实验实践平台数据、答疑平台数据、在线考核系统结果进行统计分析,建立综合考核模型,实现自动化智能化的辅助评价(图4)。

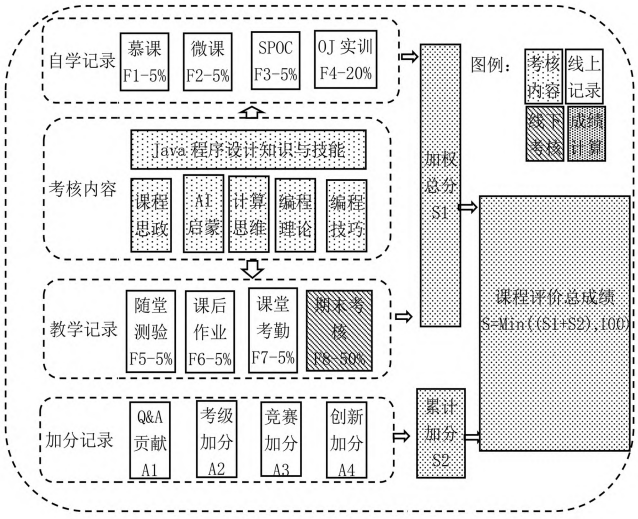


图4 “Java 语言程序设计”课程考核体系改革思路

“Java 语言程序设计”课程的最终成绩应综合课程学习全过程的所有环节的表现进行综合评价,这些环节包括:课堂测验、考勤,课后作业、课堂实验,期末考试、计算机等级考试、程序设计竞赛、多学科交叉创新成果等。通过基于互联网+和 AI 的 Java 课程教学平台采集各环节的数据记录,将各环节数据量化为百分制分数和附加分数,并根据各环节的重要性分配权重,构建最终的百分制评价模型。

$$S = \mathrm{Min}((S1 + S2),100) \quad (1)$$

中国知网 https://www.cnki.net

$$S1 = F1 * Q1 + F2 * Q2 + \cdots + F8 * Q8 \quad (2)$$

$$S2 = A1 + A2 + \cdots + A4 \quad (3)$$

公式(1)用于计算总分,公式(2)用于计算各环节加权分,公式(3)用于计算各类附加分。其中,S 为程序设计课程总成绩评价结果,若 $S1$ 与 $S2$ 之和超出 100 分,则 S 取最高分 100,故其取值可表示为 Min((S1+S2),100);$S1$ 为学习各环节的加权总分,共分为 $F1$—$F8$ 八个环节及其权重 $Q1$—$Q8$(已在图中注明);$S2$ 为额外累计加分,具体分为 $A1$—$A4$ 共四个加分项。

上述考核评分模型中,加权总分 $S1$ 兼顾了自主学习知识部分、编程训练部分和课堂教学部分的诸多环节。为了真实直观记录学习过程的细节,除期末考试外,其他数据均通过线上平台或在线程序进行采集。额外累计加分 $S2$ 则是为了激励学生踊跃参加全国计算机等级考试、程序设计竞赛、学科交叉创新和“Java 语言程序设计”课程线上平台的学习讨论而推出的举措,主要针对“Java 语言程序设计”课程开设期间在课程平台中提问或回答问题较多、取得全国计算机等级(Java)二级证书、取得相关程序设计竞赛获奖证书、获批发明专利、取得软件著作权、发表论文的学生进行加分奖励,各项加分最高不超过 5 分。

五、基于“互联网+”和 AI 的“Java 语言程序设计”课程改革实施效果

笔者从 2021 年春季学期开始对部分非计算机类本科专业的“Java 语言程序设计”课程进行基于“互联网+”和 AI 的教学改革。本节将依次呈现 2024 年春季学期“Java 语言程序设计”课程教学改革的过程性数据、2020—2024 年课程考核结果对比情况,从而印证课程教学改革效果。

“Java 语言程序设计”课程教学中,对于学生的自学内容部分,笔者主要通过中国慕课平台(https://www.icourse163.org)和精品课程学习平台(http://acm.scau.edu.cn)以及学生在线实训系统(http://acm.scau.edu.cn:8008)等互联网平台进行授课,这些系统为课程改革的实施与成绩评定提供了可靠的支持。

学生通过这些平台观看慕课视频、完成自学练习和在线编程,系统自学记录是课程成绩判断的重要依据。这些记录包括观看视频的个数、观看视频的时长、完成编程题数量、学习问题主题发表量、回答问题次数等信息,详细记录了学生自学进度和任务完成的细节。图 5 展示了学生自学视频观看情况,图 6 为学生学习有疑问时发表主题问题或回复他人主题提问的情况记录,图 7 展示了学生实践练习完成的情况,图 8 则为实践考核的成绩排名信息。

总结课程改革 5 年来的学生课程成绩,得到图 9 所示的结果。由该表可知,通过实施“Java 语言程序设计”课程改革,学生学习兴趣提高,学习效果提升,平均分逐年上升,5 年平均分提高约 15 分;优秀率提升了近 20 个百分点,学生不及格率总体呈现下降趋势;课程教学效果得到大幅提升。

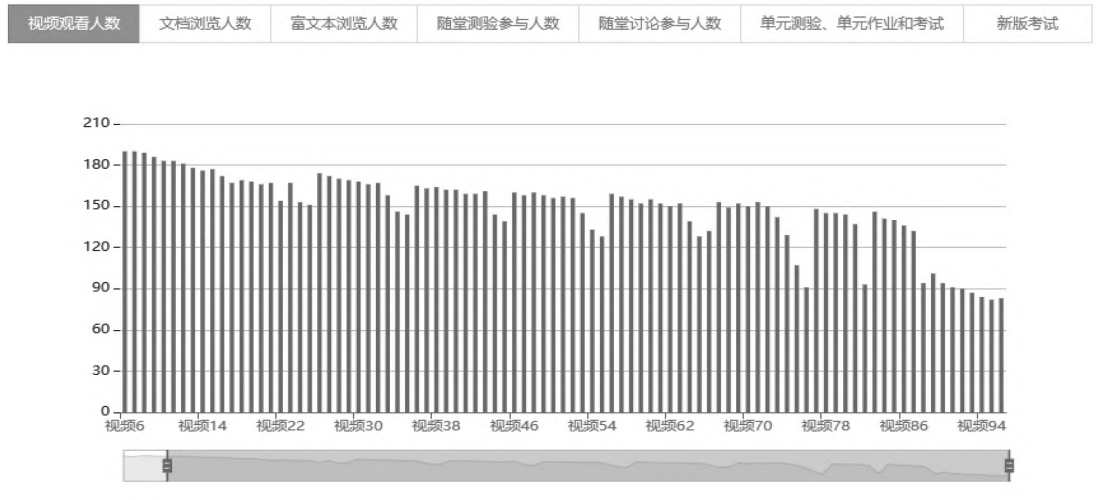


图 5　2024 年上学期的课程视频观看情况

图 10 为近 5 年来学生在在线编程实训系统中的测试成绩对比情况。由于每次测试时都有部分试题为新增题目,编程具有一定难度,因此测试平均分整体不高,优秀率较低,不及格率较高,这也说明了实践编程对低年级本科生而言是非常具有挑战性的工作。由该表数据变化情况对比可知,随着面向其他学科的教学改革路径的贯彻实施,学生实践编程能力整体朝着良好方向发展,5 年时间实践成绩平均分提高了 10 分,优秀率增加了 18 个百分点,不及格率下降了接近 40 个百分点,整体上取得了较好的实训效果。

中国知网　https://www.cnki.net

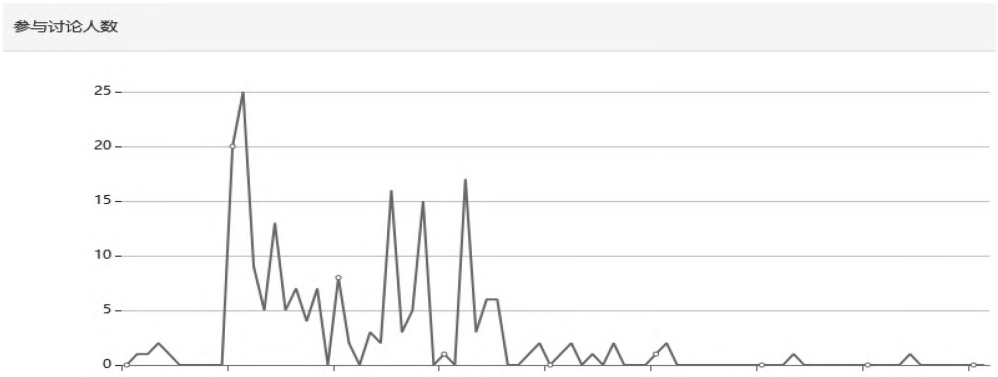


图6 2024年上学期课程问题讨论情况

23农资低碳农业12实验成绩表
(百分制分数)

开始时间: 2024-04-14 23:26:48.0 结束时间: 2024-08-12 23:26:48.0
当前时间: 2024-08-31 12:09:47 更新时间: 2024-07-07 13:24:27.0 Unknown

显示通过题数

	用户名	姓名	昵称	总题数(30)	第1次实验(3)	第2次实验(4)	第3次实验(6)	第4次实验(6)	第5次实验室(7)	第6次实验室(4)
36	202314720226	赵天祎		100	100	100	100	100	100	100
37	202314720228	朱莉平		100	100	100	100	100	100	100
38	202314720110	芦琦佳		96	100	100	100	100	100	75
39	202314720112	罗可睿		96	100	100	100	100	85	100
40	202314720121	徐龙		96	100	75	100	100	100	100
41	202314720128	庄昌宇		96	100	100	100	83	100	100

图7 2024年上学期Java自学编程完成情况

202423农资低碳农业1 - 2

开始时间: 2024-05-14 16:25:00.0 结束进场时间: 2024-05-14 17:00:00.0
当前系统时间: 2024-08-31 12:14:58 状态: Ended

共找到54条记录，当前显示从第1条至第30条。

[首页/上一页] 1, 2[下一页/尾页]

	用户名	姓名	IP地址	第几次考	题数	得分	状态	操作
	202314720105	李嘉彤	192.168.36.37	1	6	100.0	结束	查看 延长时间
	202314720124	章盼	192.168.36.36	1	6	100.0	结束	查看 延长时间
	202314720128	庄昌宇	192.168.36.4	1	6	100.0	结束	查看 延长时间
	202314720204	黄能静	192.168.36.96	1	6	100.0	结束	查看 延长时间
	202314720217	王江果	192.168.36.88	1	6	100.0	结束	查看 延长时间
	202314720219	汪力宏	192.168.36.91	1	6	100.0	结束	查看 延长时间
	202314720108	李云婕	192.168.36.12	1	6	99.0	结束	查看 延长时间
	202314720223	曾钰	192.168.36.95	1	6	98.0	结束	查看 延长时间
	202314720210	李洁	192.168.36.82	1	6	96.0	结束	查看 延长时间
	202314720116	任瑶	192.168.36.38	1	6	94.0	结束	查看 延长时间
	202314720213	乔荣星	192.168.36.104	1	6	94.0	结束	查看 延长时间
	202314720226	赵天祎	192.168.36.93	1	6	93.5	结束	查看 延长时间

图8 2024上学期Java编程实践考试情况

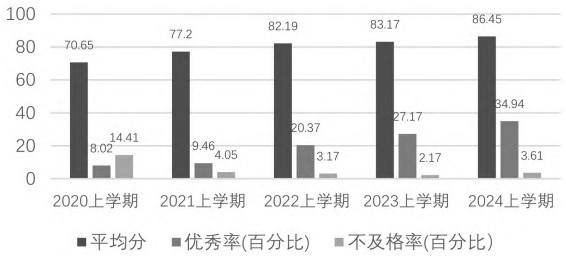


图9 2020—2024上半年“Java语言程序设计”课程成绩统计

(数据来源:华南农业大学教务系统 jwc.scau.edu.cn)

综合图9与图10的课程成绩和实践成绩来看,进行课程改革之前(2020年),确实存在学生实践编程能力和理论水平脱节的情形,不少学生表现出课程考核成绩不错但实践编程能力偏弱的高分低能现象;进行课程改革后(2021—2024),到2024年上半年为止,修读“Java语言程序设计”课程的学生的理论水平和实践编程能力都显著提升,课程不及格率和实验不及格率均降到了较低水平。

(下转第84页)

中国知网 https://www.cnki.net

[10]李恒,曾琦峰,邹正容.新时代大学生国家安全教育现状考察与实施进路:基于2360份调查问卷的样本分析[J].江南社会学院学报,2022(3):45-53.
[11]吕婷.新媒体视角下高校学生安全教育管理工作研究[J].好家长·创新教育,2018(25):1.
[12]严云洋,孙国红,乔斌.本科院校劳动教育体系构建与实施路径[J].中国大学教学,2023(Z1):75-79.

[责任编辑:刘宾年]

(上接第46页)

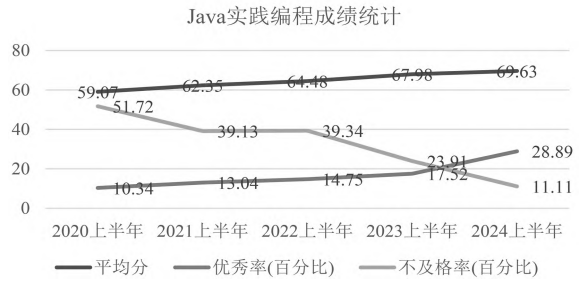


图10 2020—2024年Java实践编程成绩统计表
(数据来源:华南农业大学程序设计在线实训系统acm.scau.edu.cn:8008)

总之,通过近4年的“Java语言程序设计”课程教学改革,较好地促进了非计算机类本科专业学生对理论知识的把握与实践能力的提高,本人指导的学生的计算机等级考试通过率较高,农资低碳、林学等专业学生参加各类竞赛和获奖的大学生创新创业项目均有增加,进一步证明了基于“互联网+”和AI的“Java语言程序设计”课程改革的可行性、有效性。

[参 考 文 献]

[1]李晓辉,杨洪伟,蒋兰玲,等.其他学科背景下大学计算机基础课程教学研究与实践:以沈阳农业大学为例[J].沈阳农业大学学报(社会科学版),2023(5):622-627.
[2]李骏扬,于海琴.线上线下混合式教学与多层次认知网络构建的融合:以“JAVA程序设计”课程为例[J].东南大学学报(哲学社会科学版),2021(S1):149-153.
[3]王晓春,顾小清,刘雯.大学通识编程课程学习障碍及对策[J].中国大学教学,2024(7):45-51.
[4]周萱.知识生产模式3背景下的高校通识教育超学科发展:以计算机通识教育为例[J].江苏高教,2024(4):72-81.
[5]钱宇华.大学计算机基础通识课程的教学设计与实践[J].中国大学教学,2017(10):83-87.

[责任编辑:杨海娟]

中国知网 https://www.cnki.net

智慧牧场监测应用示范子课题项目实施协议

课题牵头单位（甲方）：华南农业大学

课题参加单位（乙方）：华南农业大学

甲、乙双方遵照 2023 年国家重点研发计划“知识驱动的科学数据智能分析方法和系统”项目实施要求，为切实做好 “智慧牧场监测应用示范”子课题实施工作，经甲乙双方平等协商，在真实、充分地表达各自意愿的基础上，达成如下联合实施协议：

1. 甲乙双方承诺认真阅读和理解子课题要求，实施过程中严格遵守。

2. 乙方在本子课题中的任务分工为：

（1）协助完成面向农业智慧牧场监测场景的知识驱动科学数据智能分析示范应用，集成数 据和知识枢纽基础功能或领域知识要素挖掘分析功能或科学数据分析模型复用功能或多模态数据多学科知识数字对象封装功 能，完成应用验证报告 1 份。

（2）申请农业智慧牧场监测相关专利 1 项。

3、子课题科技经费总计 70.00 万元，乙方经费分配为 50.00 万元。乙方经费预算详情如下表所示。

经费预算表

金额单位：万元

序号	预算科目名称	金额
	（1）	（2）
1	一、中央财政专项资金	50
2	（一）直接费用	40
3	1.设备费	5.6
4	其中：购置设备费	5.6
5	2.业务费	19.4
6	3.劳务费	15
7	（二）间接费用	10

8	二、其他来源资金	0
9	合计	50

4、子课题执行期内，乙方根据子课题任务书要求定期向甲方汇报进展和研究数据。

5、课题执行过程中，甲、乙双方各自产出的知识成果原则上归各自所有，但甲方有权因非商业目的（如：以政府性会议、报告、文件、统计资料等）使用乙方课题信息，在课题执行期间进行知识产权共享。共同产出的知识成果归共同所有，可根据双方的实际贡献进行具体分配。专利、论文、著作、新品种（系）的登记申请和推广应用情况等，均须标注课题的资助编号。

6、本协议一式六份，具有同等法律效力；甲方持四份，乙方持二份。未尽事宜由双方协商解决。

甲方（单位盖章）：华南农业大学

法定代表人（签章）：

课题负责人（签字）：黄小，

2024年 4月 25日

乙方（单位盖章）：华南农业大学

法定代表人（签章）：

任务负责人（签字）：张东敏

2024年 4月 26日

近____年主持科研项目情况表（自筹、校内子课题等类型）

主持科研项目汇总：共(__项，其中A类_(项，B类__项，C类__项；余额合计____万元。

填报人：　　填报日期：　　年　月　日

序号	项目名称	项目级别	项目来源	主持人	合同经费（万元）	实到经费（万元）	结余经费（万元）	立项时间	结题时间	本人排名	课题组总人数
	智慧牧场监测应用示范子课题	A	2023国家重点研发计划	张慧敏	50	/	/	2023-12-28			

审核人：　　填报日期：　　年　月　日

注意：本表一式2份，请交1份至科研院高新科存档

南京农业大学 科学研究院

科学研究院

2024.10.9.

基于视频跟踪的泄漏气体监测与报警项目合同

甲 方：浙江红谱科技股份有限公司

地　址：浙江省杭州市西湖区西园三路 3 号 A 幢 6 楼

电　话：0571-87763825

传　真：0571-87763821

联系人：邓丰涛

乙 方：　华南农业大学

地　址：　广州市天河区五山路 483 号

电　话：020-85285383

传　真：020-85285393

联系人：　张素敏

依据《中华人民共和国合同法》的规定，合同双方就乙方为甲方实施行为监控系统开发项目（以下简称项目）事宜，经协商达成一致，并订立本合同，以明确双方的权利、义务，确保合同双方共同执行。

第一条　项目说明

1. 项目内容

乙方将本着积极、主动、客户至上的原则，按照基于视频跟踪的泄漏气体监测与报警项目内容及双方商定的项目开发进程安排，组织技术人员对泄漏气体监测与报警系统进行新功能开发、客户化修改、源代码转移并完成项目实施。同时，通过为甲方提供一系列必要的技术服务，对泄漏气体监测与报警系统在使用过程中出现的各种技术问题予以及时解决，以确保甲方在使用行为泄漏气体监测与报警系统中能正常运行。项目主要内容包括：

1）泄露气体的监测，监测目标区域内是否出现的泄露气体，要求即使微小量泄

露气体，也能实时监测。

2）泄露气体的可视化，对泄露出的气体，以显著颜色进行显示（例如红色）

3）安全预警 探测到泄露气体，第一时间进行安全预警。

4）气体泄露点定位，根据视频中气体运动扩散方向和位置，在视频高亮标识气体泄露点。

5）泄露气体特征评估（扩散速度,损失容量）

6）算法要满足以下场景：

（1）环境温度适应性：常温环境（23 度）、高温环境（40 度）、低温环境（-15 度）3 种环境下图像效果一致；

（2）系统平台适应性：视频和图像处理同时满足 PC 和嵌入式平台，其中处理速度 50Hz。

2. 项目形式：乙方负责本项目的组织实施并提供相关技术服务，包括视频跟踪处理处理技术原理、程序编码、测试程序及平台移植等工作，本项目中乙方的主要任务包括：

- 提供专业的项目管理服务
- 理解及确认甲方需求，协助甲方制定新的业务模型
- 为甲方就此项目提供免费技术和业务培训
- 软件移植及组织项目验收
- 向甲方提供相应交付件（包括视频跟踪处理技术原理、程序编码、测试程序）
- 在投产和技术服务期内为甲方提供技术支持

第二条 项目实施前提

乙方对本项目的实施基于下述主要前提：

1. 乙方作为本项目的承包商，提供全面的项目管理，甲方愿意与本项目的承包商在图像处理项目实施过程中积极配合并承担相应的义务和责任，甲、乙双方各自委派一名全责的项目经理共同管理本项目。
2. 甲方在项目中负责提供项目所需数据及设备。
3. 在项目实施中，如果涉及到甲方系统中使用的产品、相关信息和资源等第三方专

有信息，甲方将负责为乙方获得相关信息，并承担相应责任。

第三条　项目期限

本项目中的功能开发工作应在合同生效之日起5个月内完成。

（1）2021年07月16日—2021年9月5日，完成视频数据库的建立和算法设计，搭建模拟运行环境。

（2）2021年9月6日—2021年12月15日，完成算法的验证和优化设计。

如乙方完成本项目所需的环境依赖于甲方相关系统方面的环境、数据和信息等，且该环境、数据和信息等在本合同生效之日起乙方仍未获得，则本项目开发期限相应顺延，有关顺延期限由甲方根据实际情况经与乙方协商后书面确定。

第四条　合同价款和付款方式

1. 合同价款

本合同总金额为人民币10万元（¥拾万元整）。此价款包含了本合同项下项目涉及的软件开发、技术服务、项目实施报酬及源代码转移相关费用。

乙方将向甲方提供合法、有效的等额的增值税专用发票。

甲乙双方应按照中国税法的相关规定，各自承担相应的税费。

2. 付款方式

甲方就本合同项下项目分两个阶段向乙方支付本合同项下价款。在每一个阶段的付款条件成立后，甲方应根据以下阶段说明的付款金额向乙方付款：

本合同签订之日起，经过双方确认结算金额无误后乙方方可开具发票，甲方应在收到发票后，对发票进行税务机关认证，认证通过后在收到发票三十个工作日内向乙方支付合同总额的60%，计人民币陆万元整（¥60000元）。

本合同项下项目验收完成之日起，经过双方确认结算金额无误后乙方方可开具发票（包括验收款及质保金金额），甲方应在收到发票后，对发票进行税务机关认证，认证通过后在收到发票三十个工作日内向乙方支付合同总额的40%，计人民币肆万元（¥40000元）。

3. 乙方应在发票开具之日起三个工作日内利用可靠的传递方式将发票寄出，确保发票传递快速、安全，并在发票寄出后，通过电话、邮件、传真等方式及时告知甲方。

4. 付款地址

户　名：华南农业大学

地　址：广州市天河区五山路 483 号

开户行：广州工行五山支行

帐　号：3602002609000310520

税　号：124400004554165634

以上信息如有变更，乙方须以加盖财务专用章的书面方式通知甲方，变更的信息以甲方收到书面通知的时间为生效时间。

5. 开票信息

户名：浙江红谱科技股份有限公司

地址：浙江省湖州市长兴县太湖街道高铁路 669 号综合楼 507 室

电 话：0572－6066132

开户银行：中国工商银行长兴县支行

帐 号：1205270009200701246

税 号：91330522MA28CC6G5

第五条　系统交付、验收和培训

1. 系统培训：

乙方应根据项目实施的计划、进度和需要与客户的合理要求，及时安排对甲方的相关人员进行系统培训。培训目标为使受训者能够独立、熟练地完成操作，实现本合同所规定的信息系统的功能要求。

2. 系统交付：

在本合同项下乙方应向甲方提交以下交付物：

1） 提供本项目各阶段开发文档，包括视频跟踪处理技术说明文档。

2） 开发源代码,即最新的可编译执行的源代码版本。

3） 测试程序。

3. 验收标准：

本项目达到以下 3 点要求视为达到验收标准：

1）将以本合同第一条项目内容所列基于视频跟踪的泄漏气体监测与报警系统

主要内容作为本项目验收内容。在项目验收阶段逐条比对项目主要内容中所列事项。试运行期结束，未出现影响系统预期工作的情况。

2）乙方完成本合同第五条第 1 点有关系统培训。

3）乙方向甲方提交第五条第 2 点系统交付物。

第六条　技术情报和资料保密

1. 甲乙双方同意本合同项下项目及其所涉及的技术和资料属于商业机密，任何一方未经对方允许不得向第三方泄漏，由商业机密泄漏造成的损失由泄漏方承担全部责任。
2. 乙方确认在本项目实施中乙方提供的技术不侵犯第三方的权利。

第七条　双方的权利和义务

1. 甲方的权利和义务：
   - 甲方有权利对项目的相关文件做最终审定并提出修改意见；
   - 甲方有义务配合乙方按照项目进度进行项目实施；
   - 甲方有义务为乙方提供完成项目所必需的条件和场所，并派人员予以配合；
   - 甲方有义务协调与其他各相关单位的工作；
   - 甲方有义务提供项目必需的系统环境和相关的信息资源；
   - 甲方有义务提供项目所需而非由乙方提供的各项设备及软件。
2. 乙方的权利与义务：
   - 乙方有权利按照项目进度进行整个项目的系统设计、开发、集成、系统调试和试运行及系统完善等工作；
   - 乙方有义务按照本合同要求保证各项工作在预定计划内完成，并确保完全支持系统的容量升级和业务扩展；
   - 乙方有义务协助甲方在项目建设过程中保证系统的技术领先和成熟应用；
   - 乙方有义务保证所开发软件运行的正确性和稳定性。

第八条　违约责任

1. 在项目开发期限内，甲乙双方任何一方不得以任何借口和理由终止本合同的履行。任何一方无故单方终止本合同，应向对方(守约方)支付合同总额的 10%的违约金；如因此给对方(守约方)造成损失的，违约方还应负责赔偿。
2. 甲方不能按合同约定时间付款（由于乙方项目实施原因造成的除外），每拖延一周，按应付金额的 1%向乙方支付违约金，不足一周按一周计算，赔偿额最多不超过合同总额的 10%。
3. 乙方不能按第三条要求完成项目开发的(由于甲方原因造成的项目延期除外)，每拖延一周，应按本合同价款的 1%向甲方支付违约金，不足一周按一周计算，赔偿额最多不超过合同总金额的 10%。
4. 赔偿金、违约金总额不超过合同总额的 20% 的违约金。
5. 如果因非乙方原因，乙方不能够完成本合同约定的全部工作任务，以及项目最终验收不合格，甲方可解除合同，并有权要求乙方支付合同总价款的 10%作为乙方违约的赔偿金。
6. 如因不可抗力造成甲方付款逾期和乙方不能按第三条要求完成项目实施的，甲乙双方应本着互相尊重、友好协商的原则予以解决，并应在不可抗力消除之日起恢复本合同的执行。
7. 如非人为操作原因造成系统运行异常对甲方造成损失的，甲乙双方应本着尊重事实、客观处理的原则进行事故责任认定，乙方应根据实际损失数额按承担责任比例向甲方进行赔偿。
8. 甲方违约赔偿款通过银行转账支付，乙方违约赔偿款直接从合同未支付款项抵扣，若出现剩余未支付款项金额不足抵扣的情形，则通过银行转账支付。

第九条　不可抗力

甲乙双方的任何一方由于不可抗力的原因不能履行合同时，应及时向对方通报不能履行或不能完全履行的理由，在取得有关机构证明以后，允许延期履行、部分履行或者不履行合同，双方对此互不提出赔偿责任。

第十条　其它

1. 按合同规定应该偿付的违约金、赔偿金和各种经济损失，应当在明确责任十天

后，按银行规定的结算办法付清，否则按逾期付款处理。

2. 解决合同纠纷的方式：执行本合同过程中发生争议，由当事人双方协商解决，协商不成，双方同意由成都仲裁委员会仲裁。
3. 本合同未经双方同意，任何一方不得以任何形式公开本合同及附件内容以确保双方的商业机密。
4. 本合同一式肆份，甲方持贰份、乙方持贰份。
5. 本合同自双方授权代表签字盖章之日起生效，合同执行期内，甲乙双方均不得随意变更或解除合同。未尽事宜，经双方共同协商作出补充规定，补充规定签字盖章后与本合同具有同等法律效力。

甲方：浙江红谱科技股份有限公司　　乙方：　华南农业大学

甲方代表（签字）：

乙方代表（签字）：

甲方（盖章）：

乙方（盖章）：

日期：　2021 年 7 月 16

日期：

项目立项 | 项目申报（1） |

所有项目

职称评定
- 主持的项目
- 参与的项目

博硕导评定
- 主持的项目
- 参与的项目

项目性质
- 纵向(12项)
- 横向(6项)

项目分类
- 国家自然科学基金项目(4项)
- 863计划专题课题(1项)
- 广州市科技计划项目(1项)
- 厅级其它项目(1项)
- 国家重点研发计划项目(1项)
- 省重点领域研发计划(1项)
- 实验室开放课题(1项)
- 共性关键技术(1项)
- 国家重点研发计划子课题(1项)
- 技术开发(3项)
- 技术服务(2项)
- 技术转让(1项)

参与形式
- 主持(1项)
- 参与(17项)

总数:18项 (表中经费单位：万元) 项目名称 查询 新增 删除 导出

全选	项目名称	项目分类	项目成员	起止日期	合同金额	项目状态	审核状态	操作
	基于软激光测距的牲畜体型轮廓重构方法及体况评分方法等8个专利	技术转让	尹令,吴珍芳,蔡更元,张素敏,田绪红,杨杰,刘汉兴,吴贤奇	2024-12-10--2025-12-31	100	完成	学校通过	
	大规模无线传感网络可维护性理论初探	国家自然科学基金项目	张足生,张素敏	2024-09-16--2028-12-31	49	进行	学校通过	
	基于移动式平台的水下场景立体重构与目标识别	厅级其它项目	黄琼,梁云,黄沛杰,王金凤,尹令,张素敏,古万荣,林毅申,张猜,肖磊	2024-03-01--2026-02-28	70	进行	学校通过	
	知识驱动的科学数据智能分析软件系统与示范应用	国家重点研发计划项目	黄琼,张素敏,肖媚燕,古万荣,张猜,朱梅阶,刘汉兴,周运华,王金凤,尹令	2023-12-28--2027-12-28	70	进行	学校通过	
	牲畜三维表型体尺自动测量系统及应用	技术开发	尹令,张素敏,李舜鹏,吴珍芳,蔡更元,涂淑琴,刘汉兴,朱梅阶,田绪红,黄琼	2023-12-22--2025-11-30	50	进行	机构通过	
	引进猪体重、体尺智能测定技术研发与应用	国家重点研发计划子课题	尹令,肖磊,曹维,张素敏,田绪红,吴理华	2023-12-01--2027-11-30	50	进行	学校通过	
	渔业大数据系统标准化体系研究	实验室开放课题	黄琼,梁云,黄沛杰,王金凤,古万荣,林毅申,张猜,尹令,张素敏,肖磊	2023-06-30--2024-06-30	30	进行	学校通过	
	高繁母系种猪繁殖性状表型智能测定、功能基因和分子标记挖掘（2022-2023）	共性关键技术	杨杰,尹令,尹令,罗宗刚（外）,任竹青（外）,顾婷,顾婷,全建平（学）,张素敏,朱梅阶,曹露（学）,吴家劲（学）,庄站伟（学）,吴杰（学）,邱益彬	2022-08-31--2024-12-31	635	进行	学校通过	

			（学）,徐此能（学）,阮栋林（学）,王诗媛（学）,杨丽娟（学）,周身娉（学）					
	猪表型体尺无接触测量中三维点云处理关键技术研究	国家自然科学基金项目	尹令,田绪红,刘财兴,孙爱东（外）,张素敏,刘汉兴,朱纪民（学）,林润恒（学）,胡昊（学）,王家春（学）	2021-11-19--2025-12-31	58	进行	学校通过	
	基于视频跟踪的泄露气体监测与报警	技术开发	张素敏,尹令,王琴,章晓华,林润恒（学）,胡昊（学）,朱纪民（学）	2021-07-16--2021-12-25	10	进行	学校通过	编辑 项目结项
	牲畜非接触式智能识别技术研究与示范	省重点领域研发计划	田绪红,尹令,张素敏,刘汉兴,梁云,高月芳,曹维,梁世豪（学）,石帅（学）,许创熊（学）	2019-07-04--2021-12-31	200	进行	学校通过	
	三文鱼假冒与新鲜度无损检测关键技术研究	广州市科技计划项目	钟南,吴敏,许静静,吴霆（外）,周凯（学）,张素敏,梁早清,叶松龄（学）,李炫宗（学）,孙伟（学）,郭成贤（学）,李易蓬（学）	2019-04-01--2022-03-31	100	完成	学校通过	
	电子设备销售分布和业绩提升数据分析与策略	技术服务	尹令,张素敏,王琴	2018-04-23--2019-04-24	2	完成	学校通过	
	基于物联网病虫测报的远程监测传感器及数据采集节点设计及加工	技术服务	尹令,张素敏,王琴,王永福（学）,陈凯辉（学）,陈振旭（学）	2017-12-15--2018-12-20	4.95	完成	学校通过	
			高月芳,张瑞茂（外）,张素敏,黄					

SCAULIB202519289

检索证明

根据委托人提供的论文材料，委托人华南农业大学数学与信息学院 张素敏 3 篇论文收录情况如下表。

序号	论文名称	发表刊物及发表的年月卷期/页码等	作者排名	论文等级	作者文中单位	收录情况	影响因子	中科院大类分区
1	Pig body weight prediction based on weight waveform graph	COMPUTERS AND ELECTRONICS IN AGRICULTURE 出版年：2025 出版日期：SEP 卷期：236 页码：- 文献号：110412 文献类型：Article	第一作者	T2 类	华南农业大学数学与信息学院	SCI	IF2-year=8.9 IF5-year=9.3 （2024）	农林科学 1 区 Top 期刊：是 （2025）
2	On the Equivalence of HLLE and LTSA	IEEE TRANSACTIONS ON CYBERNETICS 出版年：2018 出版日期：FEB 卷期：48 2 页码：742-753 文献类型：Article	第一作者	T2 类	华南农业大学数学与信息学院	SCI	IF2-year=10.387 IF5-year=9.631 （2018）	工程技术 1 区 Top 期刊：是 （2018）
3	Point cloud-based pig body size measurement featured by standard and non-standard postures	COMPUTERS AND ELECTRONICS IN AGRICULTURE 出版年：2022	通讯作者	T2 类	华南农业大学数学与信息学院	SCI	IF2-year=8.3 IF5-year=8.3 （2022）	农林科学 1 区 Top 期刊：是 （2022）

华南农业大学图书馆 SCAULIB202519289
华南农业大学图书馆 信息检索专用章

		出版日期：AUG 卷期：199 页码：- 文献号：107135 文献类型：Article						

说明：论文等级和中科院大类分区按《华南农业大学学术论文评价方案（试行）》划分。

报告免责声明:如未盖章,报告无效

检索员：尹银怀

华南农业大学图书馆

2025-07-16

华南农业大学图书馆SCAULIB20251289

ResearchGate

See discussions, stats, and author profiles for this publication at: https://www.researchgate.net/publication/313240808

On the Equivalence of HLLE and LTSA

Article *in* IEEE Transactions on Cybernetics · January 2017

DOI: 10.1109/TCYB.2017.2655338

CITATIONS
15

READS
119

3 authors, including:



Sumin Zhang
South China Agricultural University
9 PUBLICATIONS **141** CITATIONS
SEE PROFILE



Zhengming Ma
Sun Yat-sen University
74 PUBLICATIONS **634** CITATIONS
SEE PROFILE

All content following this page was uploaded by Zhengming Ma on 29 March 2021.

The user has requested enhancement of the downloaded file.

On the Equivalence of HLLE and LTSA

Sumin Zhang, Zhengming Ma, and Hengliang Tan

***Abstract*—Among the representative algorithms of manifold learning, Hessian locally linear embedding (HLLE) and local tangent space alignment (LTSA) algorithms haven been regarded as two different algorithms. However, in practice, the effects of these two algorithms are very similar and LTSA performs better than HLLE in some applications. This paper tries to account for this phenomenon from a mathematical point of view. There are only two differences between HLLE and LTSA. First, LTSA includes a data point into its neighborhood, while HLLE does not. Second, HLLE and LTSA use different methods to align the local coordinates of manifold. In this paper, we show that, the first difference between HLLE and LTSA is not essential. However, from the viewpoint of data utilization, LTSA does better than HLLE in the neighborhood construction. This may account for why LTSA can perform better than HLLE in some applications. As for the second difference between HLLE and LTSA, we first prove that, the alignment equations used by HLLE and LTSA are exactly the same. Second, we prove that, although HLLE and LTSA uses different methods to solve the alignment equation, their solutions are exactly the same, provided that HLLE adopts the same method as LTSA to construct the neighborhoods. Based on these arguments, we claim that HLLE and LTSA are equivalent to each other. This conclusion can also be verified experimentally by using manifold learning MATLAB demo (MANI), a widely-used experimental platform of manifold learning. When testing HLLE on MANI, if HLLE adopts the same method as LTSA to construct the neighborhoods, the experimental results presented by MANI will be the same as those of LTSA.**

***Index Terms*—Hessian locally linear embedding (HLLE), local tangent space alignment (LTSA), manifold learning, pseudo inverse, QR decomposition.**

I. Introduction

As a method of data dimension, manifold learning has attracted much attention in recent years. Some representative algorithms have been emerged in manifold learning such as Isomap [1], [2], local linear embedding (LLE) [3], [4] and its variants [5]–[9], Laplacian eigenmaps (LE) [10], Hessian locally linear embedding (HLLE) [11], local tangent space alignment (LTSA) [12], maximum variance unfolding [13], and diffusion map [14], [15]. Most studies of manifold learning are carried out around these representative algorithms.

Among these representative algorithms of manifold learning, HLLE and LTSA have three distinctive features.

1) HLLE and LTSA perform best on those data which are really collected from a manifold. The reason for this may be that, among the representative algorithms of manifold learning, HLLE and LTSA reflect the geometric characteristics of manifolds best.
2) The effects of HLLE and LTSA are very similar, while the effects of other manifold learning algorithms differ from one another.
3) LTSA sometimes performs better than HLLE.

This paper tries to account for the last two features of HLLE and LTSA. The mathematical deduction presented in this paper shows that HLLE and LTSA are equivalent. LTSA can be regarded as an improved HLLE (iHLLE).

The remaining part of this paper are organized as follows. In Section II, the mathematical principle and algorithm framework of manifold learning are presented. In Sections III and IV, LTSA and HLLE are elaborated, respectively. In Sections V and VI, a simplified HLLE (sHLLE) and an iHLLE are proposed, respectively. In Section VII, the equivalence between HLLE and LTSA is proven. In Section VIII, the experimental results are presented. In Section IX, some conclusions are given.

II. Mathematical Principle and Algorithm Framework of Manifold Learning

A. Mathematical Principle

In mathematics, a d-dimensional manifold M is a Hausdorff topological space with a countable basis. For each point x in the manifold M, there must be a neighborhood X_x of x, i.e., an open set containing x, such that X_x is homeomorphic to an open set Θ_x in the d-dimensional Euclidean space R^d. This homeomorphism is called local homeomorphism. It is clear that $M = \cup_{x\in M} X_x$, i.e., the set $\{X_x \mid x \in M\}$ is an open cover of the manifold M.

In manifold learning the manifolds are often assumed to be compact. Then, there must be a finite number of open sets $X_{x_1}, \ldots, X_{x_N}$ in the open cover $\{X_x \mid x \in M\}$ such that $M = \cup_{i=1}^{N} X_{x_i}$. In manifold learning, the open set X_{x_i} is often called a patch of the manifold M, and the open set Θ_{x_i} in the d-dimensional Euclidean space R^d which is homeomorphic to X_{x_i} is called the local coordinate of the patch X_{x_i}, or a local coordinate of the manifold M, where $i = 1, \ldots, N$. The purpose of manifold learning is to determine the local

Manuscript received September 1, 2016; revised November 27, 2016; accepted January 9, 2017. Date of publication January 31, 2017; date of current version January 15, 2018. This paper was recommended by Associate Editor H. Yin. *(Corresponding author: Zhengming Ma.)*

S. Zhang is with the School of Electronics and Information Technology, Sun Yat-sen University, Guangzhou 510006, China, and also with the School of Mathematics and Informatics, South China Agricultural University, Guangzhou 510642, China (e-mail: suminzhang@scau.edu.cn).

Z. Ma is with the School of Electronics and Information Technology, Sun Yat-sen University, Guangzhou 510006, China (e-mail: issmzm@mail.sysu.edu.cn).

H. Tan is with the School of Computer Science and Educational Software, Guangzhou University, Guangzhou 510006, China (e-mail: tanhengl@mail2.sysu.edu.cn).

Color versions of one or more of the figures in this paper are available online at http://ieeexplore.ieee.org.

Digital Object Identifier 10.1109/TCYB.2017.2655338

2168-2267 © 2017 IEEE. Personal use is permitted, but republication/redistribution requires IEEE permission.
See http://www.ieee.org/publications_standards/publications/rights/index.html for more information.

coordinates of the manifold M and align these local coordinates in the d-dimensional Euclidean space R^d to form an open set $O \subseteq R^d$ which is corresponding to the manifold M globally. The open set O is called the global coordinate of the manifold M.

B. Algorithm Framework

Suppose the d-dimensional manifold M is embedded in the Euclidean space R^D, where $d \ll D$, and $X = \{x_1, \ldots, x_N\}$ is a data set taken from the manifold M, the purpose of an algorithm of manifold learning is to find a data set $Y = \{y_1, \ldots, y_N\}$ in the Euclidean space R^d such that Y is the global coordinate of X. According to the mathematical principle of manifold learning presented in Section II-A, the algorithm framework of manifold learning can be divided into three stages: finite open cover, local homeomorphism and alignment.

In the stage of finite open cover, the aim of manifold learning is to determine a neighborhood $X_n \subseteq X$ for each data point $x_n \in X$, $n = 1, \ldots, N$. The collection of the neighborhoods of all data points in X constitutes a finite open cover of manifold. There are a lot of methods to determine the neighborhoods [17]–[25]. The commonly-used method may be the K nearest neighbors (KNNs) method, which takes the KNNs of x_n as its neighborhood, $n = 1, \ldots, N$.

In the stage of local homeomorphism, the aim of manifold learning is to build a local homeomorphic mapping $\varphi_n : X_n \to \Theta_n$ between the patch X_n and its local coordinate Θ_n, $n = 1, \ldots, N$. The tangent space method is a widely-used method in which a patch is projected onto the tangent space of the mid-point of the patch [26]–[31].

In the stage of alignment, the aim of manifold learning is to derive the global coordinate Y by aligning the local coordinates $\{\Theta_1, \ldots, \Theta_N\}$ in the Euclidean space R^d. The alignment has been a hot topic in manifold learning [32]–[40].

III. LTSA Algorithm

We elaborate LTSA [12] within the algorithm framework of manifold learning presented in Section II-B.

A. Finite Open Cover

In the first stage of manifold learning, i.e., the stage of finite open cover, for each data point x_n, LTSA first looks for its KNNs $x_{n_1}, \ldots, x_{n_K}$ and then constitutes a patch X_n by using x_n as well as its KNNs $x_{n_1}, \ldots, x_{n_K}$

$$X_n = \begin{bmatrix} x_{n_1} & \ldots & x_{n_K} & x_n \end{bmatrix} \tag{1}$$

where $n = 1, \ldots, N$.

B. Local Homeomorphism

In the second stage of manifold learning, i.e., the stage of local homeomorphism, LTSA uses principal component analysis (PCA) method to construct a local homeomorphic mapping φ_n for each patch X_n. The PCA method is as follows.

1) The patch X_n is centralized

$$\hat{X}_n = \begin{bmatrix} x_{n_1} - \bar{x}_n & \ldots & x_{n_K} - \bar{x}_n & x_n - \bar{x}_n \end{bmatrix} \tag{2}$$

where $\bar{x}_n = [1/(K+1)](\sum_{k=1}^{K} x_{n_k} + x_n)$ is the center of the patch.

2) The centralized matrix $\hat{X}_n$ is singular value decomposition (SVD)-decomposed

$$\begin{aligned} \hat{X}_n &= U_n \Pi_n V_n^T = U_n \Omega_n = \begin{bmatrix} U_{n,1} & U_{n,2} \end{bmatrix} \begin{bmatrix} \Omega_{n,1} \\ \Omega_{n,2} \end{bmatrix} \\ &= U_{n,1}\Omega_{n,1} + U_{n,2}\Omega_{n,2} \end{aligned} \tag{3}$$

where $\Omega_n = \Pi_n V_n^T$, $U_{n,1}$ is the matrix composed of the first d column vectors of the matrix U_n, $\Omega_{n,1}$ is the matrix composed of the first d row vectors of the matrix Ω_n.

3) The local homeomorphic mapping φ_n is defined as

$$\varphi_n(x) = U_{n,1}^T (x - \bar{x}_n) \in R^d. \tag{4}$$

According to φ_n, the local coordinate Θ_n of the patch X_n is given by

$$\begin{aligned} \Theta_n &= \begin{bmatrix} \theta_{n,1} & \ldots & \theta_{n,K+1} \end{bmatrix} = \varphi_n(X_n) \\ &= \begin{bmatrix} \varphi_n(x_{n_1}) & \ldots & \varphi_n(x_{n_{K+1}}) \end{bmatrix} \\ &= \begin{bmatrix} U_{n,1}^T(x_{n_1} - \bar{x}_n) & \ldots & U_{n,1}^T(x_{n_{K+1}} - \bar{x}_n) \end{bmatrix} \\ &= U_{n,1}^T \hat{X}_n = \Omega_{n,1}. \end{aligned} \tag{5}$$

Remark 1: The column vectors of $U_{n,1}$ are the principal components of the covariant matrix $\sum_{k=1}^{K+1}(x_{n_k} - \bar{x}_n)(x_{n_k} - \bar{x}_n)^T$. This is the reason why the method is called PCA method.

Remark 2: Let $T_{\bar{x}_n}(M)$ be the tangent space of the manifold M on the point $\bar{x}_n$, the column vectors of $U_{n,1}$ are the orthonormal basis of $T_{\bar{x}_n}(M)$. This is the reason why the method is also called tangent space method.

Remark 3: Since $\Theta_n = U_{n,1}^T \hat{X}_n$, the center of Θ_n is zero, i.e., Θ_n is a neighborhood of the origin of the Euclidean space R^d. In fact

$$\sum_{k=1}^{K+1} \theta_{n,k} = U_{n,1}^T \left(\sum_{k=1}^{K+1} x_{n_k} - (K+1)\bar{x}_n \right) = 0. \tag{6}$$

C. Alignment

For a patch $X_n = [x_{n_1} \ \ldots \ x_{n_{K+1}}]$, there are a global coordinate $Y_n = [y_{n_1} \ \ldots \ y_{n_{K+1}}]$ and a local coordinate $\Theta_n = [\theta_{n,1} \ \ldots \ \theta_{n,K+1}]$, the aim of alignment is to derive Y_n from Θ_n. To this end, an equation relating Y_n and Θ_n has to be established. This kind of equations is called alignment equation. The alignment equation used in LTSA is assumed to be

$$\hat{Y}_n = Y_n - \bar{y}_n \Gamma_{K+1}^T = A_n \Theta_n \tag{7}$$

where $\bar{y}_n = [1/(K+1)] \sum_{k=1}^{K+1} y_{n_k}$ is the center of Y_n, Γ_{K+1} is a $K+1$-dimensional vector whose elements are all 1, $\hat{Y}_n$ is called the centralized matrix of Y_n. In geometry, (7) means that the global coordinate Y_n can be approximated by translation, rotation and scaling of the local coordinate Θ_n.

Subsequently, LTSA uses the pseudo inverses of matrices to solve the alignment equation

$$\hat{Y}_n = A_n \Theta_n \Longrightarrow A_n = \hat{Y}_n \Theta_n^+ \tag{8}$$

where Θ_n^+ is the pseudo inverse of Θ_n, i.e., Θ_n^+ is the solution to the following problem:

$$\|I_d - \Theta_n \Theta_n^+\|^2 \underset{\text{choose } \Theta_n^+}{\longrightarrow} \min. \tag{9}$$

The above equation indicates that "choose Θ_n^+ so as to make $\|I_d - \Theta_n\Theta_n^+\|^2$ as small as possible."

Based on the pseudo inverse Θ_n^+, the local objective function can be formulated as follows:

$$\begin{aligned}\|\hat{Y}_n - A_n\Theta_n\|^2 &= \|\hat{Y}_n\big(I_{K+1} - \Theta_n^+\Theta_n\big)\|^2 \\ &= \|YS_nC_{K+1}\big(I_{K+1} - \Theta_n^+\Theta_n\big)\|^2 \\ &= \|YL_n\|^2 \underset{\text{choose } Y}{\longrightarrow} \min\end{aligned} \tag{10}$$

where $C_{K+1} = I_{K+1} - [1/(K+1)]\Gamma_{K+1}\Gamma_{K+1}^T$ is the centralizing matrix such that $\hat{Y}_n = Y_nC_{K+1}$, S_n is the selection matrix such that $Y_n = YS_n$, and $L_n = S_nC_{K+1}(I_{K+1} - \Theta_n^+\Theta_n)$.

The local objective function (10) only considers the case of one patch, taking all patches into account will generate the objective function of LTSA

$$\begin{aligned}\sum_{n=1}^{N}\|YL_n\|^2 &= \sum_{n=1}^{N} tr\big(YL_nL_n^TY^T\big) \\ &= tr\big(YLY^T\big) \underset{\text{choose } Y}{\longrightarrow} \min\end{aligned} \tag{11}$$

where $L = \sum_{n=1}^{N} L_nL_n^T$. In order to avoid trivial solutions, the objective function (11) is often solved under the constraint $YY^T = I_d$.

Remark 4: The solution to the objective function (11) is not unique. In fact, if Y is a solution to the objective function (11), then $\widetilde{Y} = OY$ is also a solution to the objective function (11), where $OO^T = I_d$.

Remark 5: In LTSA, $\Theta_n = U_{n,1}^T\hat{X}_n$ and $\hat{Y}_n = A_n\Theta_n$, then $\hat{Y}_n = (A_nU_{n,1}^T)\hat{X}_n$, this means that the global coordinate of a patch is the linear transformation of the patch. In [40], this linear transformation is called locally-linear transformation. Xiang *et al.* [41] further proved that in LLE the relation between the global coordinate of a patch and the patch itself can also be reformulated as a locally-linear transformation. Under the framework of locally-linear transformation, the connection and difference between LLE and LTSA has been discussed. In this paper, the relation between LTSA and another manifold learning algorithm HLLE is discussed. It should be noted that, although HLLE and LLE are similar by name, they are quite different in nature.

D. Local Coordinates With Row Full-Rank

If the local coordinate Θ_n is row full-rank, then its pseudo inverse Θ_n^+ can be expressed with its QR decomposition. In fact, if the local coordinate Θ_n is row full-rank, then the matrix $\Theta_n\Theta_n^T$ is invertible and the pseudo inverse Θ_n^+ can be expressed as

$$\Theta_n^+ = \Theta_n^T\big(\Theta_n\Theta_n^T\big)^{-1}. \tag{12}$$

On the other hand, since Θ_n is row full-rank, then the matrix Θ_n^T is column full-rank and can be QR-decomposed

$$\Theta_n^T = Q_n^{\text{LTSA}}R_n^{\text{LTSA}}. \tag{13}$$

Thus we have

$$\begin{aligned}I_{K+1} - \Theta_n^+\Theta_n &= I_{K+1} - \Theta_n^T\big(\Theta_n\Theta_n^T\big)^{-1}\Theta_n \\ &= I_{K+1} - Q_n^{\text{LTSA}}R_n^{\text{LTSA}}\Big(\Big(R_n^{\text{LTSA}}\Big)^T\Big(Q_n^{\text{LTSA}}\Big)^TQ_n^{\text{LTSA}}R_n^{\text{LTSA}}\Big)^{-1} \\ &\quad\times\Big(R_n^{\text{LTSA}}\Big)^T\Big(Q_n^{\text{LTSA}}\Big)^T \\ &= I_{K+1} - Q_n^{\text{LTSA}}\Big(Q_n^{\text{LTSA}}\Big)^T.\end{aligned} \tag{14}$$

Further, the local objective function (10) can be reformulated as

$$\begin{aligned}\Big\|\hat{Y}_n - A_n\Theta_n\Big\|^2 &= \Big\|\hat{Y}_n\big(I_{K+1} - \Theta_n^+\Theta_n\big)\Big\|^2 \\ &= \Big\|\hat{Y}_n\Big(I_{K+1} - Q_n^{\text{LTSA}}\Big(Q_n^{\text{LTSA}}\Big)^T\Big)\Big\|^2 \\ &\underset{\text{choose } \hat{Y}_n}{\longrightarrow} \min.\end{aligned} \tag{15}$$

This equation will be used to prove the equivalence between HLLE and LTSA in Section VII.

IV. HLLE Algorithm

HLLE is proposed in [11] and seems too complicated to be easy to understand, here we reformulate HLLE in our own way.

A. Theory

Let M be a d-dimensional manifold embedded in the D-dimensional Euclidean space R^D, where $d << D$, let O be the dimensionally-reduced version of M in the d-dimensional Euclidean space R^d and φ be the mapping between M and O, i.e., $\varphi : M \to O$. For all $x \in M$, $y = \varphi(x) = [\varphi^1(x)\dots\varphi^d(x)]^T \in R^d$, is called the global coordinate of x, where $\varphi^i : M \to R$ is the ith component function of φ, $i = 1, \dots, d$. Obviously, these component functions are the real-valued functions defined on the manifold M.

On the other hand, according to the definition of manifold, for all $x \in M$, there is a neighborhood $X_x \subseteq M$ of x such that the neighborhood X_x is homeomorphic to an open set Θ_x of the d-dimensional Euclidean space R^d. Let $\varphi_x : X_x \to \Theta_x$ be the homeomorphic mapping between X_x and Θ_x, φ_x is often called local homeomorphic mapping. Since translation will not damage homeomorphism, Without losing generality, we can assume that $\varphi_x(x) = 0$, which means that the open set Θ_x is around the origin of the d-dimensional Euclidean space R^d.

Now for each component function φ^i of the global homeomorphic mapping φ, by using the local homeomorphic mapping φ_x, we can define $g_x^i = \varphi^i \circ \varphi_x^{-1} : \Theta_x \to R$. According to the theory of differential manifold, g_x^i is called the local pullback function of φ^i and the differentiation of φ^i on X_x is defined as the differentiation of its local pullback function g_x^i on Θ_x. Note that, since the domain Θ_x of g_x^i is around the origin of d-dimensional Euclidean space R^d, we can then Taylor-expand g_x^i around the origin of the d-dimensional Euclidean space R^d.

For any $\theta' \in \Theta_x$, let $x' = \varphi_x^{-1}(\theta')$, then we have

$$\begin{aligned}\varphi^i(x') &= \varphi^i\left(\varphi_x^{-1}(\theta')\right) = \left(\varphi^i \circ \varphi_x^{-1}\right)(\theta') = g_x^i(\theta') \\ &= g_x^i(0) + \left(\nabla g_x^i(0)\right)^T\theta' + \frac{1}{2}(\theta')^T Hg_x^i(0)\theta' + \cdots \\ &= \varphi^i(x) + \left(\nabla g_x^i(0)\right)^T\theta' + \frac{1}{2}(\theta')^T Hg_x^i(0)\theta' + \cdots \quad (16)\end{aligned}$$

where

$$\nabla g_x^i(0) = \left.\begin{bmatrix}\frac{\partial g_x^i(\theta)}{\partial\theta^1} \\ \vdots \\ \frac{\partial g_x^i(\theta)}{\partial\theta^d}\end{bmatrix}\right|_{\theta=0} \in R^d$$

$$Hg_x^i(0) = \left.\begin{bmatrix}\frac{\partial^2 g_x^i(\theta)}{\partial\theta^1\partial\theta^1} & \cdots & \frac{\partial^2 g_x^i(\theta)}{\partial\theta^1\partial\theta^d} \\ \vdots & \ddots & \vdots \\ \frac{\partial^2 g_x^i(\theta)}{\partial\theta^d\partial\theta^1} & \cdots & \frac{\partial^2 g_x^i(\theta)}{\partial\theta^d\partial\theta^d}\end{bmatrix}\right|_{\theta=0} \in R^{d\times d}.$$

Furthermore, through the quadratic form transform, $(1/2)(\theta')^T Hg_x^i(0)\theta'$ can be converted into the scalar product of two vectors (see the Appendix)

$$\frac{1}{2}(\theta')^T Hg_x^i(0)\theta' = \left(h_x^i(0)\right)^T\vartheta' \quad (17)$$

where $h_x^i(0) \in R^{[d(d+1)/2]}$ is a vector whose components are composed of the elements of the Hessian matrix $Hg_x^i(0)$, $\vartheta' \in R^{[d(d+1)/2]}$ is also a vector whose components are composed of the quadratic terms of the components of θ'. Substituting (17) into (16) will give

$$\varphi^i(x') = \varphi^i(x) + \left(\nabla g_x^i(0)\right)^T\theta' + \left(h_x^i(0)\right)^T\vartheta' + \cdots \quad (18)$$

At last, taking into account all the component functions of the global homeomorphic mapping φ will give

$$\begin{aligned}y' = \varphi(x') &= \begin{bmatrix}\varphi^1(x') \\ \vdots \\ \varphi^d(x')\end{bmatrix} = \begin{bmatrix}\varphi^1(x) \\ \vdots \\ \varphi^d(x)\end{bmatrix} \\ &\quad + \begin{bmatrix}\left(\nabla g_x^1(0)\right)^T \\ \vdots \\ \left(\nabla g_x^d(0)\right)^T\end{bmatrix}\theta' + \begin{bmatrix}\left(h_x^1(0)\right)^T \\ \vdots \\ \left(h_x^d(0)\right)^T\end{bmatrix}\vartheta' + \cdots \\ &= \varphi(x) + A_x\theta' + H_x\vartheta' + \cdots \\ &= y + A_x\theta' + H_x\vartheta' + \cdots \quad (19)\end{aligned}$$

where

$$A_x = \begin{bmatrix}\left(\nabla g_x^1(0)\right)^T \\ \vdots \\ \nabla g_x^d(0))^T\end{bmatrix} \in R^{d\times d}$$

$$H_x = \begin{bmatrix}\left(h_x^1(0)\right)^T \\ \vdots \\ \left(h_x^d(0)\right)^T\end{bmatrix} \in R^{d\times\frac{d(d+1)}{2}}.$$

Equation (19) can be illustrated by Fig. 1. In Fig. 1, both x and x' are within the patch X_x and their local coordinates $\varphi_x(x) = 0$ and $\varphi_x(x') = \theta'$ are therefore within the open set Θ_x. However, the global coordinates of x and x', i.e., $y = \varphi(x)$ and $y' = \varphi(x')$, are not necessary within the open set Θ_x. Equation (19) shows the relation among $y = \varphi(x)$, $y' = \varphi(x')$, $\varphi_x(x) = 0$ and $\theta' = \varphi_x(x')$.

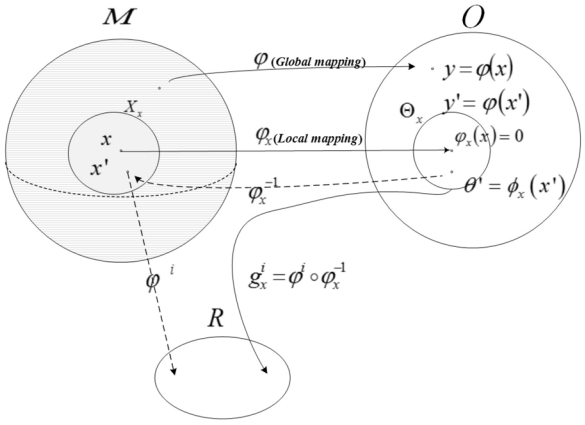


Fig. 1. Relation between global and local coordinates in theory.

B. Algorithm

1) Global and Local Coordinates: For each data point x_n, let $X_n = [x_{n_1}\ \ldots\ x_{n_k}] \in R^{D\times K}$ be the neighborhood matrix of x_n, the column vectors of X_n are composed of the KNNs of x_n. Note that, in HLLE algorithm, X_n does not include x_n. The global coordinate of X_n is denoted as

$$\begin{aligned}Y_n = \varphi(X_n) &= \left[\varphi(x_{n_1})\ \ldots\ \varphi(x_{n_K})\right] \\ &= \left[y_{n_1}\ \ldots\ y_{n_K}\right] \in R^{d\times K}. \quad (20)\end{aligned}$$

Let $\bar{x}_n = (1/K)\sum_{k=1}^K x_{n_k}$, $\bar{x}_n$ is the center of X_n. HLLE algorithm takes X_n as the neighborhood of $\bar{x}_n$, not as the neighborhood of x_n. The global coordinate of $\bar{x}_n$ is approximated by

$$\varphi(\bar{x}_n) = \varphi\left(\frac{1}{K}\sum_{k=1}^K x_{n_k}\right) \approx \frac{1}{K}\sum_{k=1}^K \varphi(x_{n_k}) = \frac{1}{K}\sum_{k=1}^K y_{n_k} = \bar{y}_n \quad (21)$$

$\bar{y}_n$ is not only the linear part of $\varphi(\bar{x}_n)$, but also the center of Y_n.

HLLE uses the same method as LTSA to construct the local homeomorphic mapping φ_n [see (4)]

$$\varphi_n(x) = U_{n,1}^T(x - \bar{x}_n).$$

It is clear that $\varphi_n(\bar{x}_n) = 0$. By using the local homeomorphic mapping φ_n, we can obtain the local coordinate Θ_n of X_n

$$\begin{aligned}\Theta_n = \varphi_n(X_n) &= \left[\varphi_n(x_{n_1})\ \ldots\ \varphi_n(x_{n_K})\right] \\ &= \left[U_{n,1}^T(x_{n_1} - \bar{x}_n)\ \ldots\ U_{n,1}^T(x_{n_K} - \bar{x}_n)\right] = U_{n,1}^T\hat{X}_n \\ &= \left[\theta_{n,1}\ \ldots\ \theta_{n,K}\right] \in R^{d\times K}. \quad (22)\end{aligned}$$

Obviously, the center of Θ_n is zero and therefore the local coordinate Θ_n is not only the neighborhood of $\varphi_n(\bar{x}_n)$, but also the neighborhood of the origin of the d-dimensional Euclidean space R^d.

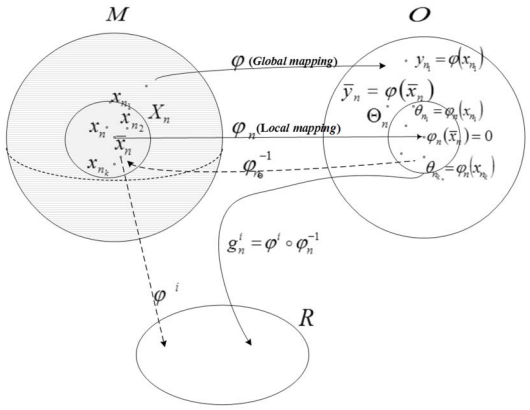


Fig. 2. Relation between global and local coordinates in algorithm.

Thus, according to the HLLE theory and (19), we have

$$y_{n_k} = \bar{y}_n + A_n\theta_{n,k} + H_n\vartheta_{n,k}, k = 1, \ldots, K. \tag{23}$$

Equation (23) can be rewritten in the matrix form

$$\begin{aligned} Y_n &= \left[y_{n_1} \ \ldots \ y_{n_K}\right] = \left[\bar{y}_n \ \ldots \ \bar{y}_n\right] \\ &\quad + A_n\left[\theta_{n,1} \ \ldots \ \theta_{n,K}\right] + H_n\left[\vartheta_{n,1} \ \ldots \ \vartheta_{n,K}\right] \\ &= \bar{y}_n\Gamma_K^T + A_n\Theta_n + H_n\Pi_n = \left[\bar{y}_n \ A_n \ H_n\right]\begin{bmatrix}\Gamma_K^T \\ \Theta_n \\ \Pi_n\end{bmatrix} \end{aligned} \tag{24}$$

where $\Gamma_K = [1 \ \ldots \ 1]^T \in R^K$, $\Pi_n = [\vartheta_{n,1} \ \ldots \ \vartheta_{n,K}] \in R^{[d(d+1)/2]\times K}$.

Equation (24) shows the relation between Y_n and Θ_n. Equation (24) is called the alignment equation which lays the foundation of HLLE' alignment.

Fig. 2 is the algorithmic version of Fig. 1. In Fig. 2, the center $\bar{x}_n$ of the patch X_n is assumed to be still within the patch X_n and its global and local coordinates are $\bar{y}_n = \varphi(\bar{x}_n)$ and $0 = \varphi_n(\bar{x}_n)$, respectively. Note that the global coordinate $\bar{y}_n$ is not necessary within the area of local coordinates Θ_n.

2) QR Decomposition: HLLE uses OR decomposition to solve the alignment equation (24). In fact, if the matrix $[\Gamma_K \ \Theta_n^T \ \Pi_n^T] \in R^{K\times[(d+1)(d+2)/2]}$ is column full-rank, it can be then QR-decomposed

$$\begin{aligned} \left[\Gamma_K \ \Theta_n^T \ \Pi_n^T\right] &= Q_n^{\text{HLLE}}R_n^{\text{HLLE}} \\ &= \left[Q_{n,1}^{\text{HLLE}} \ Q_{n,2}^{\text{HLLE}}\right]\begin{bmatrix}R_{n,11}^{\text{HLLE}} & R_{n,12}^{\text{HLLE}} \\ 0 & R_{n,22}^{\text{HLLE}}\end{bmatrix} \end{aligned} \tag{25}$$

where the matrix $Q_{n,1}^{\text{HLLE}} \in R^{K\times(d+1)}$ is composed of the first $d+1$ column vectors of Q_n^{HLLE}, the matrix $Q_{n,2}^{\text{HLLE}} \in R^{K\times[d(d+1)/2]}$ is composed of the last $[d(d+1)/2]$ column vectors of Q_n^{HLLE}. The matrices $R_{n,11}^{\text{HLLE}} \in R^{(d+1)\times(d+1)}$, $R_{n,12}^{\text{HLLE}} \in R^{(d+1)\times[d(d+1)/2]}$ and $R_{n,22}^{\text{HLLE}} \in R^{[d(d+1)/2]\times[d(d+1)/2]}$ are the corresponding block matrices of R_n^{HLLE}.

Further, we multiply (24) from both sides with the matrix $Q_{n,2}^{\text{HLLE}}((R_{n,22}^{\text{HLLE}})^T)^{-1}$

$$\begin{aligned} &Y_nQ_{n,2}^{\text{HLLE}}\left(\left(R_{n,22}^{\text{HLLE}}\right)^T\right)^{-1} \\ &\quad= \left[\bar{y}_n \ A_n \ H_n\right]\begin{bmatrix}\Gamma_K^T \\ \Theta_n \\ \Omega_n\end{bmatrix}Q_{n,2}^{\text{HLLE}}\left(\left(R_{n,22}^{\text{HLLE}}\right)^T\right)^{-1} \\ &\quad= \left[\bar{y}_n \ A_n \ H_n\right]\begin{bmatrix}\left(R_{n,11}^{\text{HLLE}}\right)^T & 0 \\ \left(R_{n,12}^{\text{HLLE}}\right)^T & \left(R_{n,22}^{\text{HLLE}}\right)^T\end{bmatrix} \\ &\qquad\times\begin{bmatrix}\left(Q_{n,1}^{\text{HLLE}}\right)^T \\ \left(Q_{n,2}^{\text{HLLE}}\right)^T\end{bmatrix}Q_{n,2}^{\text{HLLE}}\left(\left(R_{n,22}^{\text{HLLE}}\right)^T\right)^{-1} \\ &\quad= \left[\bar{y}_n \ A_n \ H_n\right]\begin{bmatrix}\left(R_{n,11}^{\text{HLLE}}\right)^T & 0 \\ \left(R_{n,12}^{\text{HLLE}}\right)^T & \left(R_{n,22}^{\text{HLLE}}\right)^T\end{bmatrix} \\ &\qquad\times\begin{bmatrix}0 \\ I_{\frac{d(d+1)}{2}}\end{bmatrix}\left(\left(R_{n,22}^{\text{HLLE}}\right)^T\right)^{-1} \\ &\quad= \left[\bar{y}_n \ A_n \ H_n\right]\begin{bmatrix}0 \\ \left(R_{n,22}^{\text{HLLE}}\right)^T\end{bmatrix}\left(\left(R_{n,22}^{\text{HLLE}}\right)^T\right)^{-1} \\ &\quad= \left[\bar{y}_n \ A_n \ H_n\right]\begin{bmatrix}0 \\ I_{\frac{d(d+1)}{2}}\end{bmatrix} = H_n. \end{aligned} \tag{26}$$

HLLE assumes that $H_n = 0$, then the local objective function of HLLE turns out to be

$$\begin{aligned} &Y_nQ_{n,2}^{\text{HLLE}}\left(\left(R_{n,22}^{\text{HLLE}}\right)^T\right)^{-1} = H_n = 0 \\ &\qquad\Rightarrow \left\|Y_nQ_{n,2}^{\text{HLLE}}\right\|^2 \underset{\text{choose } Y_n}{\longrightarrow} \min. \end{aligned} \tag{27}$$

The local objective function (27) only consider the case of a data point x_n, taking all data points into account will generate the object function of HLLE

$$\begin{aligned} \sum_{n=1}^{N}\left\|Y_nQ_{n,2}^{\text{HLLE}}\right\|^2 &= \sum_{n=1}^{N}\left\|YS_nQ_{n,2}^{\text{HLLE}}\right\|^2 = \sum_{n=1}^{N}\|YL_n\|^2 \\ &= \sum_{n=1}^{N}tr\left(YL_nL_n^TY^T\right) = tr\left(Y\left(\sum_{n=1}^{N}L_nL_n^T\right)Y^T\right) \\ &= tr\left(YLY^T\right) \underset{\text{choose } Y}{\longrightarrow} \min \end{aligned} \tag{28}$$

where $S_n \in R^{N\times K}$ is the selection matrix such that $Y_n = YS_n$, $L_n = S_nQ_{n,2}^{\text{HLLE}} \in R^{N\times[d(d+1)/2]}$, $L = \sum_{n=1}^{N}L_nL_n^T \in R^{N\times N}$. Again, the objective function (28) is often solved under the constraint $YY^T = I_d$.

Again, the solution to the objective function (28) is not unique. The orthogonal transformation of a solution to the objective function (28) is still a solution to the objective function (28).

V. Simplified HLLE Algorithm

The original HLLE can be simplified and the sHLLE is denoted as sHLLE. In fact, the alignment equation (24) can

be rearranged as follows:

$$\hat{Y}_n = Y_n - \bar{y}_n \Gamma_K^T = A_n \Theta_n + H_n \Pi_n = [A_n \ H_n] \begin{bmatrix} \Theta_n \\ \Pi_n \end{bmatrix}. \quad (29)$$

Then it is the matrix $[\Theta_n^T \ \Pi_n^T]$, not the matrix $[\Gamma_k \ \Theta_n^T \ \Pi_n^T]$ that is QR-decomposed in sHLLE. Equation (29) is the alignment equation of sHLLE.

sHLLE reduces not only the computational complexity, but also the possibility of failure of QR decomposition. According to the theory of QR decomposition, the matrix to be QR-decomposed must be column full-rank. If the matrix $[\Gamma_k \ \Theta_n^T \ \Pi_n^T]$ is not column full-rank, the matrix $[\Theta_n^T \ \Pi_n^T]$ is still possible to be column full-rank and can be QR-decomposed.

The QR decomposition of the matrix $[\Theta_n^T \ \Pi_n^T] \in R^{K\times(d+[d(d+1)/2])}$ is given by

$$\begin{aligned} \left[\Theta_n^T \ \Pi_n^T\right] &= Q_n^{\text{sHLLE}} R_n^{\text{sHLLE}} \\ &= \left[Q_{n,1}^{\text{sHLLE}} \ Q_{n,2}^{\text{sHLLE}}\right] \begin{bmatrix} R_{n,11}^{\text{sHLLE}} & R_{n,12}^{\text{sHLLE}} \\ 0 & R_{n,22}^{\text{sHLLE}} \end{bmatrix} \end{aligned} \quad (30)$$

where the matrix $Q_{n,1}^{\text{sHLLE}} \in R^{K\times d}$ is composed of the first d column vectors of Q_n^{sHLLE}, the matrix $Q_{n,2}^{\text{sHLLE}} \in R^{K\times[d(d+1)/2]}$ is composed of the last $[d(d+1)/2]$ column vectors of Q_n^{sHLLE} and the matrices $R_{n,11}^{\text{sHLLE}} \in R^{d\times d}$, $R_{n,12}^{\text{sHLLE}} \in R^{d\times[d(d+1)/2]}$ and $R_{n,22}^{\text{sHLLE}} \in R^{[d(d+1)/2]\times[d(d+1)/2]}$ are the corresponding block matrices of R_n^{sHLLE}.

Similarly, we multiply the alignment equation (29) from both sides with the matrix $Q_{n,2}^{\text{sHLLE}}((R_{n,22}^{\text{sHLLE}})^T)^{-1}$

$$\begin{aligned} &\hat{Y}_n Q_{n,2}^{\text{sHLLE}} \left(\left(R_{n,22}^{\text{sHLLE}}\right)^T\right)^{-1} \\ &= [A_n \ H_n] \begin{bmatrix} \Theta_n \\ \Gamma_n \end{bmatrix} Q_{n,2}^{\text{sHLLE}} \left(\left(R_{n,22}^{\text{sHLLE}}\right)^T\right)^{-1} \\ &= [A_n \ H_n] \begin{bmatrix} \left(R_{n,11}^{\text{sHLLE}}\right)^T & 0 \\ \left(R_{n,12}^{\text{sHLLE}}\right)^T & \left(R_{n,22}^{\text{sHLLE}}\right)^T \end{bmatrix} \begin{bmatrix} \left(Q_{n,1}^{\text{sHLLE}}\right)^T \\ \left(Q_{n,2}^{\text{sHLLE}}\right)^T \end{bmatrix} \\ &\quad \times Q_{n,2}^{\text{sHLLE}} \left(\left(R_{n,22}^{\text{sHLLE}}\right)^T\right)^{-1} \\ &= [A_n \ H_n] \begin{bmatrix} \left(R_{n,11}^{\text{sHLLE}}\right)^T & 0 \\ \left(R_{n,12}^{\text{sHLLE}}\right)^T & \left(R_{n,22}^{\text{sHLLE}}\right)^T \end{bmatrix} \begin{bmatrix} 0 \\ I_{\frac{d(d+1)}{2}} \end{bmatrix} \\ &\quad \times \left(\left(R_{n,22}^{\text{sHLLE}}\right)^T\right)^{-1} \\ &= [A_n \ H_n] \begin{bmatrix} 0 \\ \left(R_{n,22}^{\text{sHLLE}}\right)^T \end{bmatrix} \left(\left(R_{n,22}^{\text{sHLLE}}\right)^T\right)^{-1} \\ &= [A_n \ H_n] \begin{bmatrix} 0 \\ I_{\frac{d(d+1)}{2}} \end{bmatrix} = H_n = 0. \end{aligned} \quad (31)$$

Further, since $R_{n,22}^{\text{sHLLE}}$ is invertible, then the local objective function of sHLLE turns out to be

$$\begin{aligned} &\hat{Y}_n Q_{n,2}^{\text{sHLLE}} \left(\left(R_{n,22}^{\text{sHLLE}}\right)^T\right)^{-1} = 0 \Rightarrow \hat{Y}_n Q_{n,2}^{\text{sHLLE}} = 0 \\ &\quad \Rightarrow \left\| \hat{Y}_n Q_{n,2}^{\text{sHLLE}} \right\|^2 = \left\| Y_n C_K Q_{n,2}^{\text{sHLLE}} \right\|^2 \underset{\text{choose } Y_n}{\longrightarrow} \min \end{aligned} \quad (32)$$

where C_K is the centralizing matrix such that $\hat{Y}_n = Y_n C_K$.

Again, the local objective function (32) only consider the case of a data point x_n, taking all data points into account will give

$$\begin{aligned} \sum_{n=1}^{N} \left\| \hat{Y}_n Q_{n,2}^{\text{sHLLE}} \right\|^2 &= \sum_{n=1}^{N} \left\| Y_n C_K Q_{n,2}^{\text{sHLLE}} \right\|^2 \\ &= \sum_{n=1}^{N} \left\| Y S_n C_K Q_{n,2}^{\text{sHLLE}} \right\|^2 = \sum_{n=1}^{N} \| Y L_n \|^2 \\ &= \sum_{n=1}^{N} tr\left(Y L_n L_n^T Y^T\right) = tr\left(Y \left(\sum_{n=1}^{N} L_n L_n^T\right) Y^T\right) \\ &= tr\left(Y L Y^T\right) \underset{\text{choose } Y}{\longrightarrow} \min \end{aligned} \quad (33)$$

where S_n is the selection matrix such that $Y_n = Y S_n$, $L_n = S_n C_K Q_{n,2}^{\text{sHLLE}}$, $L = \sum_{n=1}^{N} L_n L_n^T$. Again, the objective function (33) is often solved under the constraint $YY^T = I_d$.

sHLLE is exactly the same as HLLE. The improvement of sHLLE to HLLE is only computationally tricky. Therefore, from now on, HLLE is sHLLE in this paper.

VI. Improved HLLE Algorithm

Although the patch $X_n = [x_{n_1} \ \dots \ x_{n_k}]$ is generated based on the data point x_n, however, once the patch X_n is generated, HLLE no longer takes it as the neighborhood of x_n, but the neighborhood of $\bar{x}_n$, where $\bar{x}_n = (1/K)\sum_{k=1}^{K} x_{n_k}$ is the center of the patch X_n. That is to say, the data point x_n disappears from X_n and $\bar{x}_n$, and would not play any role the subsequent stages.

In order to make full use of x_n, an iHLLE is proposed here. The only difference between iHLLE and HLLE is that, in iHLLE, the patch X_n includes not only the KNNs of x_n, but also x_n itself. Specific stages of iHLLE are as follows.

1) *Finite Open Cover:* Let $x_{n_1} \ \dots \ x_{n_k}$ be the KNNs of x_n, then the patch is constructed as follows:

$$\begin{aligned} X_n &= \left[x_{n_1} \ \dots \ x_{n_K} \ x_n\right] \\ &= \left[x_{n_1} \ \dots \ x_{n_K} \ x_{n_{K+1}}\right] \in R^{D\times(K+1)} \end{aligned} \quad (34)$$

where $x_{n_{K+1}} = x_n$.

2) *Local Homeomorphism:* Let $\bar{x}_n = [1/K+1]\sum_{k=1}^{K+1} x_{n_k}$, $\bar{x}_n$ is the center of X_n. iHLLE regards X_n as the neighborhood of $\bar{x}_n$, not the neighborhood of x_n, and then uses the PCA method to construct the local homeomorphic mapping φ_n

$$\varphi_n(x) = U_{n,1}^T (x - \bar{x}_n)$$

where $U_{n,1}$ is composed of the first d column vectors of the matrix U_n, U_n comes from the SVD decomposition of the centralized matrix $\hat{X}_n$. It is clear that $\varphi_n(\bar{x}_n) = 0$. Based on the local homeomorphic mapping φ_n, the local coordinate Θ_n of X_n is then given by

$$\begin{aligned} \Theta_n &= \varphi_n(X_n) = \left[\theta_{n,1} \ \dots \ \theta_{n,K} \ \theta_{n,K+1}\right] \\ &= U_{n,1}^T \hat{X}_n \in R^{d\times(K+1)}. \end{aligned} \quad (35)$$

It can be seen from (35) that, since the center of $\hat{X}_n$ is zero, the center of Θ_n is then also zero. Therefore,

the local coordinate of Θ_n is also a neighborhood of the origin of the Euclidean space R^d.

3) *Alignment:* According to the deduction of HLLE, the alignment equation (29) is

$$\hat{Y}_n = Y_n C_{K+1} = A_n\Theta_n + H_n\Pi_n = [A_n\ H_n]\begin{bmatrix}\Theta_n\\ \Pi_n\end{bmatrix} \quad (36)$$

where $C_{K+1} = I_{K+1} - [1/(K+1)]\Gamma_{K+1}\Gamma_{K+1}^T$ is the centralizing matrix. The deduction of objective function of iHLLE is exactly the same as that of HLLE.

It can be seen by comparing HLLE and iHLLEs that, in the local area around each data point x_n, HLLE uses $K+1$ data: $x_{n_1}, \ldots, x_{n_K}, \bar{x}_n^{\text{HLLE}}$, while iHLLE uses $K+2$ data: $x_{n_1}, \ldots, x_{n_K}, x_n, \bar{x}_n^{\text{iHLLE}}$, where $x_{n_1}, \ldots, x_{n_K}$ is the KNNs of x_n, $\bar{x}_n^{\text{HLLE}} = (1/K)\sum_{k=1}^{K} x_{n_k}$ and $\bar{x}_n^{\text{iHLLE}} = [1/(K+1)](\sum_{k=1}^{K} x_{n_k} + x_n)$. Although the data $x_{n_1}, \ldots, x_{n_K}$ are generated based on x_n, HLLE does not use x_n any longer in the following stages and regards the data $x_{n_1}, \ldots, x_{n_K}$ as the neighborhood of $\bar{x}_n^{\text{HLLE}}$, not the neighborhood of x_n. By contrast, iHLLE continues to use x_n in the subsequent stages and regards the data $x_{n_1}, \ldots, x_{n_K}, x_n$ as the neighborhood of $\bar{x}_n^{\text{iHLLE}}$. Since iHLLE makes better use of data than HLLE, it can be expected that iHLLE will perform better than HLLE in some applications.

VII. Equivalence Between HLLE and LTSA

In this paper, we distinguish between being equivalent and being identical. Being equivalent means "be the same in essence, but can be different in some trivial details," while being identical means "be exactly the same without any difference." Being identical is a special case of being equivalent.

In this section, we first prove that iHLLE is not only equivalent to LTSA, but can even be identical to LTSA. Then we prove that HLLE is equivalent to LTSA.

A. Identical Relation Between iHLLE and LTSA

It will be seen by comparing iHLLE and LTSA that these two algorithms are equivalent to each other.

1) In the first stage of manifold learning, i.e., the stage of finite open cover, the patches X_n^{LTSA} and X_n^{iHLLE} constructed by LTSA and iHLLEs, respectively, are exactly the same, they are all composed of the KNNs $x_{n_1}, \ldots, x_{n_K}$ of x_n and x_n itself, that is

$$\begin{aligned} X_n^{\text{LTSA}} = X_n^{\text{iHLLE}} &= \left[x_{n_1}\ \ldots\ x_{n_K}\ x_{n_{K+1}}\right] \\ &= X_n \in R^{D\times(K+1)} \end{aligned} \quad (37)$$

where $x_{n_{K+1}} = x_n$.

2) In the second stage of manifold learning, i.e., the stage of local homeomorphism, both LTSA and iHLLEs take the patch X_n as the neighborhood of $\bar{x}_n = [1/(K+1)](\sum_{k=1}^{K+1} x_{n_k})$, not the neighborhood of x_n, and then use the PCA method to build up the local homeomorphic mapping φ_n [see (4)]

$$\varphi_n(x) = U_{n,1}^T(x - \bar{x}_n) \in R^d.$$

Therefore, the local coordinates Θ_n^{LTSA} and Θ_n^{iHLLE} are the same, that is

$$\begin{aligned} \Theta_n^{\text{LTSA}} &= \Theta_n^{\text{iHLLE}} = \varphi_n(X_n) \\ &= \left[\varphi_n(x_{n_1})\ \ldots\ \varphi_n(x_{n_K})\ \varphi_n(x_{n_{K+1}})\right] \\ &= \left[\theta_{n,1}\ \ldots\ \theta_{n,K}\ \theta_{n,K+1}\right] = \Theta_n \in R^{d\times(K+1)}. \end{aligned} \quad (38)$$

3) In the third stage of manifold learning, i.e., the stage of alignment, the alignment equation relating Y_n^{LTSA} and Θ_n in LTSA is assumed to be (7)

$$\hat{Y}_n^{\text{LTSA}} = A_n\Theta_n$$

while the alignment equation relating Y_n^{iHLLE} and Θ_n in iHLLE is deduced to be (29)

$$\hat{Y}_n^{\text{iHLLE}} = A_n\Theta_n + H_n\Pi_n.$$

At the first glance, these two alignment equations seem different. However, if we carefully examine the deduction of iHLLE's alignment, we can find that the above difference is only formal. In the deduction of iHLLE's alignment, the matrix H_n is assumed to be zero, i.e., $H_n = 0$ [see (27) or (31)], which means that the alignment equation of iHLLE is

$$\hat{Y}_n^{\text{iHLLE}} = A_n\Theta_n + H_n\Pi_n = A_n\Theta_n \quad (39)$$

That is to say, both LTSA and iHLLEs are based on the same alignment equation to align their local coordinates (to deduce their object functions). The only difference between LTSA and iHLLE is that, LTSA uses the pseudo inverses of matrices to solve the alignment equation $\hat{Y}_n^{\text{LTSA}} = A_n\Theta_n$, while iHLLE uses QR decomposition of matrices to slove the alignment equation $\hat{Y}_n^{\text{iHLLE}} = A_n\Theta_n$. This difference is tricky, not essential. Therefore, iHLLE and LTSA algorithms are actually equivalent to each other.

Furthermore, if the size of neighborhood (the number of neighbors K) is properly chosen, iHLLE's solution to the alignment equation, i.e., the objective function of iHLLE, will be even identical to that of LTSA.

Theorem 1: If $K+1 = d + [d(d+1)/2]$, then the objective functions of iHLLE and LTSA are exactly the same without any difference, where K is the number of neighbors and d is the manifold's dimension.

Proof: The proof can be divided into five stages:

1) In iHLLE, the matrix $[\Theta_n^T\ \Pi_n^T]$ is assumed to column full-rank and therefore can be QR decomposed

$$\begin{aligned} \left[\Theta_n^T\ \Pi_n^T\right] &= Q_n^{\text{iHLLE}} R_n^{\text{iHLLE}} \\ &= \left[Q_{n,1}^{\text{iHLLE}}\ Q_{n,2}^{\text{iHLLE}}\right]\begin{bmatrix} R_{n,11}^{\text{iHLLE}} & R_{n,12}^{\text{iHLLE}} \\ 0 & R_{n,22}^{\text{sHLLE}}\end{bmatrix} \end{aligned} \quad (40)$$

where $Q_{n,1}^{\text{iHLLE}} \in R^{(K+1)\times d}$, $Q_{n,2}^{\text{iHLLE}} \in R^{(K+1)\times(d(d+1)/2)}$, $R_{n,11}^{\text{iHLLE}} \in R^{d\times d}$, $R_{n,22}^{\text{iHLLE}} \in R^{[d(d+1)/2]\times[d(d+1)/2]}$, and $R_{n,12}^{\text{iHLLE}} \in R^{d\times[d(d+1)/2]}$.

2) In iHLLE, the local objective function is as follows [see (32), $Q_{n,2}^{\text{sHLLE}} = Q_{n,2}^{\text{iHLLE}}$]:
$f_{\text{iHLLE}}(\hat{Y}_n) = \|\hat{Y}_n Q_{n,2}^{\text{iHLLE}}\|^2 \longrightarrow_{\text{choose } Y_n} \min$.

3) Since the matrix $[\Theta_n^T\ \Pi_n^T]$ is column full-rank, then the matrix Θ_n^T must be also column full-rank. Furthermore, the QR decomposition of Θ_n^T can be expressed as

$$\Theta_n^T = Q_{n,1}^{\mathrm{iHLLE}} R_{n,11}^{\mathrm{iHLLE}}. \tag{41}$$

In LTSA, the local objective function will be as follows [see (15), $Q_n^{\mathrm{LTSA}} = Q_{n,1}^{\mathrm{iHLLE}}$]:

$$f_{\mathrm{LTSA}}\left(\hat{Y}_n\right) = \left\| \hat{Y}_n \left(I_{K+1} - Q_{n,1}^{\mathrm{iHLLE}} \left(Q_{n,1}^{\mathrm{iHLLE}} \right)^T \right) \right\|^2 \underset{\text{choose } Y_n}{\longrightarrow} \min. \tag{42}$$

4) The size of the matrix $[\Theta_n^T\ \Pi_n^T]$ is $(K+1) \times (d + (d(d+1)/2))$. If $K+1 = d + (d(d+1)/2)$, then the matrix $[\Theta_n^T\ \Pi_n^T]$ is square and invertible and the matrix Q_n^{iHLLE} is then orthonormal, that is

$$\begin{aligned} I_{K+1} &= Q_n^{\mathrm{iHLLE}} \left(Q_n^{\mathrm{iHLLE}} \right)^T \\ &= \left[Q_{n,1}^{\mathrm{iHLLE}}\ Q_{n,2}^{\mathrm{iHLLE}} \right] \begin{bmatrix} \left(Q_{n,1}^{\mathrm{iHLLE}} \right)^T \\ \left(Q_{n,2}^{\mathrm{iHLLE}} \right)^T \end{bmatrix} \\ &= Q_{n,1}^{\mathrm{iHLLE}} \left(Q_{n,1}^{\mathrm{iHLLE}} \right)^T + Q_{n,2}^{\mathrm{iHLLE}} \left(Q_{n,2}^{\mathrm{iHLLE}} \right)^T. \end{aligned} \tag{43}$$

5) Substituting (43) into (42) generates the following result:

$$\begin{aligned} f_{\mathrm{LTSA}}\left(\hat{Y}_n\right) &= \left\| \hat{Y}_n \left(I_{K+1} - Q_{n,1}^{\mathrm{iHLLE}} \left(Q_{n,1}^{\mathrm{iHLLE}} \right)^T \right) \right\|^2 \\ &= \left\| \hat{Y}_n Q_{n,2}^{\mathrm{iHLLE}} \left(Q_{n,2}^{\mathrm{iHLLE}} \right)^T \right\|^2 \\ &= tr\left(\hat{Y}_n Q_{n,2}^{\mathrm{iHLLE}} \left(Q_{n,2}^{\mathrm{iHLLE}} \right)^T Q_{n,2}^{\mathrm{iHLLE}} \left(Q_{n,2}^{\mathrm{iHLLE}} \right)^T \hat{Y}_n^T \right) \\ &= tr\left(\hat{Y}_n Q_{n,2}^{\mathrm{iHLLE}} \left(Q_{n,2}^{\mathrm{iHLLE}} \right)^T \hat{Y}_n^T \right) \\ &= \left\| \hat{Y}_n Q_{n,2}^{\mathrm{iHLLE}} \right\|^2 = f_{\mathrm{iHLLE}}\left(\hat{Y}_n\right). \end{aligned} \tag{44}$$

In the above deduction, we exploit the result $(Q_{n,2}^{\mathrm{iHLLE}})^T Q_{n,2}^{\mathrm{iHLLE}} = I_{(d(d+1)/2)}$.

Equation (44) shows that the local objective functions of LTSA and iHLLE are exactly the same without any difference.

B. Equivalent Relation Between HLLE and LTSA

It has been long believed in manifold learning that the difference between HLLE and LTSA lies in the alignment, not in the neighborhood construction. Compared with LTSA's alignment, HLLE's alignment seems much more complicated and different. However, the introduction of iHLLE can correct this misunderstanding. As shown in Section VII-A, iHLLE is exactly the same as LTSA in the first two stages of manifold learning, while in the last stage of manifold learning, i.e., in the stage of alignment, iHLLE is exactly the same as HLLE. The theorem proven in Section VII-A shows that, although iHLLE and LTSA use different methods to solve the alignment equation, the solution, i.e., the local objective function, can be exactly the same! That is to say, iHLLE is identical to LTSA without any difference.

On other words, if HLLE adopts LTSA's method to construct neighborhoods of data points (at this time, HLLE becomes iHLLE), HLLE can be then exactly the same with LTSA without any difference. Therefore, the real difference between HLLE and LTSA is not the different methods of alignment, but the different methods of neighborhood construction. However, as recognized widely, the difference of whether to include a data point into its neighborhood is too trivial to be essential. Based on these arguments, we claim that HLLE is equivalent to LTSA.

VIII. Experimental Results

The correctness of our conclusion on the equivalence between LTSA and HLLE first comes from the rigorous mathematical deduction. However, the conclusion can also be justified experimentally by using manifold learning MATLAB demo (MANI), a widely-used platform of manifold learning. MANI integrates seven representative algorithms of manifold learning (MDS [16], Isomap [1], [2], LLE [3], LE [10], HLLE [11], LTSA [12], and diffusion map [14]) and nine commonly-used manifolds. MANI can be downloaded from the website: http://www.math.ucla.edu/∼wittman/mani/.

A. Experiments on Toy Data

We use MANI to test HLLE, iHLLE, and LTSA on all nine manifolds. When testing iHLLE, no additional programming is required. All one has to do is to replace X_n^{HLLE} with X_n^{iHLLE} for each patch, i.e., include the data points into their own neighborhoods, and then run HLLE on MANI, the results produced by MANI is the results of iHLLE.

Fig. 3 shows the experimental results on toy data. In Fig. 3, the first column is the manifold data, and the second, third and fourth columns are the experiment results of iHLLE, LTSA, and HLLE, respectively. Both manifold data and experimental results are produced by MANI. When testing iHLLE, the neighborhoods of data points must include the data points themselves, just like the neighborhoods of data points in LTSA. It can be seen from Fig. 3 that the experimental results of HLLE, iHLLE, and LTSA are much alike.

B. Experiments on Real World Data

Fig. 4 shows the experimental results of HLLE, iHLLE, and LTSA on the real world data, Frey Face. Frey Face is a data set produced by Brendan Frey and often used to test the effects of manifold learning algorithms in [1], [12], [14], and [16]. The images in Frey Face are all taken from a small video of Brendan Frey in which he only changes his head poses and facial expressions. Therefore, although the dimension of images is 560, the intrinsic dimension of these images is 2: head pose and facial expression. In Fig. 4, the data points with the same colors correspond to the same images which are also shown next to these data points. It is clear that the experimental results of HLLE, iHLLE, and LTSA are much alike.

Fig. 5 shows the experimental results of HLLE, iHLLE, and LTSA on another real world data, Plaster. Plaster is also

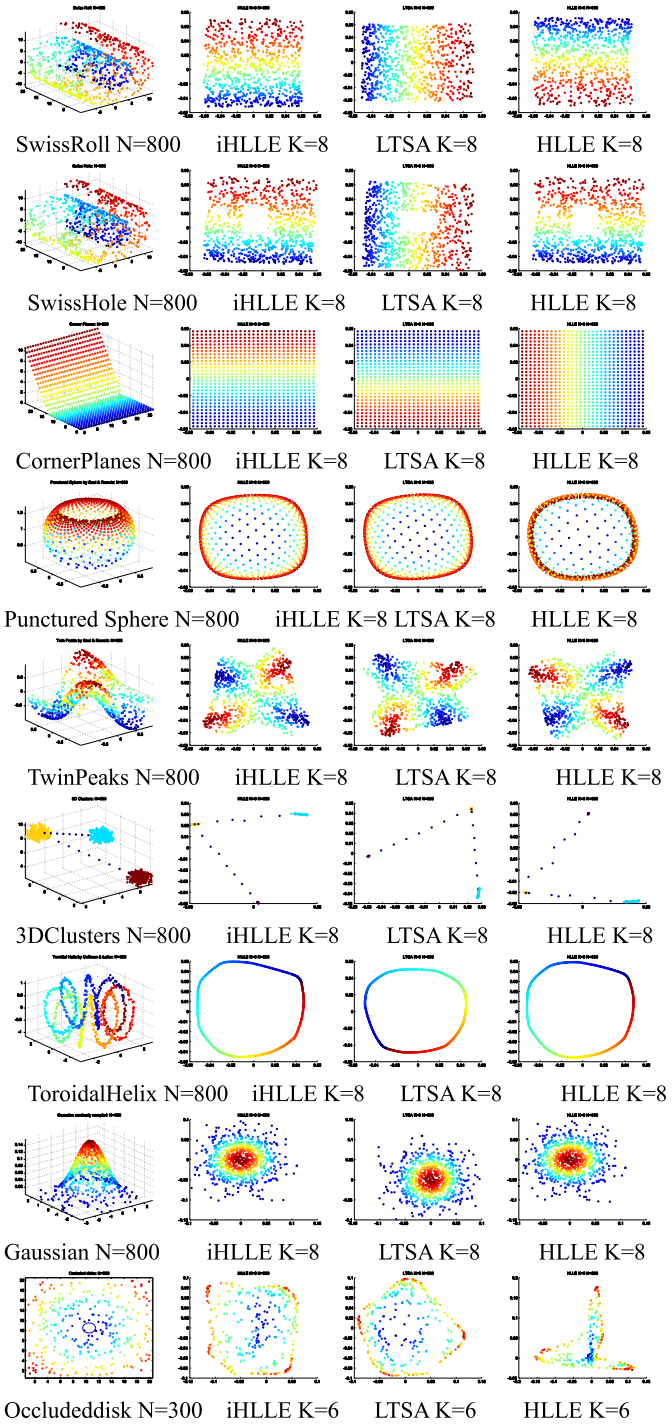


Fig. 3. Experimental results of HLLE, iHLLE, and LTSA on toy data. In the figure, the first column is the manifold data, and the second, third, and fourth columns are the experimental results of iHLLE, LTSA, and HLLE, respectively. Both manifold data and experimental results are produced by MANI.

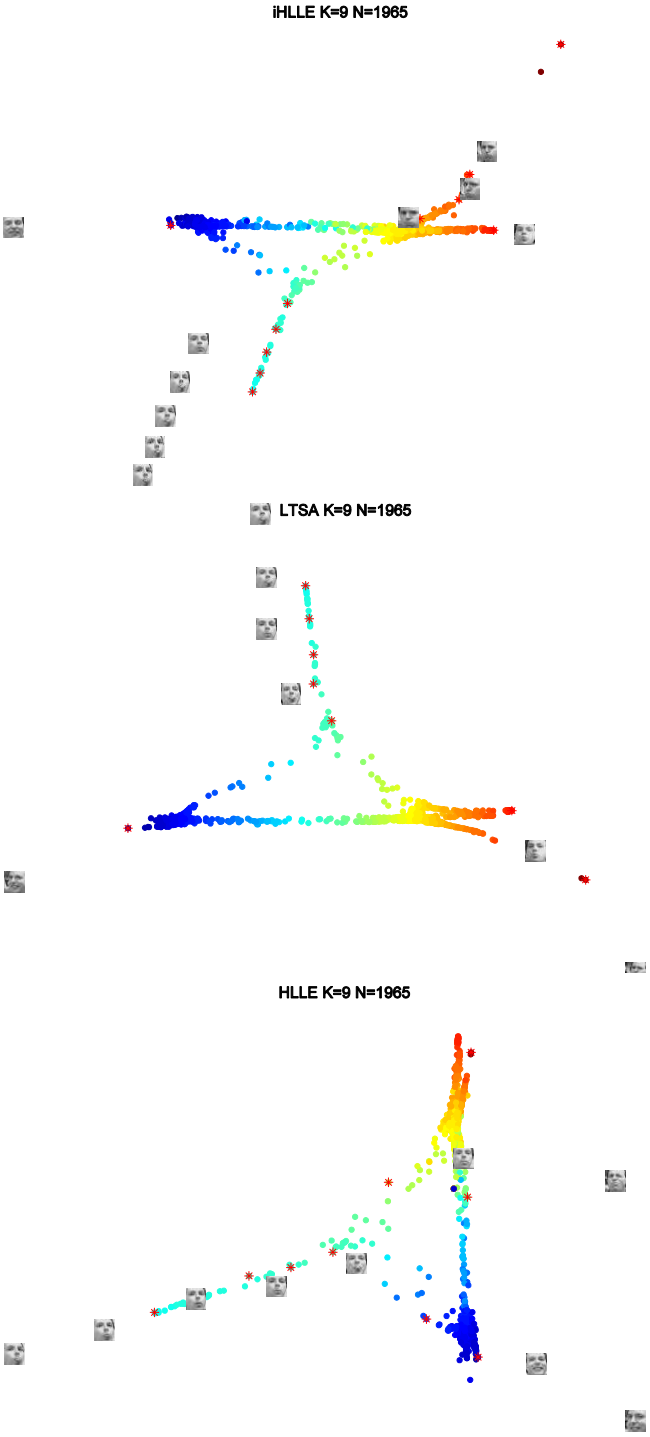
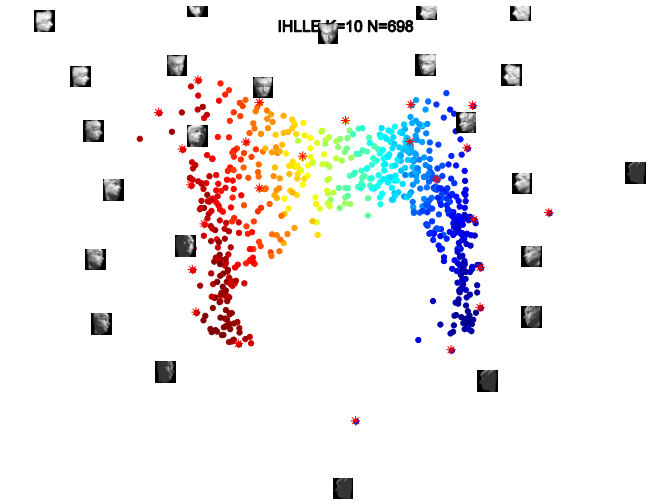
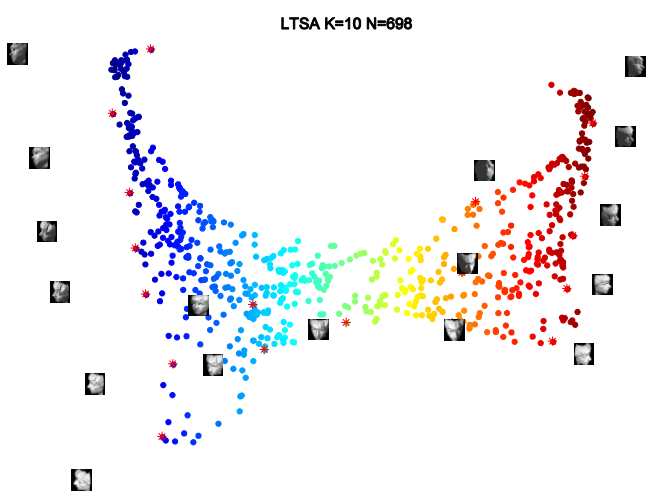


Fig. 4. Experimental results of HLL, iHLL, and LTSA on Frey Face. In the figure, the data points with the same colors correspond to the same images which are also shown next to these data points.

a data set often used in many academic literatures about manifold learning [2], [14]. The images of Plaster are all taken from the same plaster statue from different shooting angles and illuminations. Therefore, although the dimension of images is 4096, the intrinsic dimension of images is 2: shooting angle and illumination. In Fig. 5, the data points with the same colors correspond to the same images which are also shown next to these data points. Again, the experimental results of HLLE, iHLLE, and LTSA are much alike.

Fig. 6 shows the experimental results of HLLE, iHLLE, and LTSA on the real world data, MNIST. MNIST consists of the images of 0–9 handwritten digits and is often used in many academic literatures about manifold learning [42]–[45]. In Fig. 6, the images of handwritten digit 4 are taken from





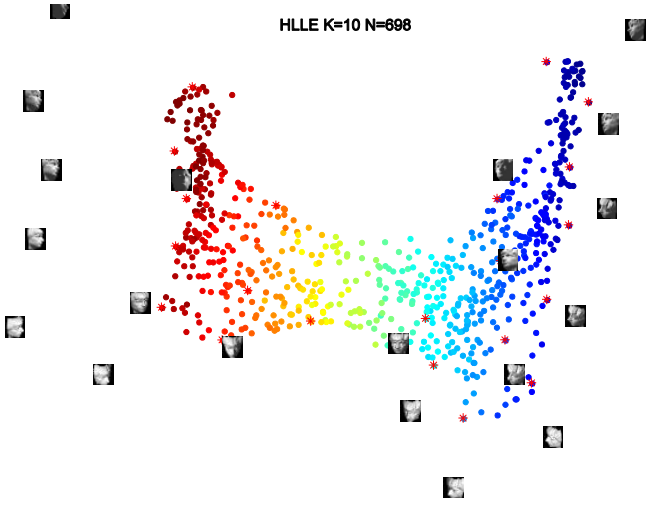
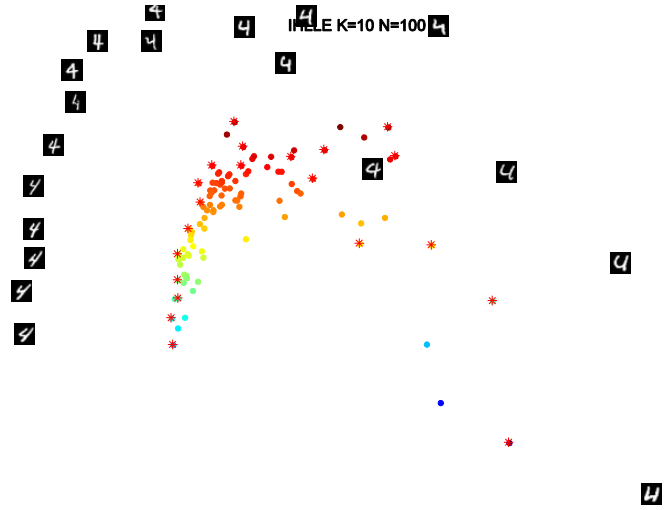
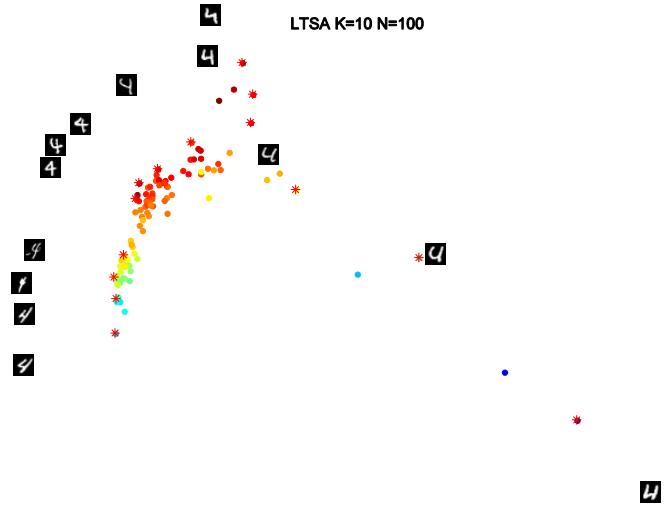


Fig. 5. Experimental results of HLLE, iHLLE, and LTSA on Plaster. In the figure, the data points with the same colors correspond to the same images which are also shown next to these data points.





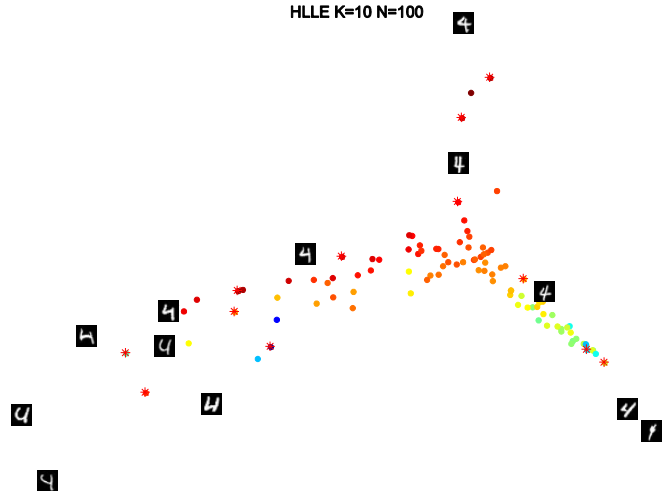


Fig. 6. Experimental results of HLLE, iHLLE, and LTSA on MNIST. In the figure, the data points with the same colors correspond to the same images which are also shown next to these data points.

MNIST and dimensionally reduced to the 2-D plane. In Fig. 6, the data points with the same colors correspond to the same images which are also shown next to these data points. Again, the experimental results of HLLE, iHLLE, and LTSA are much alike.

Fig. 7 shows the experimental results of iHLLE and LTSA on the real world data Plaster, where $d = 2$ and $K = 4$, i.e., d and K satisfy the relation $K + 1 = d + d(d + 1)/2$, as indicated in the theorem proven in Section VII. In this

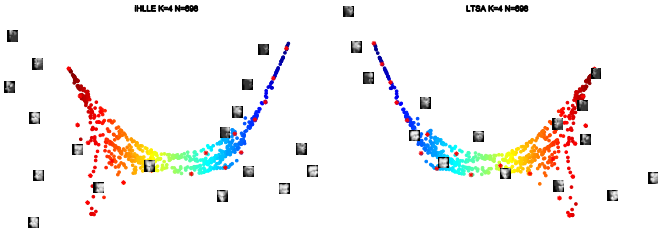


Fig. 7. Experimental results of iHLLE and LTSA on Plaster where $d = 2$ and $K = 4$, the data points with the same colors correspond to the same images which are also shown next to these data points.

TABLE I
DIFFERENCES BETWEEN HLLE, IHLLE, AND LTSA

	HLLE	iHLLE	LTSA
Construction of Neighborhoods	X_n^{HLLE} does not contain x_n	X_n^{iHLLE} contain x_n	X_n^{LTSA} contain x_n
Alignment	QR Decomposition	QR Decomposition	Pseudo Inverse
where $X_n^{iHLLE} = X_n^{LTSA} = [x_{n_1} \dots x_{n_K} x_n] \neq [x_{n_1}, \dots, x_{n_K}] = X_n^{HLLE}$			

case, both mathematical proof and experimental verification show that iHLLE and LTSA are exactly the same without any difference. However, it may be worth noting that HLLE fails in this case. This is because the condition of QR decomposition cannot be met in some local parts of manifold. iHLLE is an improvement to HLLE and avoids the defect of HLLE to some extent, as argued in Sections V and VI.

IX. CONCLUSION

Here some conclusions are presented as follows:

1) There are two differences between HLLE and LTSA. First, LTSA includes a data point into its neighborhood, while HLLE does not. Second, HLLE and LTSA use different methods to solve the same alignment equation. LTSA uses the pseudo inverse method, while HLLE uses QR decomposition method. Since these two differences are not essential, we claim that HLLE and LTSA are equivalent to each other.
2) iHLLE is an intermediate algorithm between HLLE and LTSA. In the neighborhood construction, iHLLE is exactly the same with LTSA, while in the alignment, iHLLE is exactly the same with HLLE. The differences between HLLE, iHLLE, and LTSA can be illustrated in Table I. It is clear that iHLLE is equivalent to HLLE and also equivalent to LTSA.
3) The purpose to introduce iHLLE is to further prove the equivalence between HLLE and LTSA. It has been long believed in manifold learning that the main difference between HLLE and LTSA lies in the alignment, not in the neighborhood construction. Compared with LTSA's alignment, HLLE's alignment seems much more complicated and different. However, the introduction of iHLLE can correct this misunderstanding. As the theorem proven in Section VII shows, the solution of iHLLE to the alignment equation can be exactly the same as that of LTSA. That is to say, if HLLE adopts the LTSAs method to construct neighborhoods of data points (at this time, HLLE becomes iHLLE), HLLE can be exactly the same with LTSA. On other words, the real difference between HLLE and LTSA lies in the neighborhood construction, not in the alignment. However, as recognized widely, the difference of whether to include a data point into its neighborhood is too trivial to distinguish HLLE and LTSA in essence from each other.
4) Although HLLE and LTSA are equivalent in essence, LTSA does better than HLLE from the viewpoint of data utilization: LTSA includes x_n into X_n^{LTSA}, while HLLE discards x_n from X_n^{HLLE}. In this sense, LTSA can be regarded as an improvement to HLLE. This may account for why LTSA performs better than HLLE in some applications.

APPENDIX
QUADRATIC FORM TRANSFORMATION

For all vectors $x \in R^d$ and symmetric matrices $H \in R^{d\times d}$

$$x^T Hx = \sum_{i=1}^{d}\sum_{j=1}^{d} h_{ij}x_i x_j = \sum_{i=1}^{d} h_{ii}x_i^2 + 2\sum_{i=1}^{d-1}\sum_{j=1}^{d} h_{ij}x_i x_j$$

$$= \begin{bmatrix} x_1^2 & \dots & x_d^2 \end{bmatrix} \begin{bmatrix} h_{11} \\ \vdots \\ h_{dd} \end{bmatrix} + \begin{bmatrix} \sqrt{2}x_1x_2 & \dots & \sqrt{2}x_{d-1}x_d \end{bmatrix} \begin{bmatrix} \sqrt{2}h_{12} \\ \vdots \\ \sqrt{2}h_{(d-1)d} \end{bmatrix}$$

$$= \begin{bmatrix} x_1^2 & \dots & x_d^2 & \sqrt{2}x_1x_2 & \dots & \sqrt{2}x_{d-1}x_d \end{bmatrix} \begin{bmatrix} h_{11} \\ \vdots \\ h_{dd} \\ \sqrt{2}h_{12} \\ \vdots \\ \sqrt{2}h_{(d-1)d} \end{bmatrix}.$$

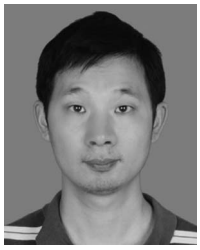
ACKNOWLEDGMENT

The authors would like to the anonymous reviewers for their careful work and thoughtful suggestions that have helped improve this paper substantially.

REFERENCES

[1] J. B. Tenenbaum, V. De Silva, and J. C. Langford, "A global geometric framework for nonlinear dimension reduction," *Science*, vol. 290, no. 5500, pp. 2319–2323, Dec. 2000.
[2] M. Balasubramanian, E. L. Schwartz, J. B. Tenenbaum, V. de Silva, and J. C. Langford, "The isomap algorithm and topological stability," *Science*, vol. 295, no. 5552, p. 7, 2002.
[3] S. T. Roweis and L. K. Saul, "Nonlinear dimensionality reduction by locally linear embedding," *Science*, vol. 290, no. 5500, pp. 2323–2326, 2000.
[4] L. K. Saul and S. T. Rowels, "Think globally, fit locally: Unsupervised learning of low dimensional manifolds," *J. Mach. Learn. Res.*, vol. 4, pp. 119–155, Jun. 2004.
[5] M. Sun, C. Liu, J. Yang, Z. Jin, and J. Yang, "A two-step framework for highly nonlinear data unfolding," *Neurocomputing*, vol. 73, nos. 10–12, pp. 1801–1807, 2010.
[6] C. Hou, J. Wang, Y. Wu, and D. Yi, "Local linear transformation embedding," *Neurocomputing*, vol. 72, nos. 10–12, pp. 2368–2378, 2009.

[7] X. Li, S. Lin, S. Yan, and D. Xu, "Discriminant locally linear embedding with high-order tensor data," *IEEE Trans. Syst., Man, Cybern. B, Cybern.*, vol. 38, no. 2, pp. 342–352, Apr. 2008.
[8] Y. Pan, S. S. Ge, and A. Al Mamun, "Weighted locally linear embedding for dimension reduction," *Pattern Recognit.*, vol. 42, no. 5, pp. 798–811, 2009.
[9] H. Chang and D.-Y. Yeung, "Robust locally linear embedding," *Pattern Recognit.*, vol. 39, no. 6, pp. 1053–1065, 2006.
[10] M. Belkin and P. Niyogi, "Laplacian eigenmaps for dimensionality reduction and Laplacian eigenmaps for dimensionality reduction and data representation," *Neural Comput.*, vol. 15, no. 6, pp. 1373–1396, 2003.
[11] D. Donoho and C. Grimes, "Hessian eigenmaps: New tools for nonlinear dimensionality reduction," *Proc. Nat. Acad. Sci.*, vol. 100, pp. 5591–5596, Mar. 2003.
[12] Z. Zhang and H. Zha, "Principal manifolds and nonlinear dimensionality reduction via tangent space alignment," *SIAM J. Sci. Comput.*, vol. 26, no. 1, pp. 313–338, 2005.
[13] K. Q. Weinberger and L. K. Saul, "Unsupervised learning of image manifolds by semidefinite programming," *Int. J. Comput. Vis.*, vol. 70, no. 1, pp. 77–90, 2006.
[14] S. Lafon and A. B. Lee, "Diffusion maps and coarse-graining: A unified framework for dimensionality reduction, graph partitioning, and data set parameterization," *IEEE Trans. Pattern Anal. Mach. Intell.*, vol. 28, no. 9, pp. 1393–1403, Sep. 2006.
[15] S. Lafon, Y. Keller, and R. R. Coifman, "Data fusion and multicue data matching by diffusion maps," *IEEE Trans. Pattern Anal. Mach. Intell.*, vol. 28, no. 11, pp. 1784–1797, Nov. 2006.
[16] A. O'Connell, "Modern multidimensional scaling: Theory and applications," *J. Amer. Stat. Assoc.*, vol. 94, no. 445, pp. 338–340, 1999.
[17] Z. Zhang, J. Wang, and H. Zha, "Adaptive manifold learning," *IEEE Trans. Pattern Anal. Mach. Intell.*, vol. 34, no. 2, pp. 253–265, Feb. 2012.
[18] C. Varini, A. Degenhard, and T. W. Nattkemper, "ISOLLE: LLE with geodesic distance," *Neurocomputing*, vol. 69, nos. 13–15, pp. 1768–1771, 2006.
[19] R. Karbauskaitė, O. Kurasova, and G. Dzemyda, "Selection of the number of neighbours of each data point for the locally linear embedding algorithm," *Inf. Technol. Control*, vol. 36, no. 4, pp. 359–364, 2007.
[20] J. Yin, D. Hu, and Z. Zhou, "Noisy manifold learning using neighborhood smoothing embedding," *Pattern Recognit. Lett.*, vol. 29, no. 11, pp. 1613–1620, 2008.
[21] D. Tarlow, K. Swersky, L. Charlin, I. Sutskever, and R. Zemel, "Stochastic *k*-neighborhood selection for supervised and unsupervised learning, international conference on machine learning," *Pattern Recognit.*, vol. 28, no. 3, pp. 199–207, 2013.
[22] Y. Zhan, J. Yin, and J. Long, "Dynamic neighborhood selection for nonlinear dimensionality reduction," in *Proc. Model. Decis. Artif. Intell. (MDAI)*, vol. 5861. 2009, pp. 327–337.
[23] X. Gao and J. Liang, "The dynamical neighborhood selection based on the sampling density and manifold curvature for isometric data embedding," *Pattern Recognit. Lett.*, vol. 32, no. 2, pp. 202–209, 2011.
[24] V. Premachandran and R. Kakarala, "Consensus of k-NNs for robust neighborhood selection on graph-based manifolds," in *Proc. IEEE Conf. Comput. Vis. Pattern Recognit. (CVPR)*, Portland, OR, USA, 2013, pp. 1594–1601.
[25] L. Liang, F. Liu, M. Li, and G. Xu, "Manifold learning with self-organizing mapping for feature extraction of nonlinear faults in rotating machinery," *Math. Problems Eng.*, vol. 2015, no. 20, pp. 1–11, 2015.
[26] T. Lin and H. Zha, "Riemannian manifold learning," *IEEE Trans. Pattern Anal. Mach. Intell.*, vol. 30, no. 5, pp. 796–809, May 2008.
[27] S. Karygianni and P. Frossard, "Tangent-based manifold approximation with locally linear models," *Signal Process.*, vol. 104, pp. 232–247, Nov. 2014.
[28] T. Zhang, J. Yang, D. Zhao, and X. Ge, "Linear local tangent space alignment and application to face recognition," *Neurocomputing*, vol. 70, nos. 7–9, pp. 1547–1553, 2007.
[29] P. Dollár, V. Rabaud, and S. Belongie, "Non-isometric manifold learning: Analysis and an algorithm," in *Proc. Int. Conf. Mach. Learn. (ICML)*, Corvallis, OR, USA, 2007, pp. 241–248.
[30] S. Xiang, F. Nie, C. Zhang, and C. Zhang, "Nonlinear dimensionality reduction with local spline embedding," *IEEE Trans. Knowl. Data Eng.*, vol. 21, no. 9, pp. 1285–1298, Sep. 2009.
[31] H. Xiaofei and L. Binbin, "Tangent space learning and generalization," *Front. Elect. Electron. Eng. China*, vol. 6, no. 1, pp. 27–42, 2011.
[32] Q. Ye, H. Zha, and R.-C. Li, "Analysis of an alignment algorithm for nonlinear dimensionality reduction," *BIT Numer. Math.*, vol. 47, no. 4, pp. 873–885, 2007.
[33] C. Wang and S. Mahadevan, "Manifold alignment using procrustes analysis," in *Proc. Int. Conf. Mach. Learn. (ICML)*, Helsinki, Finland, 2008, pp. 1120–1127.
[34] T. Zhang, X. Li, D. Tao, and J. Yang, "Local coordinates alignment (LCA): A novel manifold learning approach," *Int. J. Pattern Recognit. Artif. Intell.*, vol. 22, no. 4, pp. 667–690, 2011.
[35] T. Zhang, D. Tao, X. Li, and J. Yang, "Patch alignment for dimensionality reduction," *IEEE Trans. Knowl. Data Eng.*, vol. 21, no. 9, pp. 1299–1313, Sep. 2009.
[36] P. Zhang, H. Qiao, and B. Zhang, "An improved local tangent space alignment method for manifold learning," *Pattern Recognit. Lett.*, vol. 32, no. 2, pp. 181–189, 2011.
[37] Z. Han, D.-Y. Meng, Z.-B. Xu, and N.-N. Gu, "Incremental alignment manifold learning," *J. Comput. Sci. Technol.*, vol. 26, no. 1, pp. 153–165, 2011.
[38] Y. Chen, J. Yin, J. Zhu, and Z. Jin, "Dimensionality reduction via locally reconstructive patch alignment," *Opt. Eng.*, vol. 51, no. 7, pp. 397–407, 2012.
[39] J. Chen, Z. Ma, and Y. Liu, "Local coordinates alignment with global preservation for dimensionality reduction," *IEEE Trans. Neural Netw. Learn. Syst.*, vol. 24, no. 1, pp. 106–117, Jan. 2013.
[40] Z. Ma and J. Chen, "The Huffman-like alignment in manifold learning," *Int. J. Pattern Recognit. Artif. Intell.*, vol. 28, no. 4, pp. 985–1008, 2014.
[41] S. Xiang, F. Nie, C. Pan, and C. Zhang, "Regression reformulations of LLE and LTSA with locally linear transformation," *IEEE Trans. Syst., Man, Cybern. B, Cybern.*, vol. 41, no. 5, pp. 1250–1262, Oct. 2011.
[42] Y. Zhou and S. Sun, "Manifold partition discriminant analysis," *IEEE Trans. Cybern.*, vol. PP, no. 99, pp. 1–11, Mar. 2016.
[43] Y. Tang, "Deep learning using linear support vector machines," in *Proc. Int. Conf. Mach. Learn. (ICML)*, Atlanta, GA, USA, 2013.
[44] W. Wang, R. Arora, K. Livescu, and J. Bilmes, "On deep multi-view representation learning," in *Proc. 32nd Int. Conf. Mach. Learn.*, Lille, France, 2015, pp. 1083–1092.
[45] T.-H. Chan *et al.*, "PCANet: A simple deep learning baseline for image classification," *IEEE Trans. Image Process.*, vol. 24, no. 12, pp. 5017–5032, Dec. 2015.



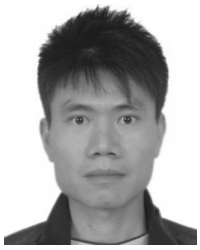
Sumin Zhang received the B.Sc. and M.Sc. degrees in computer science and technology from the Wuhan University of Technology, Wuhan, China, in 2001 and 2004, respectively, and the Ph.D. degree in communication and information system from Sun Yat-sen University, Guangzhou, China, in 2016.

He joined South China Agricultural University, Guangzhou, in 2004, where he is currently a Lecturer with the School of Mathematics and Informatics. His current research interests include machine learning, dimensionality reduction, and pattern recognition.



Zhengming Ma received the B.Sc. and M.Sc. degrees from the South China University of Technology, Guangzhou, China, in 1982 and 1985, respectively, and the Ph.D. degree in pattern recognition and intelligent control from Tsinghua University, Beijing, China, in 1989.

He is currently a Professor with the School of Electronics and Information Technology, Sun Yat-sen University, Guangzhou. His current research interests include machine learning and signal processing.



Hengliang Tan received the B.Sc. degree from Foshan University, Foshan, China, in 2006, and the M.Sc. and Ph.D. degrees from Sun Yat-sen University, Guangzhou, China, in 2011 and 2016, respectively.

He joined the School of Computer Science and Educational Software, Guangzhou University, Guangzhou, in 2016. His current research interests include machine learning and pattern recognition.

View publication stats

Computers and Electronics in Agriculture 236 (2025) 110412

Contents lists available at ScienceDirect

Computers and Electronics in Agriculture

journal homepage: www.elsevier.com/locate/compag

Original papers

Pig body weight prediction based on weight waveform graph

Sumin Zhang [a,c], Jinfa Peng [a], Qiong Huang [a], Zhikun Li [a], Ling Yin [a,b,c,*]

[a] College of Mathematics and Informatics, South China Agricultural University, Guangzhou 510642, China
[b] National Engineering Research Center for Swine Breeding Industry, Guangzhou 510642, China
[c] State Key Laboratory of Swine and Poultry Breeding Industry, Guangzhou, Guangdong 510640, China

ARTICLE INFO

Keywords:
Gait
ResNet18SV
Regression equation
Dynamic weighing

ABSTRACT

Livestock body weight and its changes are important indicators for evalua ting the growth, nutritional status, and health condition of livestock. The normal walking gait of livestock is a visual basis for assessing their health. Since the body weight waveform data generated by livestock freely walking on weighing platforms simultaneously records information on livestock body weight and walking gait characteristics, this study proposes to achieve dynamic weighing of pigs based on the pig weight waveform dataset. The paper first proposed an improved ResNet18 classification network model called ResNet18SV. Then, the ResNet18SV model is used for livestock gait classification, categorizing livestock gaits into four categories: fast, slow, normal, and linger based on their walking characteristics. Finally, a body weight regression model was tailored for each type of gait to accurately predict livestock weight. To validate the effectiveness and advancement of the proposed method, various classification models are used for gait classification comparative experiments, with the experimental results showing that the gait classification accuracy based on the ResNet18SV network is 97.13 %. Furthermore, based on the gait classification results, the pig body weight is predicted synchronously, with an overall average error of 0.28 %, close to the average error of static weighing (0.2 %). The experimental results demonstrate the good performance of our proposed method in livestock gait classification and dynamic weight prediction. By solely relying on inexpensive weighing platforms to obtain body weight waveform data, gait classification and weight prediction are achieved, thus offering a broader application value.

1. Introduction

At various stages of livestock production, such as weaning, conservation, selection, and fattening, as well as in daily health monitoring, it is necessary to measure the weight of livestock and track their gait for monitoring. Based on the measurements taken at different periods, the individual growth, nutritional level, and health status of livestock can be distinguished, and their grades can be assessed and differentiated accordingly. This information can be used to develop different feeding programs and breeding standards for livestock of different grades, thereby improving livestock production levels. Traditionally, livestock weighing has been carried out manually by experienced ranch staff using scales, which is not only time-consuming and labor-intensive but also can cause stress to the animals, leading to errors and potential risks (kicking, stepping on, or biting). Particularly in large-scale farming operations, manual weighing of a large number of livestock is difficult to accomplish.

In recent years, (Yuqing et al., 2021; Jia et al., 2021; Haikun et al., 2022; Fernandes et al., 2020) has successfully promoted the refinement, automation, and intelligence of the livestock farming industry through the use of computer vision technology. With the continuous development of computer vision and Internet of Things technologies, systems for automatic weight measurement have been implemented, including weighing systems for daily health and nutrition monitoring (Segerkvist et al., 2020; González-García et al., 2018; Dickinson et al., 2013; Podlahová et al., 2011) and weighing systems for disease monitoring and early warning based on abnormal growth curves (Alawneh et al., 2011; Pastell et al., 2006). Significant research progress has also been made in the visual estimation of livestock body weight and dynamic weighing. (Cang et al., 2019) designed a neural network based on Faster R-CNN with additional regression branches, using depth images of 20 pigs from a top view for weight estimation. The method achieved an average relative error of 0.37 %. While it can accurately estimate individual pig weights, it is weak at estimating group weights. (Hengxiang et al., 2021) proposed a dual-branch BotNet network with multiple parallel fully connected layers for pig weight estimation, with an

* Corresponding author at: College of Mathematics and Informatics, South China Agricultural University, Guangzhou 510642, China.
E-mail address: yin_ling@scau.edu.cn (L. Yin).

https://doi.org/10.1016/j.compag.2025.110412
Received 21 March 2024; Received in revised form 25 March 2025; Accepted 13 April 2025
Available online 1 May 2025
0168-1699/© 2025 Elsevier B.V. All rights are reserved, including those for text and data mining, AI training, and similar technologies.

average absolute error of 6.366 kg. (Wei et al., 2023) introduced a dual-stream cross-attention Visual Transformer method using 15,466 RGB and depth images to obtain the average shoulder height, body length, and back projection area of pigs. These parameters are then used in a secondary regression to estimate pig weight, with an average absolute error of 3.237 kg. This method is limited to cases where livestock are in a standing or standard posture and does not consider various postures. (Kwon et al., 2023) proposed using grid reconstruction to generate training data from point clouds of pigs and developing a DNN for estimating live pig weight with an average absolute error of 4.89 kg. This method demonstrates strong robustness and high accuracy in weight estimation. (Guixin et al., 2022) suggested using body size parameters obtained from the point cloud of the livestock's back to establish a regression analysis model for predicting livestock weight with an average absolute error of 2.961 kg. This research can obtain reliable regression parameters from different regression models and accurately estimate livestock weight.

In the field of dynamic livestock weighing, researchers have explored various approaches to accurately determine weight while animals are in motion. These methods can be broadly categorized into traditional statistical filtering techniques, physics-based models, AI-driven algorithms, and multi-source data fusion techniques. Traditional statistical methods, such as direct averaging of weight readings (U M Peiper et al., 1993), are straightforward but fail to account for irregular movements like pausing, linger, or rapid motion, leading to significant deviations. Similarly, physics-based models, such as treating livestock walking as a pendulum motion (Cveticanin and Wendl, 2004), have demonstrated single-head weighing accuracy of 98 %. However, these methods often rely on overly idealized conditions, resulting in errors as high as 2 % and limiting their practical application in large-scale monitoring scenarios. AI-driven approaches have shown promise in improving accuracy and robustness. Automated walk-over weighing (WoW) systems (González-García et al., 2021) have achieved over 95 % consistency in repeatability and accuracy by detecting subtle weight fluctuations. However, these systems remain vulnerable to outliers caused by abnormal animal behaviors, requiring extensive data filtering. Similarly, AI-based poultry monitoring platforms (Schomburg et al., 2023) have demonstrated strong correlation with manual measurements (Spearman coefficient of 0.9868), yet sensor fluctuations induced by collective activity resulted in relative errors up to 11 % and potential mistake under heat stress or disease conditions. The proposed error compensation mechanism can improve the reliability of dynamic weighing systems. Mobile weighing systems (Hasan et al., 2024) have shown high correlation with traditional static weighing (Lin's concordance coefficient 0.97, $P < 0.001$), but systematic biases persist, particularly with weight-dependent deviations. Machine learning models integrating multi-source data, such as visual and flow sensor data (Cassimiro et al., 2024), have improved prediction accuracy. However, these models remain sensitive to extreme fluctuations, with R^2 values dropping to 0.71 under unstable conditions. Further advancements in signal processing have also contributed to improved accuracy. SVM-based classification techniques (Ningning et al., 2020) have been used to analyze dynamic weight waveform charts, followed by a combination of empirical wavelet transforms to achieve an average relative error below 1 %. Despite its accuracy, efficiency concerns and livestock-specific variations limit its broader application. To address these limitations, waveform signal analysis has been further refined (Zhijiang et al., 2023), incorporating time-domain feature extraction and error compensation. This method has achieved an average relative error of 0.68 % but struggles with scalability across different livestock types and movement patterns.

Livestock weight visual estimation and dynamic weighing each have their own application scenarios. The former involves non-contact weight estimation, which can effectively reduce livestock stress responses. It is suitable for monitoring long-term growth trends and periodic growth conditions of livestock. However, compared to the latter, the weight estimation error is relatively large. Dynamic weighing for livestock weight prediction results in smaller weight estimation errors and is suitable for scenarios involving minor growth changes in livestock over the short term.

By placing weighing platforms along the walking path of pigs and collecting dynamic weight signals of pigs, the ResNet18SV model is used to classify the weight signals and determine the gait categories of the pigs. Subsequently, a tailored weight regression equation was developed for each gait category to obtain the predicted weight. This method can reliably and stably obtain pig weight results in various complex situations, improving the accuracy of pig weight determination while avoiding the stress responses of pigs and potential livestock attacks associated with manual contact. It is highly suitable for promoting use on large-scale livestock farms. Particularly in special circumstances such as repeated movements and rapid passes by pigs, this method can accurately predict pig weight.

The main contributions of this paper can be summarized as follows:

- ·We categorize pig gait behavior into fast, slow, normal, and linger gaits.
- ·We propose the ResNet18SV model to improve the classification of pig gait.
- ·We tailored a body weight regression equation for each type of gait to improve prediction of pig body weight dynamics.

The remain of the paper is organized as follows. Section 2 describes the research methods, including data collection, data preprocessing, gait classification model and weight prediction strategy. Section 3 presents the main evaluation metrics and the results and analysis of the proposed classification model and weight prediction strategy. Section 4 discusses the rationality of the methods based on our analysis of the experiments conducted. Section 5 summarizes and discusses the experimental methods, experimental results and future research directions of this paper.

2. Materials and methods

This section introduces the construction of our weighing platform and the collection of datasets, followed by a detailed description of our weight prediction method.

2.1. Setting up the weighing platform

To ensure that all parts of the pig's body are fully on the weighing platform during weight measurement, a weight determination channel with fences on both sides was designed. Due to the uncontrollable nature of pigs, the experimental environment allows only one pig to pass through at a time, thus avoiding mutual interference during the measurement process.

Fig. 1 shows the on-site diagram of the system used at the pig farm. From the on-site diagram, it can be seen that the weight determination



Fig. 1. Site diagram of the pig weight dynamic weighing platform.

platform adopts a rectangular, flat structure with standardized lengths and widths. The standardized length of the livestock weighing platform is 2 m, with a width of approximately 0.5 m. In order to further clarify the system workflow and the process of each sensor obtaining weight and body size data, Fig. 2 provides the logical structure of the acquisition system. The acquisition system mainly consists of four parts: ear tag reading antenna, weighing platform, weighing display instrument, and data processing and storage computer. The RFID ear tag reading antenna is connected to the computer via a serial port; the weighing platform is connected to the weighing display to show real-time weight readings; and it is connected to the computer via a serial port. On the computer side, two USB to 485 serial ports are used to receive ear tag and weight data. After processing the weight data, the ear tag and weight data are automatically recorded and stored.

In Fig. 2, symbols ① to ⑥ represent: ① weighing platform, ② fence, ③ RFID reading antenna, ④ weighbridge data display, ⑤ data processing and storage computer, ⑥ USB to 485 serial port cable.

2.2. Dateset

The data collection work for this study was conducted between June 2023 and August 2023 at Guangdong Wen's Food Co., Ltd. and Jingjing Food Company in Heyuan City, Guangdong Province. After manual weighing, the pig enters the weight measurement channel. When non-zero data appears on the gravity sensor, the system starts to collect weight data. Then, when the pig passes through the middle of the channel and approaches the ear tag reading device, the reading of the ear tag number is automatically triggered. Next, the system continuously receives weight data until the pig walks off the weighing platform. When the weight data returns to zero again, the collection of this weight data is completed. Finally, all the instantaneous weight data of the ear tag and the pig during the period when it passes through the measurement channel are obtained. All instantaneous weight data during the period of passing through the weighbridge, with time as the x-axis and instantaneous weight data as the y-axis to plot the dynamic weight waveforms graph, as shown in Fig. 4. Each pig walks through two to three times. The target pig breed was Landrace pigs, with a weight range between 75 kg and 150 kg. There were 531 target pigs, and a total of 1443 sets of weight data were collected. After excluding invalid data caused by short-term contact leading to the weighbridge reading before resetting or when the pigs were not all standing on the weighing platform simultaneously, 1268 sets of weight data were obtained. The distribution of pig weights is shown in Fig. 3. In the experiments, the training set and test set were divided in the ratio of 7:3.

When pigs walk normally through the measuring channel or exhibit special behaviors such as backing up, stopping, or moving rapidly, significant differences in the process and details lead to weight data sequences forming waveform data with various characteristics. Fig. 4 illustrates the waveform features of pigs passing through the weighing platform in various scenarios. It can be observed that the weight waveform for the fast category has shorter peak segments and overall shorter duration, while the slow category exhibits longer duration of peak segments with smoother peak values. The normal category falls between the fast and slow categories in terms of peak segment duration but also shows relatively smooth peak values. The linger category displays significant fluctuations in peak segments with irregular patterns. It is also observed that there are significant speed differences between fast, slow and normal gaits, and therefore it is possible to distinguish between these three gaits on the basis of speed. During the passage of the pig through the weighbridge, it was stipulated that up to one weight difference between the peak and the trough greater than 40 % of the pig's true body weight and the duration of the pig's four feet on the weighbridge less than 3 s was considered as fast, from 3 to 6 s was considered as normal, and 6 and more seconds was considered as slow. However, in the linger gait, although there is a mixture of fast and slow speeds, weight fluctuations are more irregular and greater in magnitude than in the other three gaits, usually displaying two or more peaks and troughs, with large differences between peaks and troughs. Thus, the number of peaks and troughs and the difference in body weight between them can be used to differentiate between fast, slow and normal gait and wandering gait.

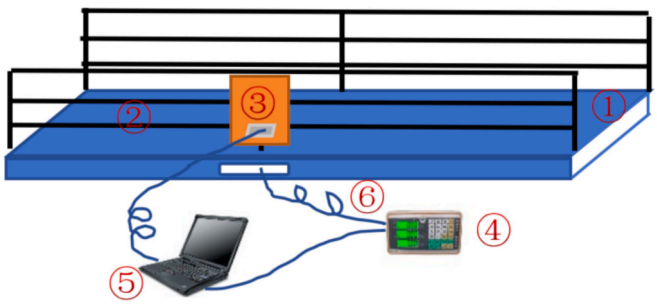


Fig. 2. Weight automatic collection system.

2.3. Method

Fig. 5 illustrates the overall framework of the training and prediction process of the model in this study. The left side represents the model training process, which consists of two components: training the classification model and the weight equation. In the training phase, dynamic weight sequence data are first collected and labeled with gait categories, then converted into waveform diagrams. ResNet18SV is used to classify the gait waveform diagrams, resulting in the classification model. Meanwhile, peak segments are extracted from the dynamic weight sequence, and multiple parameters w are obtained. A regression equation is then used to tailor an optimal weight equation for each gait category, resulting in different gait-specific weight equations W_{type}. In the prediction phase, dynamic weight sequence data are first acquired and converted into waveform diagrams. The trained classification model is then used to classify the Waveform Graph, determining the corresponding gait category *type*. After classification, multiple key parameters w are extracted from the dynamic weight sequence. Finally, multiple parameters w and the corresponding weight equation W_{type} for the determined gait category are used to predict the weight, resulting in the predicted weight value. The structure of the classification model is described in Section 2.3.1, including the ResNet18 primitive network, the SE attention mechanism, the VIT classifier, and the overall framework structure of ResNet18SV; and the weight prediction strategy is described in Section 2.3.2, including the acquisition of the raw data, the peak segmentation, the fitting of the weight equation, and the weight prediction.

2.3.1. Classification model

2.3.1.1. ResNet18. ResNet18 was proposed by (Kaiming et al., 2015) and is commonly used for image classification and recognition tasks. Its core algorithm is residual learning, where adding residual blocks to the neural network can address the issues of vanishing gradients and exploding gradients in deep neural networks. A residual block contains a skip connection, allowing information to flow directly across multiple layers, enabling the network to better capture details and features in images, and the model is relatively lightweight. The specific implementation of feature extraction is given in formulas (1) and (2).

$$x_l = F_l(x_{l-1}) + x_{l-1} \tag{1}$$

$$X_{res} = F_l(x_{l-1}) = Sig(\boldsymbol{W}_{l,n} \cdots Sig(\boldsymbol{W}_{l,2} Sig(\boldsymbol{W}_{l,1} x_{l-1}))) \tag{2}$$

where x_l is the feature map data of the lth layer processed through the previous $l-1$ layer, F_l is the result obtained after x_l undergoes a series of

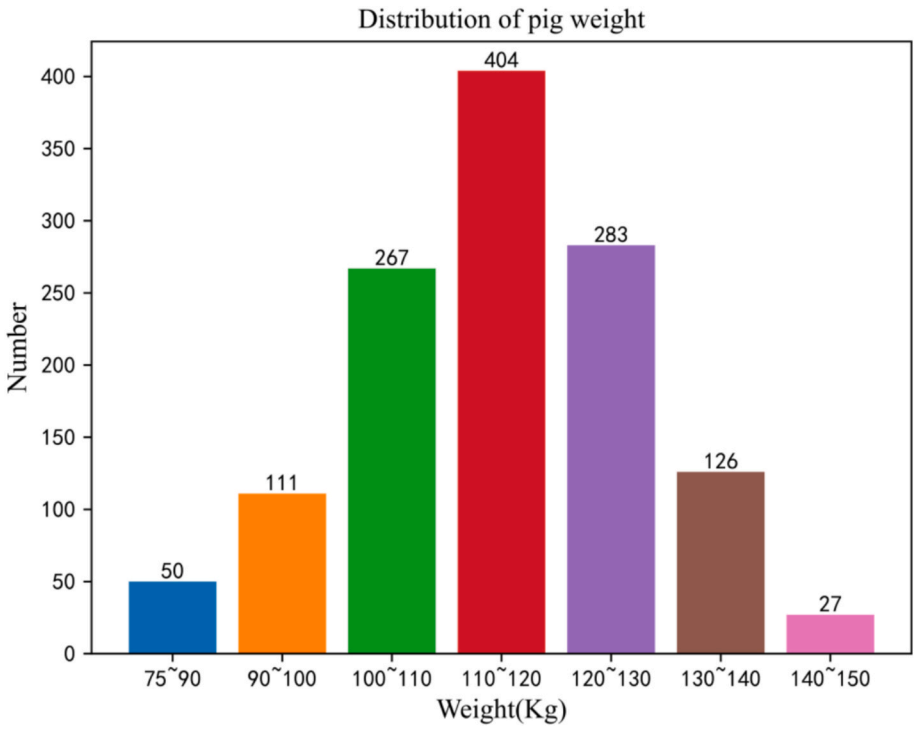


Fig. 3. Weight Distribution Chart of Pigs.

operations such as convolution and activation, W refers to the network weights of each layer and $Sig()$ represents the *Sigmoid* function.

2.3.1.2. SE attention mechanism. SE-Net is an attention mechanism for deep convolutional neural networks that aims to improve the performance of the network on tasks such as image classification (as shown in Fig. 6). SE-Net was originally proposed by (Jie et al., 2017), which introduced the Squeeze-and-Excitation (SE) module to adaptively adjust the weights of channel features by learning the weights of each channel, thereby increasing the weights of valid channels and decreasing the weights of invalid or less effective channels. The attention mechanism focuses on certain important areas or features, thereby improving processing efficiency and accuracy. For example, in lung infection severity prediction, the SE mechanism enhances the focus on lung lobes and infection areas (Yousefzadeh et al., 2022); in pneumonia detection, the dynamic mapping attention mechanism optimizes the capture of image details (Labbaf Khaniki et al., 2023); AR and VR technologies help learners focus on key details through immersive learning experiences (Bigonah et al., 2024; Yousefi et al., 2022); and in myocardial fibrosis analysis, the self-calibration method guides attention to specific regions (Mehrnia et al., 2024). These all help us quickly locate key areas or features, enabling us to solve problems more efficiently and accurately.

The SE module of the SE-Net consists of three steps: channel-wise feature squeeze, channel-wise feature excitation, and channel-wise feature recalibration. In the squeeze step, the SE module compresses the feature maps of each channel into a single value through global average pooling to obtain a global feature representation for the channel. In the excitation step, the SE module uses two fully connected layers to learn the weights for each channel, which are then applied to the original feature maps to adjust the weights of the channel feature maps. Finally, the weighted channel feature maps are added back to the original feature maps to recalibrate the original features, allowing the computer to learn the areas of focus in each image during neural network training, forming an attention mechanism (Choi et al., 2018). The specific implementation of feature extraction is given in formulas (3)–(5).

$$z_c = \boldsymbol{F}_{sq}(\boldsymbol{u}_c) = \frac{1}{H \times W}\sum_{i=1}^{H}\sum_{j=1}^{W} u_c(i,j), u_c(i,j) \in X_{res} \tag{3}$$

$$s_c = \boldsymbol{F}_{ex}(\boldsymbol{z}, \boldsymbol{W}) = Sig(\boldsymbol{W}_2 \mathrm{R}(\boldsymbol{W}_1 \boldsymbol{z})) \tag{4}$$

$$X_{se} = \boldsymbol{F}_{scale}(\boldsymbol{u}_c, s_c) = \boldsymbol{u}_c s_c \tag{5}$$

where F_{sq} is the squeeze operation applied to the feature output of ResNet18, and H, W, and C represent the height, width, and number of channels of X_{res}; $\boldsymbol{F}_{ex}$ represents the excitation operation, which involves a series of convolutions and nonlinear operations; and $\boldsymbol{F}_{scale}$ is the multiplication of the original features with $\boldsymbol{F}_{ex}$, resulting in the processed feature map X_{se}.

2.3.1.3. VIT classifier. The Vision Transformer (ViT) is an image classification model based on a self-attention mechanism (A Dosovitskiy et al., 2020). It divides the image into a series of image patches and utilizes a transformer model for feature extraction and classification of these patches. VIT Classifier consists of an input layer, two hidden layers, and an output layer, commonly known as the MLP Head (as shown in Fig. 7). The hidden layers incorporate a tanh activation function to further extract features of the weight waveform, resulting in better classification performance than the ResNet18 classifier. The specific implementation of feature extraction is given in formulas (6)–(8).

$$h_1 = tanh(\boldsymbol{W}_1 z + b_1) \tag{6}$$

$$h_l = tanh(\boldsymbol{W}_l h_{l-1} + b_l) \tag{7}$$

$$y_{pred,i} = \frac{e^{(\boldsymbol{W}_L h_{L-1} + b_L)_i}}{\sum_{j=1}^{C} e^{(\boldsymbol{W}_L h_{L-1} + b_L)_j}}, i = 1, 2, \cdots, C \tag{8}$$

where z represents the feature vector obtained after performing average pooling on X_{se}; $tanh$ is an activation function that performs nonlinear transformations to enhance the network's expressive power; $y_{pred,i}$ represents the output converted into a class probability distribution through

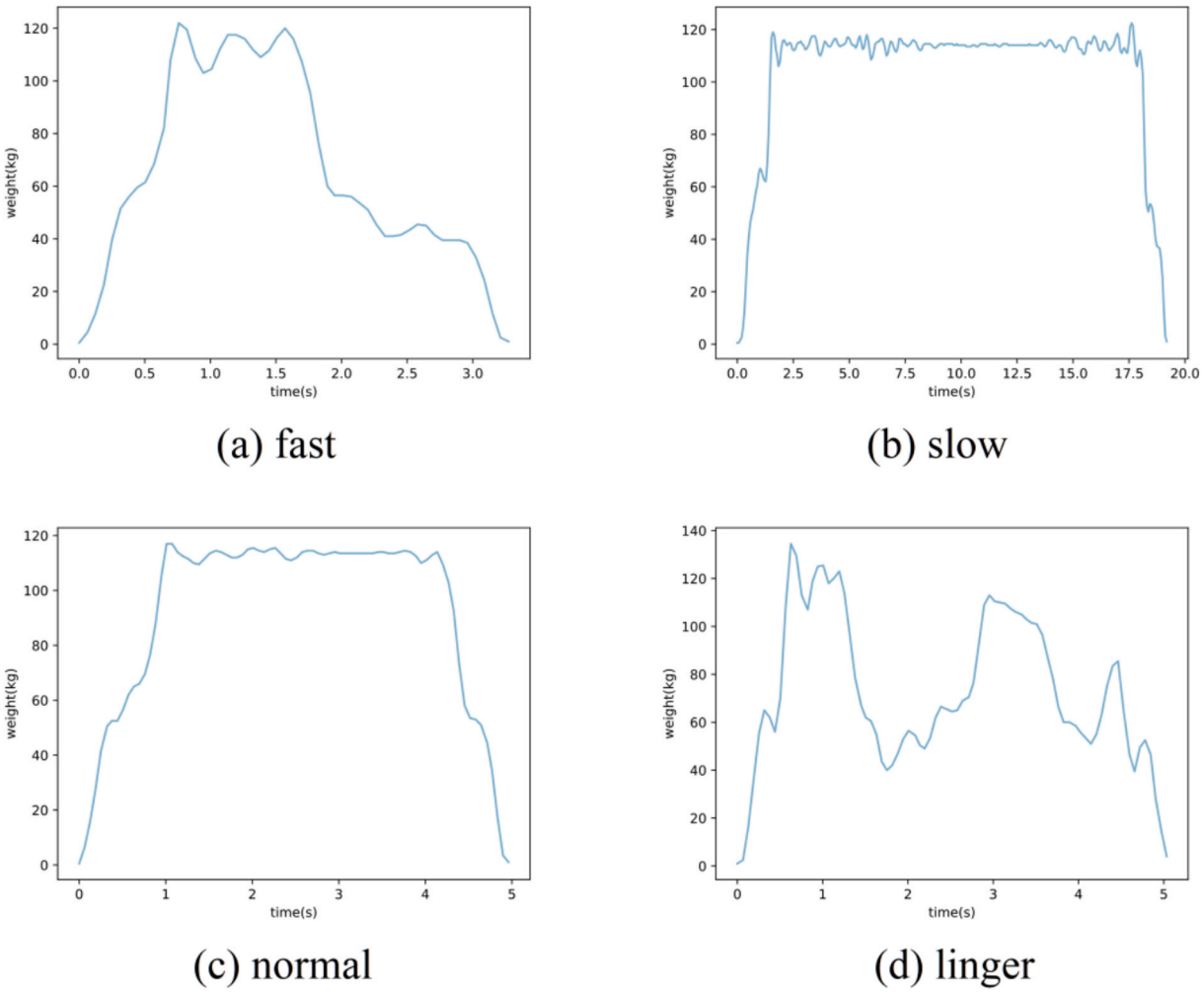


Fig. 4. Waveform characteristics of pigs passing through the weighbridge in different gaits: (a) fast passage; (b) slow and steady movement; (c) normal passage; (d) lingering passage.

the softmax function, and C denotes the number of classes.

2.3.1.4. ResNet18SV. There are multiple strategies for adding the SE attention mechanism, each of which may lead to some variability in the extracted features and thus produce different results. The embedding position of the attention mechanism has a certain effect on the recognition accuracy, but adding the attention mechanism to the first convolutional layer or the last convolutional layer will not change the original structure of the ResNet18 network and can still effectively migrate the original pre-training parameters (Dongmei et al., 2022). So in this experiment, the SE attention mechanism is added to the end of the residual structure of ResNet18, and the classifier (MLP Head layer) from the Vision Transformer model is used to replace the classifier of the ResNet18 model, constituting the ResNet18SV model(shown in Fig. 8).

2.3.1.5. Classification experiment processing flow. The main workflow of the classification experiment is summarized in Fig. 9. This classification experiment work is divided into four parts: collecting data, processing data, feature extraction network, and output. The details of this workflow are described as follows.

In the data preprocessing part, it mainly includes three stages: data transformation, data filtering, and data marking.

Data Transformation: Converting the collected dynamic weight data into weight waveform graphs is a necessary operation before classification and facilitates subsequent experimental operations.

Data Filtering: Before model training, it is necessary to exclude abnormal and non-standard data, such as abnormal data caused by weight table data not returning to zero, insufficient weight data caused by livestock running too fast on the weighing scale, and data that does not meet the standard due to livestock having only two feet on the weighing scale.

Data Labeling: Each filtered image is manually classified and labeled with categories.

2.3.2. Weight prediction strategy

The accuracy of weight prediction results depends on the accuracy of gait classification. Obviously, the weight measured when all four feet of the pig are on the weighing platform is the true weight of the pig. Only by accurately obtaining the weight data in the interval where the weight waveform peaks are located for statistics can the weight of the pig be accurately predicted. Therefore, in order to ensure that the true weight of the pig is obtained as accurately as possible when the pig passes through the weighing scale in various situations, gait weight data from pigs were statistically analyzed and one weight regression equation was tailored for each gait category in this study. The data flow is shown in Fig. 10.

2.3.2.1. Obtain the original dataset and actual weights. In section 2.2, the gait weight data of pigs were collected using sensors in the experiment, i.e., the original dataset $W_1=(w_1, w_2, w_3, \ldots w_n)$, and obtained the static actual weight y of the pigs using a cage scale.

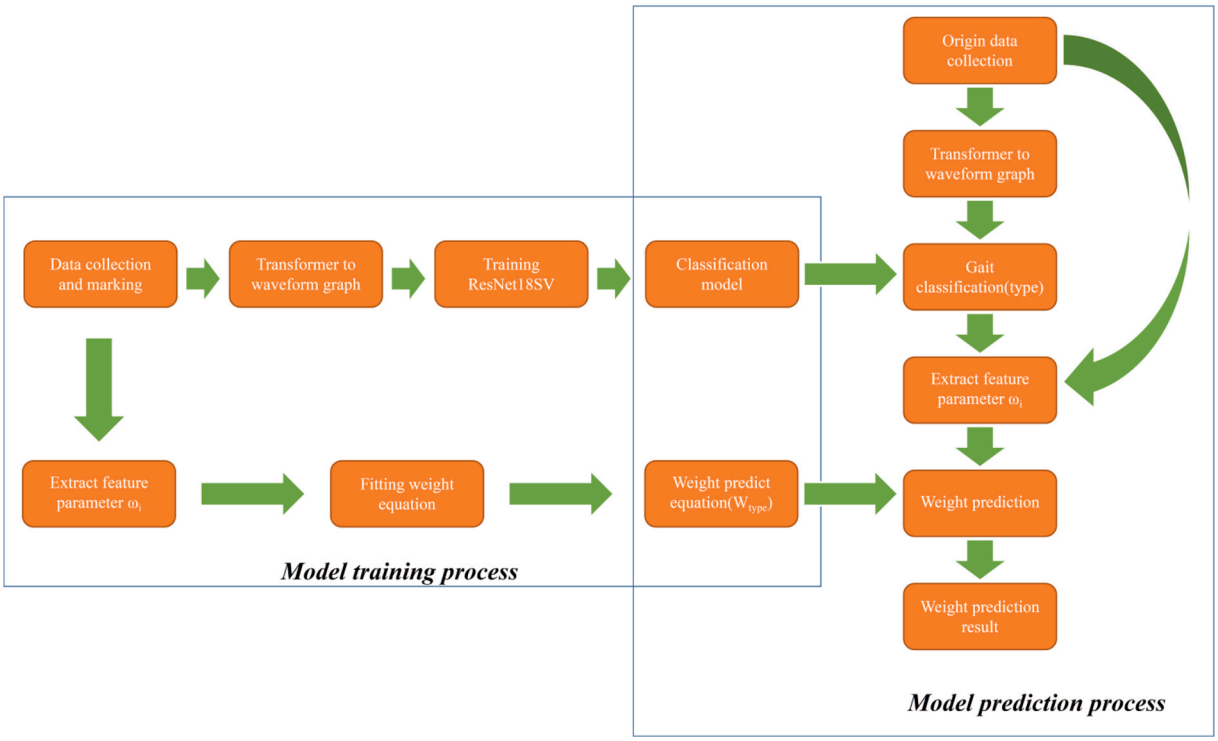


Fig. 5. Overall flowchart of weight prediction.

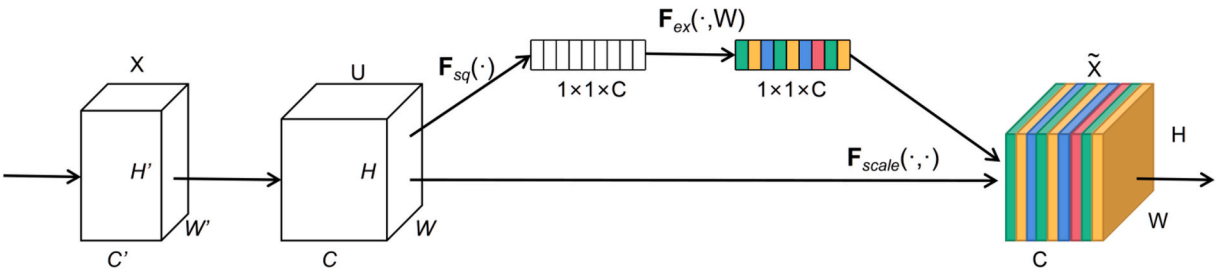


Fig. 6. SE-Net Attention Mechanism Structure.

2.3.2.2. Peak segmentation. In this study, the key to achieving a good prediction result lies in how to obtain representative key weight values from numerous dynamic weight data to fit the weight equation. Directly extracting the top peak segment is the most straightforward solution because the data from the top peak segment is often closely related to the true weight values. However, the challenge lies in selecting the threshold value that aligns with the weight data distribution of the majority of a particular category. Therefore, based on statistical analysis, this study proposes a strategy of extracting the optimal coefficients with the minimum error using two-stage extraction based on adaptive thresholds to obtain more representative data, i.e., certain parameters that are closely related to the real weight. The quadratic peak segmentation process consists of four steps.

From Fig. 11, it can be seen that the numerical fluctuations in the original dataset W_1 are large, thus requiring the identification of the overall best threshold to partition the W_1 dataset. First, the maximum value (weight_max), all local maxima, and minima were obtained from the W_1 dataset, and then derive the first optimal selection coefficient α based on the minimum error adaptive threshold, resulting in the threshold α*weight_max for partitioning the W_1 dataset. Filtering the data in the W_1 set based on α*weight_max, extracting weight data greater than α*weight_max to obtain the weight set W_2. It is worth noting that extremum values are the local extremes in the dataset, and their means can better represent the critical points of the dataset. Therefore, by filtering out the local maxima and minima data greater than α*weight_max, their average values were calculated to obtain the mean maximum value (mean_maximum) and mean minimum value (mean_minimum), which are necessary prerequisites for determining the threshold to partition the W_2 dataset.

From the green curves in Fig. 11 (a)-(d), it is evident that the data distribution of the weight set W_2 at this point exhibits significant differences, necessitating the identification of a second boundary to partition the dataset. This ensures the selection of the most suitable data segment for weight prediction. By calculating the average of mean_maximum and mean_minimum, the mean_crest can be obtained. Finally, the experiment will automatically determine the overall best second selection coefficient β and use β*mean_crest as the threshold to partition the W_2 dataset.

Using β*mean_crest as the dividing line to filter the data in the weight set W_2, simultaneously extracting the data with weights less than β*mean_crest to obtain the weight set W_3, as depicted by the red curves in Fig. 11 (a)-(d). Similarly, the sets of local maxima and minima weights are also filtered to exclude data with weights less than β*mean_crest. The red curves in Fig. 11 (a)-(d) show that the weight data extracted using this algorithm corresponds to the weight measured on the scale for all four-legged animals. The data obtained in the second iteration is more

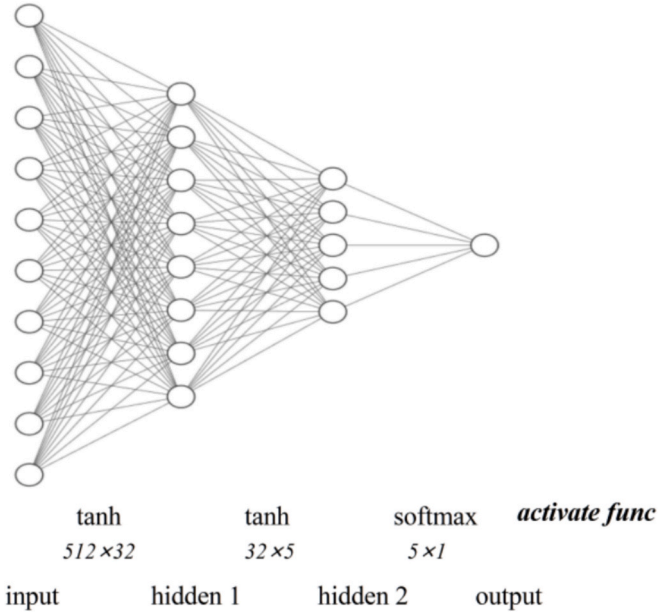


Fig. 7. VIT Classifier Network Structure.

detailed, precise, and closer to the true weight values compared to the first iteration. However, as observed in Fig. 11, the waveforms in the linger category exhibit many sharp peaks, indicating that some of the peak values obtained are higher than the true weight values. Therefore, adjustments need to be made to the local maxima values of this category by comparing them to the surrounding values and obtaining an adjustment coefficient γ. Multiplying the values by this coefficient ensures that the peak values exhibit a smoother trend.

2.3.2.3. Fitting the weight equation. Based on the W3 set, obtain feature parameters such as the maximum value (w_max), the mean value (w_mean), the mode (w_mode), the median (w_median), etc. Except for the slow category, other categories continuously train and learn using a multivariate regression model based on parameters such as w_max, w_mean, and w_mode to fit the weight regression equation W, as shown in formula (9).

$$W = p + a^{*}\omega_0 + b^{*}\omega_1 + c^{*}\omega_2 + d^{*}\omega_3 + e^{*}\omega_4 + f^{*}\omega_5 + g^{*}\omega_6\# \quad (9)$$

where ω_i (i = 0, 1…, 6) represents w_max, w_min, w_median, w_mode, mean_maximum, mean_minimum, and w_mean. For the slow category, the data obtained at this point are very close to the true values. Therefore, w_mean is used as the final weight prediction result, and the weight equation is given in formula (10).

$$W = \omega_6 \quad (10)$$

2.3.3. Weight prediction

The weight prediction process is shown in the right half of Fig. 5. After obtaining dynamic weight data of the pigs, they are inputted into the trained classification model to predict the gait category of the current pig. Then, peak values are extracted from the dynamic weight data, relevant feature parameters are obtained, and finally, these feature parameters are inputted into the weight equation W_{type} corresponding to the gait category to obtain the weight prediction result for the pig, completing one round of weight prediction.

3. Results and discussion

3.1. Evaluation metrics

Evaluation metrics are important tools used to assess the performance of machine learning models, helping us determine if a model is good enough and suitable for real-world applications. Common evaluation metrics for classification tasks include accuracy, precision, recall, F1 score, etc., while for regression prediction tasks, commonly used evaluation metrics include mean squared error and mean absolute error. The following evaluation metrics were used in this study to assess the model's performance and accuracy.

Accuracy refers to the proportion of correctly classified samples by the classifier to the total number of samples. It can reflect the degree of consistency between predicted values and true values. The formula for accuracy is given in Equation (11).

$$Accuracy = \frac{TP + TN}{TP + TN + FP + FN} \quad (11)$$

where TP (True Positive) is the number of true positive instances, TN (True Negative) is the number of true negative instances, FP (False Positive) is the number of false positive instances, and FN (False Negative) is the number of false negative instances. The symbols in the formulas for precision, recall, and other metrics also have this meaning.

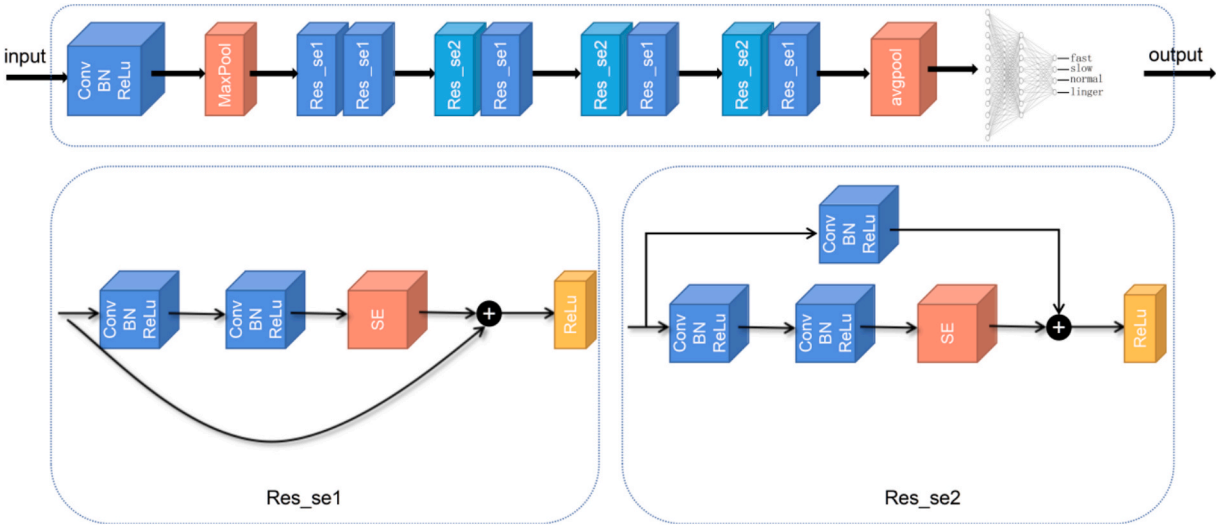


Fig. 8. ResNet18SV Model Structure.

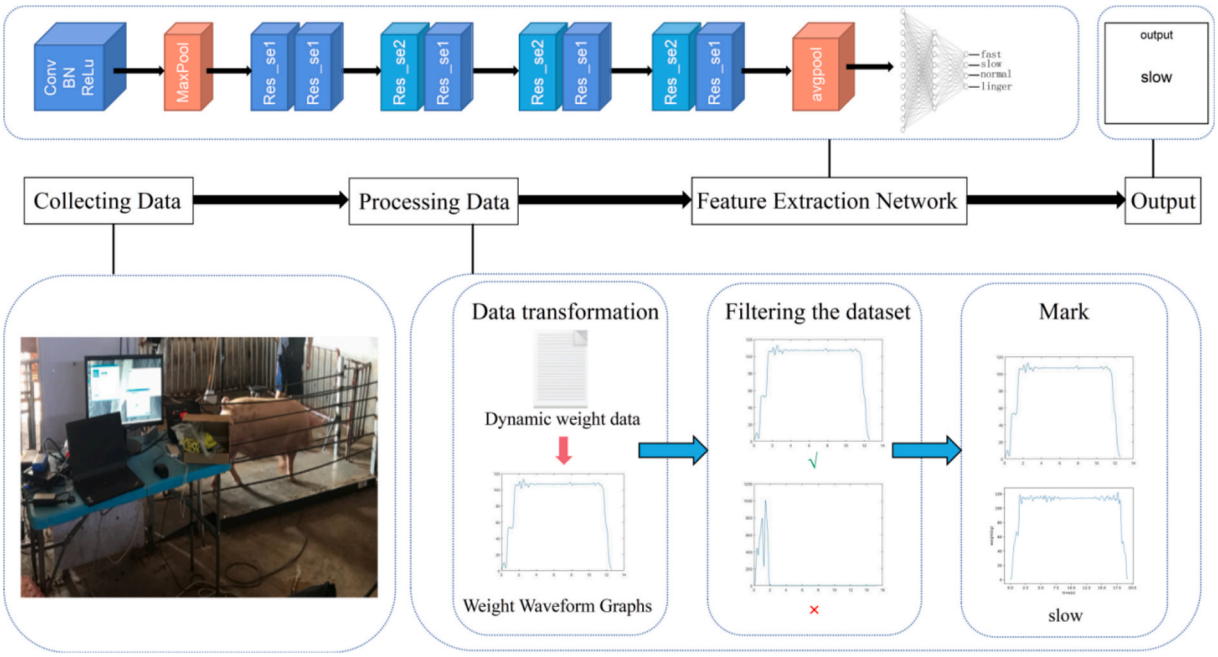


Fig. 9. Experimental Processing Flowchart.

Precision refers to the proportion of true positive instances among all instances classified as positive. The formula for precision is given in Equation (12).

$$Precision = \frac{TP}{TP + FP} \tag{12}$$

Recall refers to the proportion of true positive instances that are correctly predicted as positive by the classifier among all true positive instances. The formula for recall is given in Equation (13).

$$Recall = \frac{TP}{TP + FN} \tag{13}$$

F1-score is the harmonic mean of precision and recall. It combines the two metrics of precision and recall to evaluate the overall performance of a classification model. The F1-score ranges from 0 to 1, with a value closer to 1 indicating better model performance. The formula for F1-score is given in Equation (14).

$$F1 - score = \frac{2 \times Precision \times Recall}{Precision + Recall} \tag{14}$$

Mean square error (MSE) is used to calculate the average squared difference between the predicted value and the true value and can be used to measure the degree of model fit. The formula for MSE is given in Equation (15).

$$MSE = \frac{1}{n}\sum_{i=1}^{n}(Y_i - \widehat{Y}_i)^2 \tag{15}$$

Mean relative error (MRE) is used to calculate the relative error between the predicted value and the true value and can be used to reflect the degree of fluctuation in weight measurement error. The formula for MRE is given in Equation (16).

$$MRE = \frac{1}{n}\sum_{i=1}^{n}\frac{|Y_i - \widehat{Y}_i|}{Y_i} \tag{16}$$

Where n is the sample size, a is the true weight value, and b is the predicted weight value.

3.2. Classification results

Due to the differences in models, the related parameters and their hyperparameters also vary. Table 1 shows the relevant parameter settings, and experiments are conducted based on these parameter settings to provide experimental results.

The nine models have the same dataset and other parameter settings, except for differences in learning rate and dropout settings. For ResNet18, ResNet18-SE, and ResNet18SV, the learning rate decays by a factor of 0.9 in the [5, 60] epochs, with a dropout setting of 0.7, indicating that 30 % of neurons are involved in training each epoch. The remaining classification models decay by a factor of 0.9 at the 60th epoch, with a dropout setting of 0.5. The cross-entropy function measures the difference between the distribution of true labels and the probability distribution of model outputs by calculating the cross-entropy of the two distributions, defined as follows:

$$L = -\frac{1}{N}\sum_{k}\sum_{c=1}^{M} y_{ic}\log(p_{ic}) \tag{17}$$

where M represents the number of classes, y_{ic} represents the symbolic function (0 or 1); it takes the value 1 if the true category of sample i is equal to c, otherwise it takes the value 0. Here, p_{ic} represents the predicted probability that sample i belongs to category c.

During training, experiments are conducted on the network in the PyTorch framework (Paszke et al., 2019) based on the above parameter settings, and the loss rate curves of the nine test models are shown in Fig. 12.

In Fig. 12, it can be observed that the loss values of most classification models fluctuate and decrease within a certain range, eventually reaching a relatively stable state. This indicates that these classification models have good recognition and classification capabilities for this

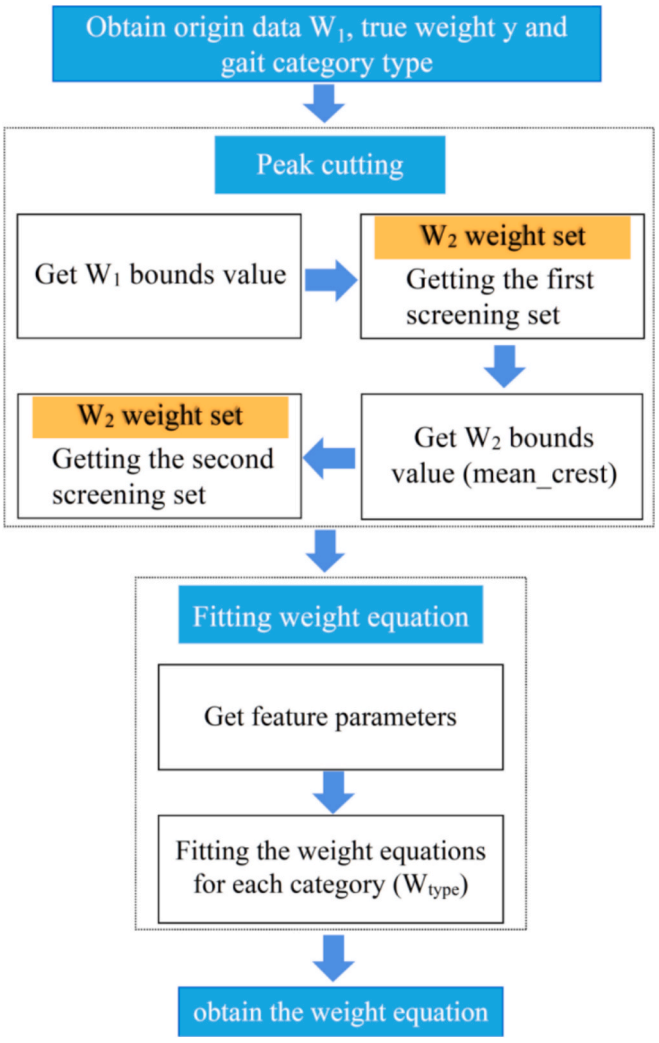


Fig. 10. Flowchart of the strategy for fitting the various types of weight equations.

dataset, highlighting the effectiveness of the dataset and the model's convergence and good generalization. Furthermore, it is evident that the loss values of our improved model exhibit better stability, indirectly indicating the improved model's more stable recognition performance. The detailed evaluation metric results of the model are provided in Table 2.

As shown in Table 2, different models have their strengths and weaknesses in terms of accuracy, precision, recall, F1 score, and parameter count. The ResNet18-SE model achieved a classification accuracy of 96 %, which is better than the original ResNet18 (93.7 %), with an improvement of 2.3 %. This is because the ResNet18-SE model focuses attention on the concave-convex positions and peak positions of the weight curve, which overall allows for better extraction of important features, thereby improving the model's classification performance. Furthermore, by replacing its classifier with the Vit model's classifier, it can be observed that ResNet18SV achieves the best overall performance among the tested models in this study, with a classification accuracy 1.1 percentage points higher than the ResNet18-SE model. In addition, RIFormer excels in accuracy and F1 score, ResNet18SV has a higher precision, and MobileNetSV has the advantage of fewer parameters. However, considering both parameter count and accuracy, the ResNet18SV model performs the best among these models, with the highest precision and recall, and only a 0.2 % lower accuracy than the best-performing model, which is entirely within an acceptable range for practical applications. This also indicates that the SE attention mechanism plays a significant role in the ResNet18 model, enabling the network to focus on more prominent features, such as the peaks in the waveform. Furthermore, the classifier in the ViT model contributes significantly to extracting more important feature information and enhancing its classification capability. It can also be seen that the recognition and classification abilities of ResNet18SV and ViT models are comparable, but our model is more lightweight. The MobileNetSV model is even more lightweight than the ResNet18SV model, but its recognition rate is much lower than that of the latter. In summary, the improved model strikes a balance between lightweight design and accuracy, outperforming the comparative models in both aspects and is better suited for practical applications.

3.3. Weight prediction results

3.3.1. Secondary peak extraction results

Table 3 compares the relative error results of the primary and secondary peak extraction methods for pig weight prediction at different gaits as well as the average relative error results, in which the average error of primary extraction is 0.57 %, while the average error of secondary extraction is reduced to 0.28 %, with an overall error reduction of about 50 %. And the error of each type of gait in the secondary extraction is smaller than that of the primary extraction, and this significant difference reflects the fundamental difference between the two methods in parameter screening. As the secondary extraction is further optimized on the basis of the primary extraction, it can more accurately and adaptively obtain the weight sequence parameters that are not much different from the real weight. From the specific results, the secondary extraction achieves a significant reduction of error in all gaits, especially in the slow gait, the error is reduced from 0.47 % to 0.16 %, which is the most obvious improvement of accuracy; and in the linger gait, which has the highest error, the error of the secondary extraction is also reduced from 0.67 % to 0.45 %, which still exhibits a good improvement effect. Because of the large fluctuation of ups and downs in the linger gait, the parameters after the secondary extraction contain the top part of the parameters of the primary extraction, removing the parameters at the end of the comparison. For the more fluctuating gaits, the error generated by the secondary extraction is not much different from that of the primary extraction, while 60 % of the data in the linger gait data are for the more fluctuating gaits. Overall, the secondary extraction method can adaptively obtain parameter selection thresholds and more accurately acquire weight sequence parameters that are close to the true weight, making the obtained data more refined and significantly improving the accuracy of the prediction results.

3.3.2. Analysis of weight prediction results

The parameters such as maximum value (w_max), median (w_median), and mode (w_mode) can be obtained through the regression strategy in Section 2.3.2, measured in kilograms. These parameters can be used to establish various weight regression models. It was found that the coefficient of the minimum value (w_min) and the average of the local minima (mean_minimum) is very small, indicating that their influence on weight is negligible in the experiment. Therefore, the parameters w_min and mean_minimum were excluded from the experiment, and the weight regression model was re-established. Table 4 presents the predictive performance of various regression models for different categories.

In Table 4, it is evident that different methods yield varying prediction results for different categories. Among the Fast and Normal categories, the most effective method for weight prediction involves using linear regression to fit weight equations with relevant parameters, indicating a clear linear relationship among the parameters obtained through the quadratic peak extraction algorithm. In the slow category, the best prediction results are achieved by averaging the parameters. The average relative error rate is only 0.16 %, indicating that the extracted parameters closely approximate the true weight values,

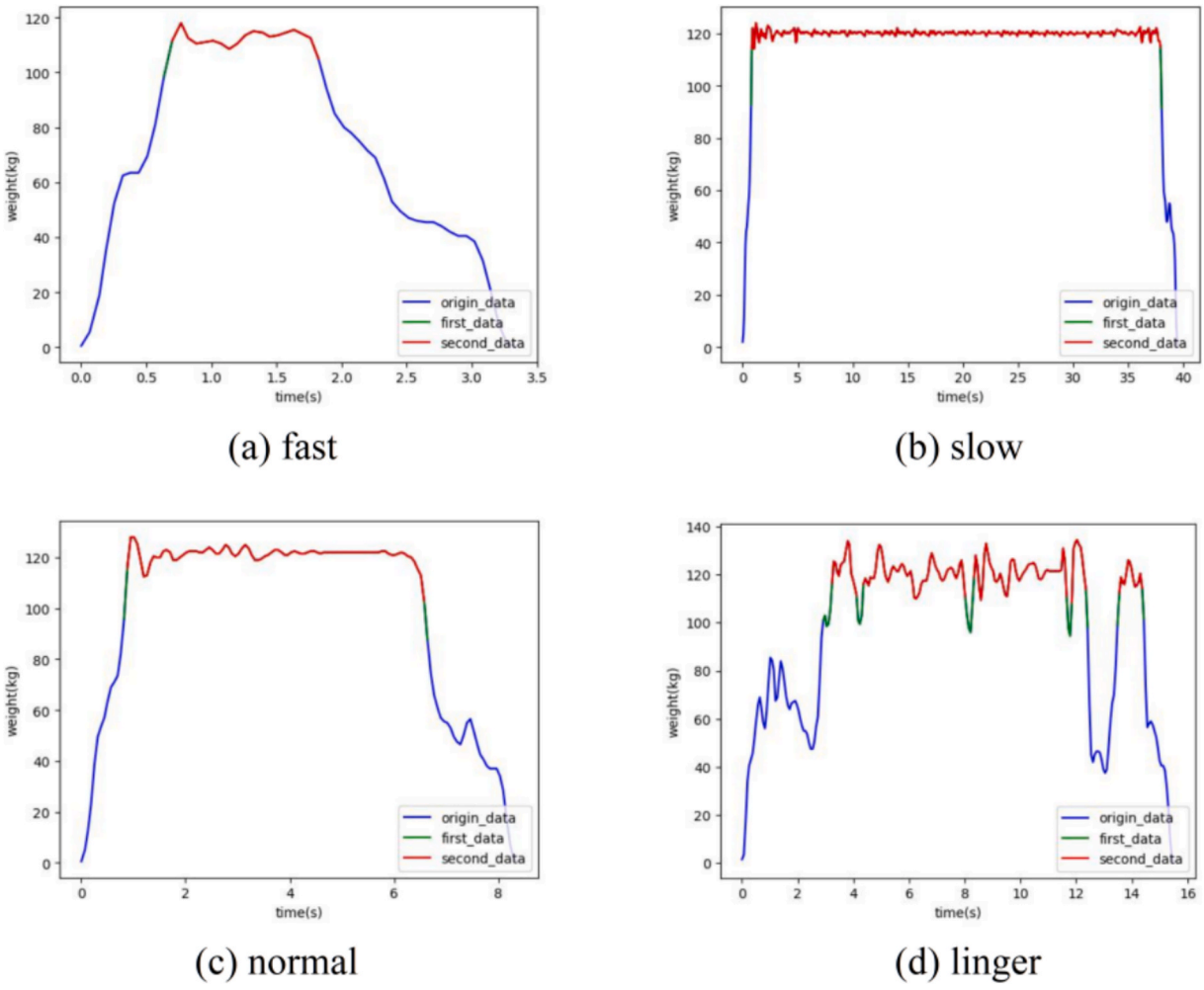


Fig. 11. The changes in weight data extraction for various gaits of pigs, where the horizontal axis represents time and the vertical axis represents actual weight. The blue curve indicates the original data, the green plus blue curve indicates the data after the first selection, and the red plus green plus blue curve indicates the data after the second selection.

Table 1
Model parameter setting.

Model parameter	optimizer	Learning rate	Dropout	Epoch	Activation function	Loss function
ResNet18	Adam	0.0007	0.7	100	Relu	Cross-entropy
ResNet18-SE	Adam	0.0007	0.7	100	Relu	Cross-entropy
Vision-Transformer	Adam	0.00007	0.5	100	Relu	Cross-entropy
Swin-TransformerV2	Adam	0.0005	0.5	100	Relu	Cross-entropy
MobileNet	Adam	0.0005	0.5	100	Relu	Cross-entropy
ResNet18SV	Adam	0.0007	0.7	100	Relu	Cross-entropy
MFF	Adam	0.0007	0.7	100	Relu	Cross-entropy
RIFormer	Adam	0.0007	0.7	100	Relu	Cross-entropy
YOLOv11	Adam	0.0003	0.7	100	Relu	Cross-entropy

underscoring the importance and effectiveness of the quadratic peak extraction strategy. For the Linger category, the prediction results obtained by various methods show minor differences. However, the numerical differences in parameters are more pronounced compared to the other categories, resulting in the highest average relative error rate. This is attributed to significant data variations caused by intense pig movement, leading to the presence of certain nonlinear relationships in the extracted parameters and reduced prediction accuracy. By comparing the prediction accuracy of various methods, the models with the highest prediction accuracy for each category are ultimately determined and presented in Equations (18)–(21).

$$W_{fast} = 0.43 + 0.25\,\omega_0 - 0.07\omega_2 + 0.02\omega_3 - 0.03\omega_4 + 0.83\omega_6 \quad (18)$$

$$W_{slow} = \omega_6 \quad (19)$$

$$W_{normal} = 0.5 + 0.06\,\omega_0 - 0.05\omega_2 + 0.03\omega_3 - 0.03\omega_4 + 0.99\omega_6 \quad (20)$$

$$W_{linger} = 3.45 + 0.017\,\omega_0 - 0.069\omega_2 + 0.027\omega_4 + 1.06\omega_6 \quad (21)$$

where ω_i (i = 0, 1…, 6) represents the maximum value, the minimum value, the median, the mode, the mean of maximum values, the mean of minimum values, and the average value (w_mean). It can be observed that the impact of the same parameter varies across different categories, and the influence of different parameters within the same category also differs, primarily depending on the magnitude of the coefficients' absolute values. In this regard, when the absolute value of the coefficient is

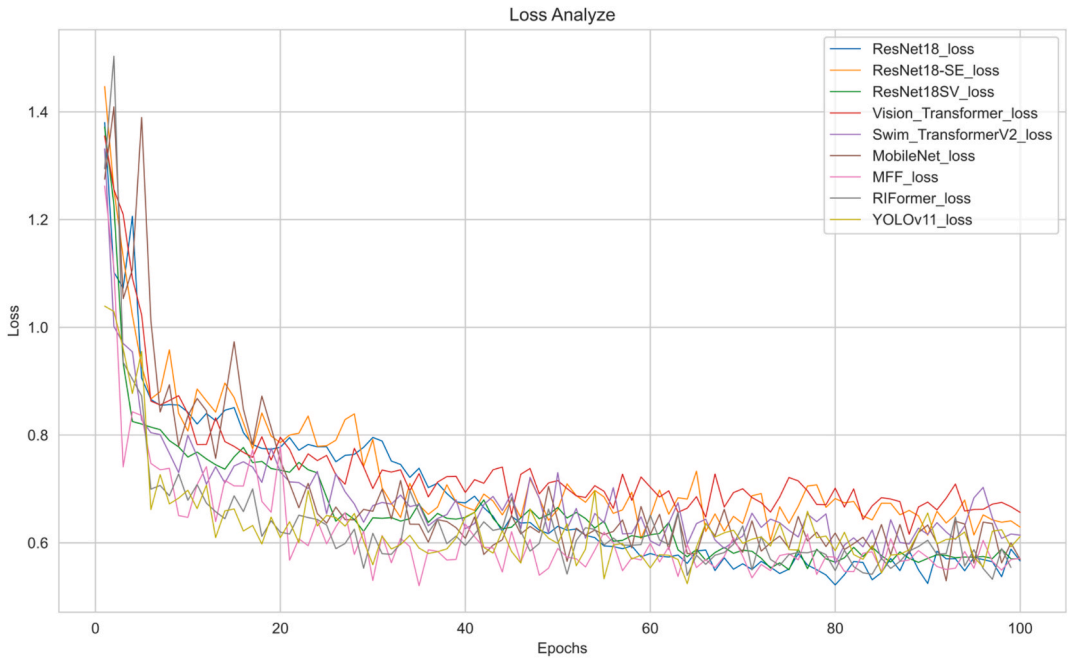


Fig. 12. The loss rate curve of the test set under the model.

Table 2
The classification results of the test set at the best epoch.

Model	Accuracy (%)	Precision (%)	Recall (%)	F1-score (%)	#Param (MB)
ResNet18	93.7	93.6	93.5	93.5	11.3
ResNet18-SE	96.0	95.5	94.2	94.7	11.3
Vision-Transformer	96.6	96.9	95.0	95.8	86.1
Swin-TransformerV2	95.5	95.2	95.0	95.0	42.1
MobileNetSV	93.8	94.3	93.7	93.8	**1.52**
MFF	94.2	94.6	93.7	94.1	86.57
RIFormer	**97.3**	97.1	97.0	**97.3**	56.3
YOLOv11	96.3	96.2	95.4	96.1	28.5
ResNet18SV	97.1	**97.2**	**97.1**	97.1	11.8

Table 3
Average relative error results of weight prediction after primary and secondary extraction.

Extraction Method	Type				
	Fast	Slow	Normal	Linger	Mean
Primary extraction error	0.62 %	0.47 %	0.53 %	0.67 %	0.57 %
Secondary extraction error	0.31 %	0.16 %	0.21 %	0.45 %	0.28 %

less than 5×10^{-4}, meaning the influence of a specific parameter on the predicted weight is below 0.05 %, it is considered negligible in the model. This implies that its impact on the weight prediction result can be ignored. Evidently,arameters with the most significant impact have higher decision-making power across all categories, indicating that the data extracted in the second round is more detailed and precise. This also suggests that when there is minimal fluctuation in dynamic weight changes, the average data values are very close to the true weight values. Fig. 13 illustrates the comparison between the final predicted results and the true weight by inputting the datasets of different categories into various regression models.

From Fig. 13, it can be seen that the predicted results and actual weight values of each category mostly overlap, indicating a small difference between the two. However, there are instances where the differences are more pronounced. For example, in the Fast category, there is a significant discrepancy in predicting the weight of the 90th pig, which can be attributed to the pigs moving too quickly on the scale, resulting in limited top data and biased parameter acquisition, ultimately leading to increased errors. In the slow and normal categories, both can accurately predict weight. By examining Equations (19) and (20), it is evident that the coefficient for the mean value in the normal category is almost close to 1, with other parameters fine-tuning around the mean value parameter. The pigs passing through the scale normally and slowly without any abnormal behavior result in smooth dynamic weight data acquisition, enabling accurate weight prediction. In the Linger category, there is a more significant discrepancy between the predicted and actual weight values. Due to the livestock being more active on the scale, the o btained parameter ω_i is noticeably higher than the actual weight. For some pigs, more than half of the weight sequence data is lower than the true weight. This is also the case for the sequence data obtained using the secondary threshold extraction method. As seen in Fig. 13(d), some predicted values are smaller than the true weight values. By combining with equation (21), it can be found that ω_6 is the most important parameter, and at this point, ω_6 is smaller than the true weight. Additionally, the adjustment coefficient for ω_2 is relatively large, so the predicted weight is much smaller than the actual weight.

Table 4
The average relative error rate of predictions for different categories across various models.

Gait category	Linear regression	Ridge regression	Lars regression	ElasticNetCV regression	SVR regression	Average
Fast	**0.31 %**	0.64 %	0.34 %	0.34 %	0.32 %	0.4 %
Slow	0.2 %	0.54 %	0.26 %	0.28 %	0.23 %	**0.16 %**
Normal	**0.21 %**	0.27 %	0.39 %	0.38 %	0.35 %	0.41 %
Linger	0.54 %	0.48 %	0.56 %	0.52 %	**0.45 %**	0.66 %

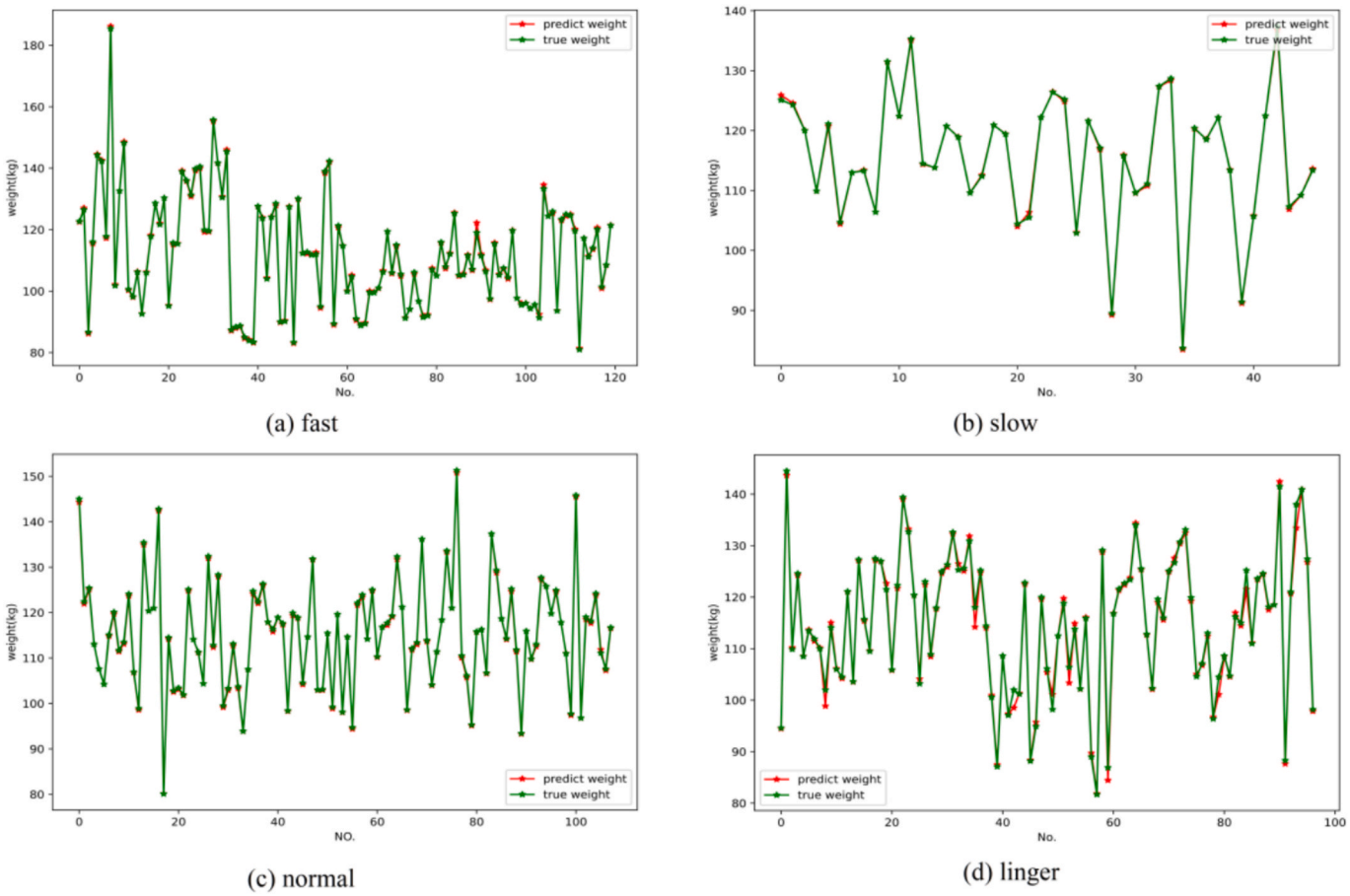


Fig. 13. A comparison chart of weight prediction results and actual weight values. The horizontal axis represents the number of samples in the test set, while the vertical axis represents the weight values. The red curve represents the predicted weight values, and the green curve represents the actual weight values. (For interpretation of the references to colour in this figure legend, the reader is referred to the web version of this article.)

Although the secondary threshold extraction method leads to some weight sequence data significantly deviating from the true weight, the method is still highly effective overall. Although readjusting the maximum value may not have a particularly pronounced effect on individual data points, the strategy of adjusting the local maximum value still has advantages as it can reduce the discrepancies between the most predicted results and the actual weight values, which also serves as a correction for the secondary threshold extraction method.

3.3.3. *Stability analysis*

Fig. 14 illustrates the weight prediction result errors for some pigs. The straight lines extending parallel to the X-axis from points (x, 0) serve as dividing lines, with greater distance from the dividing line indicating larger prediction errors. It is evident that the prediction errors vary among different pigs and even within the same pig due to the variations in gait during multiple measurements. The largest difference in prediction error is observed for pig number 6, attributed to its gait categories, including slow, normal, and linger. The weight fluctuations in the linger category for pig 6 are significant, with sparse peak data leading to poor prediction performance. Additionally, the prediction accuracy for the slow gait category is higher than that for the linger category, further widening the error gap between these two categories. While other pigs have multiple gait categories, the fluctuations in their weight are relatively smooth, resulting in minimal differences in prediction errors. It can also be observed that the prediction errors for the majority of pigs are not significant, indicating the high stability of the algorithm proposed in this study and the reliability of the obtained results.

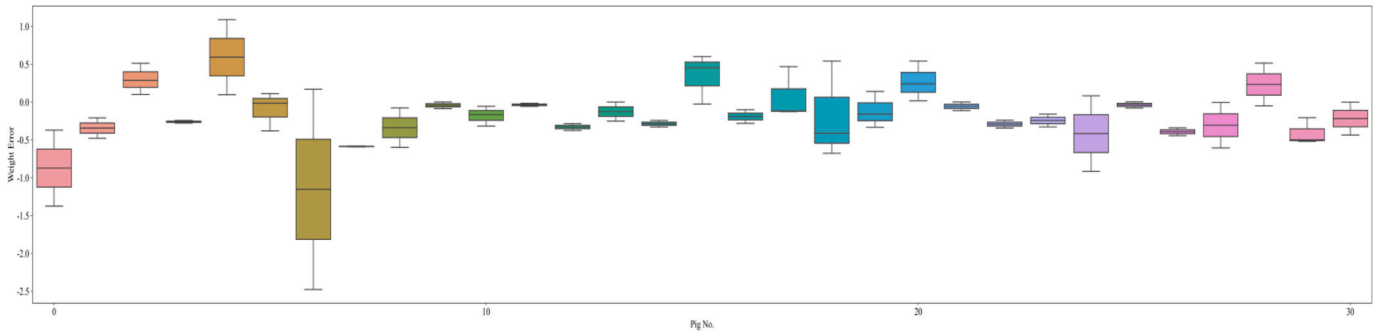


Fig. 14. Weight prediction result error stability analysis.

3.3.4. Classification importance analysis

In the experiment, the chi-square test was employed to demonstrate the relationship between gait categories and dynamic weight, as shown in Table 5. For each gait category, 100 data samples were selected, and Equation (23) was used to predict the weight. The number of pigs within different ranges of average relative error for each gait category was obtained. Subsequently, the test statistic X^2 was calculated using Equation (22) and compared with the significance level α (defaulted to 0.05). The results indicated that $X^2 \approx 26.66 > X^2_{1-\alpha} = 16.919$, demonstrating that at a significance level of $\alpha = 0.05$, gait categories are associated with relative weight error, thereby confirming the relationship between gait categories and dynamic weight.

$$X^2 = n \times \left(\sum_{i=1}^{r} \sum_{j=1}^{s} \frac{n_{ij}^2}{n_{i.} n_j} - 1 \right) \tag{22}$$

where n is the total number of samples, n_{ij} represents the frequency of the *i-th* gait category and the *j-th* relative weight error group, $n_{i.}$ is the total frequency of the *i-th* gait category, n_j is the total frequency of the *j-th* relative weight error group, r is the number of gait categories, and s is the number of relative weight error groups.

In this study, the training sets of the four categories are combined to fit the weight regression equation, and the difference between the predicted weight results and the actual weight is observed, while exploring the importance of classification. Formula (23) represents the weight regression equation, and the comparison between predicted weight and actual weight is shown in Fig. 15.

$$W_{all} = 0.97 + 0.36\omega_0 + 0.32\omega_2 + 0.1\omega_3 - 0.03\omega_4 + 0.23\omega_6 \tag{23}$$

From formula (23), it can be seen that the weight results are mainly determined by ω_0、ω_2 and ω_6, and the coefficient of the penalty term ω_4 is relatively small, indicating that the predicted results may be higher or lower for certain categories. From formulas (18) to (21), it can be observed that the impact of ω_6 on each category is significant, but the coefficient of ω_6 in formula (23) does not carry much weight. Additionally, the adjusted value of ω_0 tends to be lower than the average value of some categories. Although it may not be able to adapt to all category situations, as seen in Fig. 15, this approach yields the best overall results, leading to an overall underestimation in predicted results. Comparing the strategy of classification before weight prediction, it can be observed that using corresponding strategies for each category to predict weight values tends to be closer to the true values. This directly highlights the importance of classification before weight prediction.

Fig. 16 displays the mean square error (MSE) and average relative error (MRE) of the predicted weight and actual weight for each category and all categories combined. From Fig. 16 (b), it can be observed that the average relative errors for the four categories are 0.31 %, 0.16 %, 0.21 %, and 0.45 % respectively, while the average relative error for "all" is 0.97 %. This indicates that fitting a weight equation for each gait category results in smaller weight prediction errors compared to fitting a single equation, resulting in predictions closer to the actual values. For the fast category, most predicted weights closely match the actual weights, but the MSE is 0.38. This is due to the significant weight fluctuations and short duration on the scale when animals pass quickly, leading to occasional overestimation of weights for individual data points, as seen in the 90th test data point in Fig. 13 (a), resulting in an overall bias. The slow and normal categories show minimal differences between predicted and actual weights, with MSE around 0.3. The weight values within the peak range for these categories closely match the actual weights, with smooth peak data leading to low fluctuations. As shown in Fig. 16 (b), the errors are around 0.2 %, indicating highly accurate weight predictions for these categories. For the linger category, despite occasional intense movements or abnormal behaviors on the scale, the average relative error is 0.45 %, demonstrating the method's ability to estimate weight accurately. Similarly, for other category peaks with gentle data fluctuations, weight predictions are accurate with low errors. Considering the "all", where a single curve equation predicts weights for all categories, the MSE is high at 1.14. This directly suggests that fitting a weight equation for each gait category yields much better results than fitting a single equation for all categories.

Table 5
Number of pigs within different margins of error for each gait category.

MeanRelative error	Gait category				
	Fast	Slow	Normal	Linger	Sum
|error| < 0.1 %	22	36	32	15	105
0.1 % < |error| < 0.2 %	27	24	26	24	101
0.2 % <|error| < 0.5 %	31	23	28	24	106
|error| > 0.5 %	20	17	14	37	88
Sum	100	100	100	100	400

Next, let's explore the situation of weight prediction deviation when category prediction is incorrect. In Fig. 17(a), it shows the average absolute error between the predicted weight using the weight equation of the predicted category and the actual weight when the category prediction is wrong. Fig. 17(b) illustrates the average absolute error between the predicted weight using the weight equation of the actual category and the actual weight when category prediction is wrong. From Fig. 17(a), when the linger category is predicted as the slow category, the average absolute error in estimating weight is significant, at 1.22 kg. Conversely, in Fig. 17(b), for the corresponding category where the predicted category matches the actual category, the estimated weight's average absolute error is around 0.7 kg. The notable difference in errors is due to significant differences in gait fluctuations between the two categories. The linger category exhibits irregular weight fluctuations with unpredictable peak variations, resulting in notable differences between extracted parameters and actual weights. In contrast, the slow category shows smoother gait fluctuations with minimal differences between extracted parameters and actual weights. Therefore, when using the weight equation of the slow category to predict the weight of the linger category, the method of predicting weight using average values for the significant peak variations in the linger category often leads to larger prediction errors. For many categories where prediction errors occur, using the weight equation of that category to predict weight results in significantly larger average absolute errors compared to using the weight equation of the actual category. This is because the range of fluctuations around each peak for each category varies, and different methods and extracted data lead to significant differences in the weight regression equations fitted, resulting in vastly different weight predictions, as demonstrated in Fig. 17. This underscores the necessity and importance of classification accuracy. Therefore, the method of classifying first and then fitting weight equations proves more effective than fitting one weight equation for all datasets, and it can be effectively applied in practical engineering applications.

4. Discussion

Fig. 18 and Fig. 19 show a comparison of the livestock classification model and weight regression equation for weight prediction of 118 buffaloes and 62 goats. The average relative prediction error for buffaloes is 0.64 %, and for goats, it is 1.98 %. As shown in Fig. 18, the actual weight of buffaloes is very close to the predicted weight, indicating that our model has good generalization ability and can be directly applied to the buffalo breed. From Fig. 19, it can be seen that our model still requires significant improvements in predicting the weight of goats. Due to the different average weights of pigs (about 120 kg), buffaloes (500–1000 kg), and goats (about 30–40 kg), the same model shows considerable differences when predicting the weight of cows and goats. Additionally, the impact of each parameter varies across different breeds. Since goats are lighter and generally more active, they usually pass through the scale quickly, and even small deviations in predicted

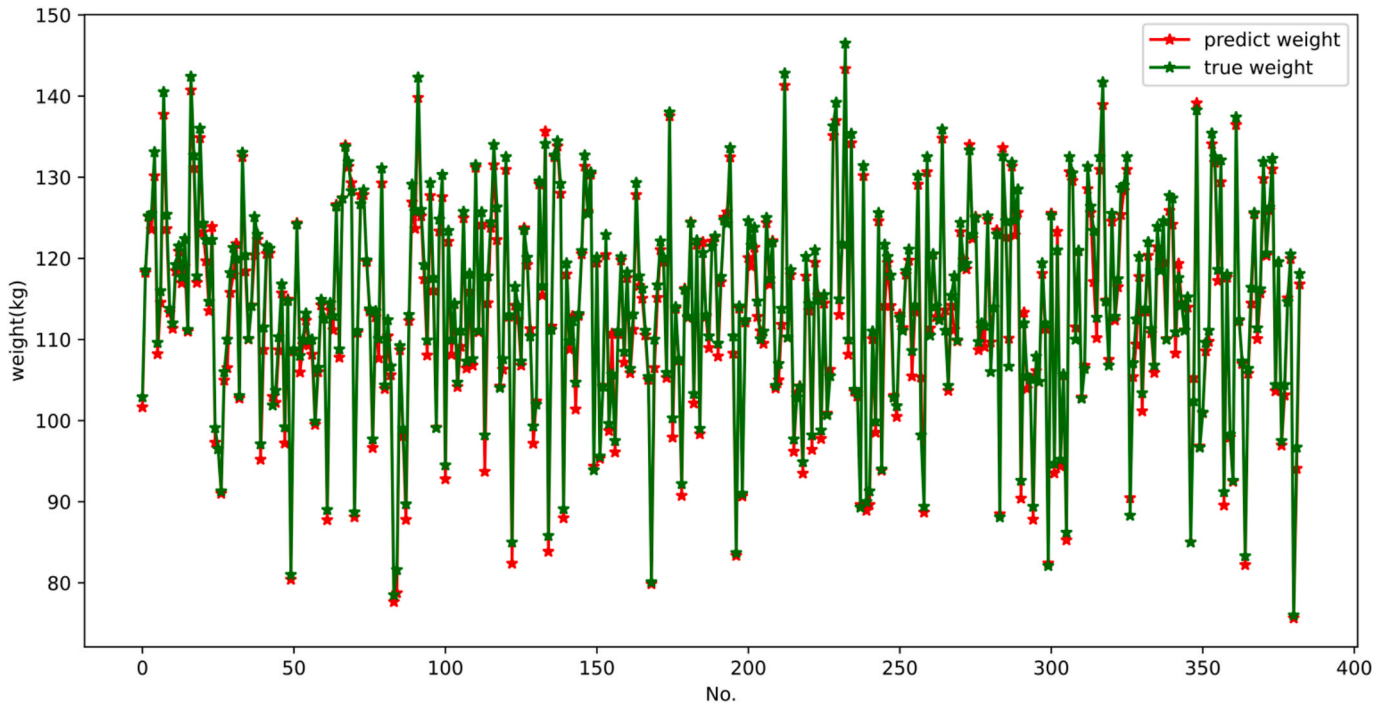


Fig. 15. Comparison between body weight values predicted by fitting only one regression equation and true body weight for various behaviors in pigs. The horizontal axis represents the number of samples in the test set, while the vertical axis represents the weight values. The red curve represents the predicted weight values, and the green curve represents the actual weight values.

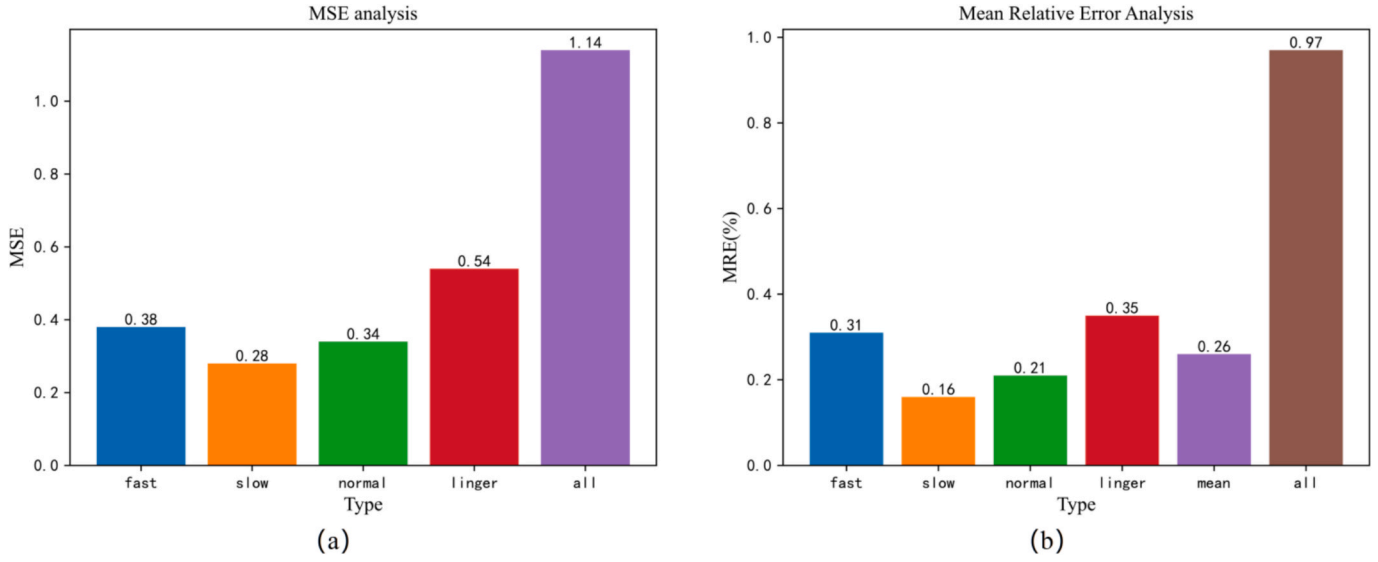


Fig. 16. Error Analysis. (a) represents the mean square error for each category, while (b) indicates the average relative error for each category. "mean" denotes the average error values for the four categories, and "all" represents the errors calculated by fitting a weight regression equation to all datasets.

weight result in large errors. On the other hand, buffaloes are relatively calm when standing on the scale, and their heavier weight reduces the influence of small deviations. Therefore, for livestock breeds such as pigs and buffaloes, which are not very light or move slowly across the scale, the experimental classification model and weight regression model show good portability, scalability, and accuracy.

From Fig. 11, it can be observed that the weight data extracted using this algorithm are all weights measured on the scale when pigs are standing on all fours. The data obtained in the second extraction are more detailed, precise, and closer to the true weight values compared to the first extraction. If using 85 % to 90 % or higher of the maximum value of the original data directly as the threshold, a small portion of data may be selected that is similar to the data obtained in the second extraction. However, the majority of the data would only include heavier weight data, leading to an overall overestimation of predicted weights. Additionally, using a fixed percentage as a threshold is not suitable for selecting data across various behavioral categories. In contrast, the data obtained in the second extraction uses the average of the maximum and minimum values as the threshold, which is more appropriate for the overall dataset. This method results in more reasonable, detailed, and accurate data selection, with strong applicability across various behavioral categories. Therefore, after the second

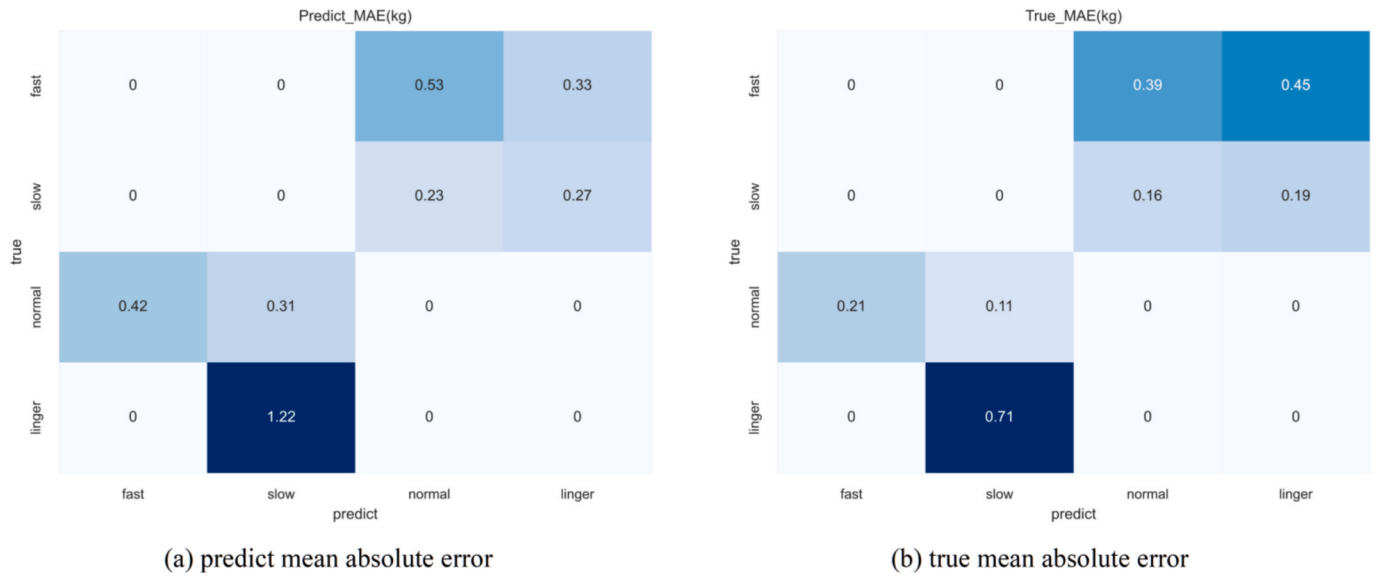


Fig. 17. Weight prediction deviation comparison chart. The horizontal axis represents the predicted category, and the vertical axis represents the actual category.

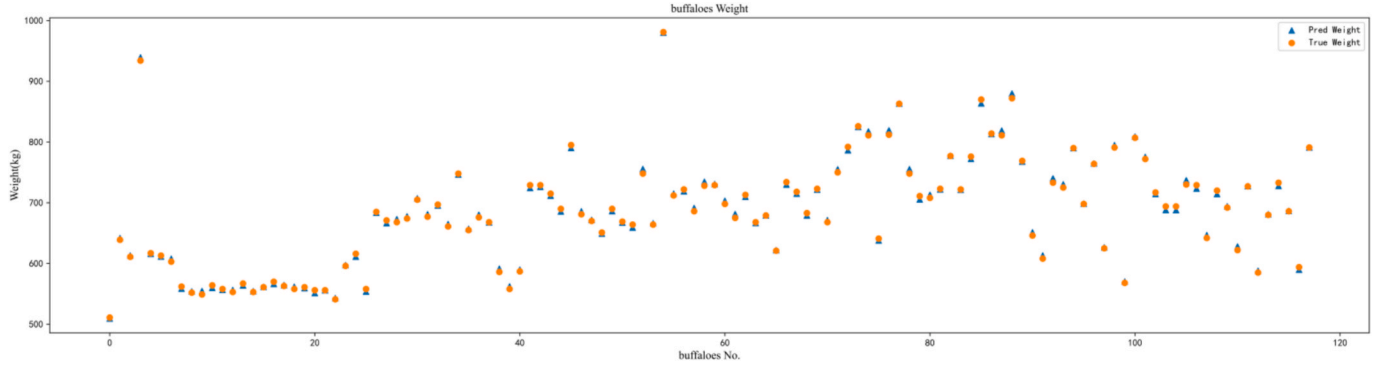


Fig. 18. Comparison of predicted weights and true weights of buffaloes graph.

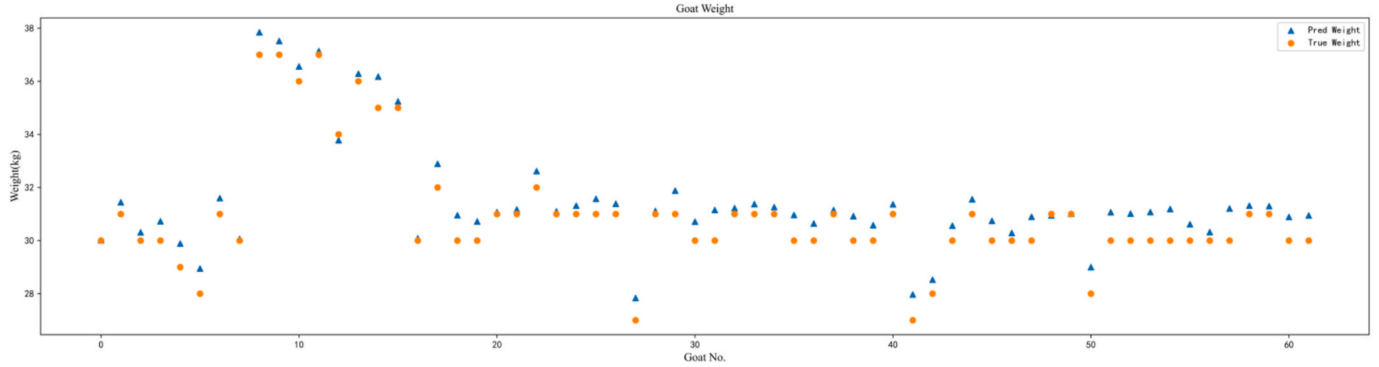


Fig. 19. Comparison of predicted and true body weights of goats.

data extraction, training a regression model can result in a stable and highly generalizable model, leading to more accurate weight predictions. In Fig. 13(d), it can be noticed that there are extreme fluctuations in specific scenarios where the error increases, such as when pigs are in heat or sick. But this error is also within the accepted range, so for this study the quadratic peak extraction method is suitable for extreme fluctuations. In the subsequent study the extreme fluctuation weight curve will be rounded to further improve the accuracy.

The ResNet18SV model may encounter some latency under limited computational resources (such as on edge devices), but it can still meet the demands of practical applications. The performance of the ResNet18SV model could be impacted when handling more complex datasets. For example, when livestock behavior becomes more complex or waveform features exhibit significant variations, the stability and accuracy of the model may decrease. This is because fast and linger gaits sometimes cause significant variations in the peak segments, and the accuracy of the weight prediction by the regression model can also be affected. This is due to the fewer extracted weight features, which may

lead to greater deviations in the obtained parameters, ultimately resulting in increased weight prediction errors.

5. Conclusion

In this study, we collected dynamic weight data of pigs for experimentation and proposed using the ResNet18SV classification model to categorize pig walking weight signals into four gait categories: fast, slow, normal, and linger. Subsequently, the regression model was used to train the data for each category, and a weight regression equation for weight prediction was tailored for each category of gait. The experimental results showed that the classification model achieved an accuracy of 97.1 %, providing a strong foundation for accurate weight calculations. The average relative errors for weight prediction in each category were 0.31 %, 0.16 %, 0.21 %, and 0.45 %, all of which were below 0.5 %. This indicates that our proposed method offers higher weighing accuracy compared to previous dynamic weighing algorithms. In addition to accurately predicting pig weights, our method combines the behavioral classification results of pigs with weight predictions to assess if pigs are experiencing stress reactions, enabling cost-effective monitoring of pig health. In conclusion, the method proposed in this paper meets the needs of smart livestock farming by effectively addressing the issues of dynamic pig weighing and behavioral classification. This method is suitable for widespread application in breeding enterprises, reducing the human, material, and financial resources required for pig weighing and health monitoring. It also helps reduce animal stress responses and improve animal welfare. Future research plans include expanding overall data collection and extending the livestock species range to further improve the accuracy and robustness of the algorithm, better meeting the requirements of industry applications.

CRediT authorship contribution statement

Sumin Zhang: Writing – review & editing, Resources, Methodology. **Jinfa Peng:** Writing – original draft, Visualization, Investigation. **Qiong Huang:** Project administration. **Zhikun Li:** Validation. **Ling Yin:** Resources, Project administration, Funding acquisition.

Declaration of competing interest

The authors declare that they have no known competing financial interests or personal relationships that could have appeared to influence the work reported in this paper.

Acknowledgements

The authors would like to thank Guangdong Wen's Food Group Co., Ltd. for generously providing the experimental materials. Additionally, we sincerely appreciate all individuals who assisted us in obtaining data and manually measuring the target pigs. This project was supported by the National Science and Technology Planning Project [2023YFD1300202], the National Natural Science Foundation of China [32172780] , the National Engineering Research Center for Swine Breeding Industry, and the State Key Laboratory of Swine and Poultry Breeding Industry.

Data availability

Data will be made available on request.

References

Alawneh, J.I., Stevenson, M.A., Williamson, N.B., Lopez-Villalobos, N., Otley, T., 2011. Automatic recording of daily walkover liveweight of dairy cattle at pasture in the first 100 days in milk. J. Dairy Sci. 94, 4431–4440. https://doi.org/10.3168/jds.2010-4002.

Bigonah, M., Jamshidi, F., Marghitu, D., 2024. Immersive Agricultural Education: Gamifying Learning With Augmented Reality and Virtual Reality. IGI Global 26–76. https://doi.org/10.4018/979-8-3693-1710-5.ch002.

Cang, Y., He, H., Qiao, Y., 2019. An Intelligent Pig Weights Estimate Method Based on Deep Learning in Sow Stall Environments. IEEE Access 7, 164867–164875. https://doi.org/10.1109/ACCESS.2019.2953099.

Cassimiro, A.N., Ramos, E.S., Cabrera, V.E., Freitas, E., Milk weighing scale based on machine learning, Smart Agricultural Technology, Volume 7, 2024, 100417, ISSN 2772-3755, doi: 10.1016/j.atech.2024.100417.

Choi, H., Cho, K., Bengio, Y., 2018. Fine-grained attention mechanism for neural machine translation. Neurocomputing 284, 171–176. https://doi.org/10.1016/j.neucom.2018.01.007.

Cveticanin, D., Wendl, G., 2004. Dynamic weighing of dairy cows: using a lumped-parameter model of cow walk. Comput. Electron. Agric. 44, 63–69. https://doi.org/10.1016/j.compag.2004.03.001.

Dickinson, R.A., Morton, J.M., Beggs, D.S., Anderson, G.A., Pyman, M.F., Mansell, P.D., Blackwood, C.B., 2013. An automatedwalk-over weighing system as a tool for measuring liveweight change in lactating dairy cows.J. Dairy Sci 96, 4477–4486. https://doi.org/10.3168/jds.2012-6522.

Dongmei, H., Yueqi, W., Anduo, H., Jindong, S., Shuai, S., Yuan, S., Lingfeng, F., 2022. Insulator state edge recognition method based on multi-dimensional features. Electric Power 55 (01), 133–141.

Dosovitskiy, A., Beyer, L., Kolesnikov, A., Weissenborn, D., Zhai, X., Unterthiner, T., Dehghani, M., Minderer, M., Heigold, G., Gelly, S., Uszkoreit, J., & Houlsby, N., 2020. An Image is Worth 16x16 Words: Transformers for Image Recognition at Scale. ArXiv, abs/2010.11929. doi: 10.48550/arXiv.2010.11929.

Fernandes, A.F., Turra, E.M., Alvarenga, É.R., Passafaro, T.L., Lopes, F.B., Alves, G.F., Singh, V., Rosa, G.J., 2020. Deep Learning image segmentation for extraction of fish body measurements and prediction of body weight and carcass traits in Nile tilapia. Comput. Electron. Agric. 170, 105274. https://doi.org/10.1016/j.compag.2020.105274.

González-García, E., Alhamada, M., Nascimento, H., Portes, D., Bonnafe, G., Allain, C., Llach, I., Hassoun, P., Gautier, J.M., Parisot, S., Measuring liveweight changes in lactating dairy ewes with an automated walk-over-weighing system, Journal of Dairy Science, Volume 104, Issue 5, 2021, Pages 5675-5688, ISSN 0022-0302, doi: 10.3168/jds.2020-19075.

González-García, E., Alhamada, M., Pradel, J., Douls, S., Parisot, S., Bocquier, F., Menassol, J.B., Llach, I., González, L.A., 2018. A mobile and automated walk-over-weighing system for a close and remote monitoring of liveweight in sheep. Comput. Electron. Agric. 153, 226–238. https://doi.org/10.1016/j.compag.2018.08.022.

Guixin, L., Xinliang, L., Yafang, M., Bingbing, W., Lihua, Z., Minjuan, W., 2022. Body size measurement and live body weight estimation for pigs based on back surface point clouds. Biosyst. Eng. https://doi.org/10.1016/j.biosystemseng.2022.03.014.

Haikun, Z., Cheng, F., Tiemin, Z., Hongzhi, Z., Jikang, Y., Chuang, M., 2022. Shank length and circumference measurement algorithm of breeder chickens based on extraction of regional key points. Comput. Electron. Agric. 197, 106989. https://doi.org/10.1016/j.compag.2022.106989.

Hengxiang, H., Yulong, Q., Ximen, L.i., Chunyu, C., Xingfu, Z., 2021. Automatic weight measurement of pigs based on 3D images and regression network. Comput. Electron. Agric. 187, 106299. https://doi.org/10.1016/j.compag.2021.106299.

Jia, N., Kootstra, G., Koerkamp, P.G., Shi, Z., Du, S., 2021. Segmentation of body parts of cows in RGB-depth images based on template matching. Comput. Electron. Agric. 180, 105897. https://doi.org/10.1016/j.compag.2020.105897.

Jie, H., Li, S., Samuel, A., Gang, S., Enhua, W., 2017. Squeeze-and-Excitation Networks. IEEE/CVF Conference on Compute Vision and Pattern Recognition 2018, 7132–7141. https://doi.org/10.48550/arXiv.1709.01507.

Kaiming, H.X.Z., Shaoqing, R., Jian, S., 2015. Deep Residual Learning for Image Recognition. IEEE Conference on Computer Vision and Pattern Recognition (CVPR) 770–778. https://doi.org/10.48550/arXiv.1512.03385.

Kwon, K., Park, A., Lee, H., Mun, D., 2023. Deep learning-based weight estimation using a fast-reconstructed mesh model from the point cloud of a pig. Comput. Electron. Agric. 210, 107903. https://doi.org/10.1016/j.compag.2023.107903.

Labbaf Khaniki, M.A., Mirzaeibonehkhater, M., Manthouri, M., 2023. Enhancing Pneumonia Detection using Vision Transformer with Dynamic Mapping Re-Attention Mechanism. In: 2023 13th International Conference on Computer and Knowledge Engineering (ICCKE), pp. 144–149. https://doi.org/10.1109/ICCKE60553.2023.10326313.

Ningning, F., Xi, K., Haoyuan, H., Gang, L., Yan'e, Z., Shuli, M., 2020. Research on a Dynamic Algorithm for Cow Weighing Based on an SVM and Empirical Wavelet Transform. Sensors (Basel, Switzerland) 20. https://doi.org/10.3390/s20185363.

Mehrnia, M., Kholmovski, E., Katsaggelos, A., Kim, D., Passman, R.S., & Elbaz, M.S., 2024. Novel Self-Calibrated Threshold-Free Probabilistic Fibrosis Signature Technique for 3D Late Gadolinium Enhancement MRI. IEEE transactions on biomedical engineering, PP. doi: 10.1109/TBME.2024.3476930.

Hasan, F.M., Thomson, P.C., Islam, M.R., Cameron E.F. Clark, Chlingaryan, A., Lomax, S., Monitoring cattle liveweight using a mobile, in-paddock weigh platform: Validation, attendance and utility, Smart Agricultural Technology, Volume 9, 2024, 100639, ISSN 2772-3755, doi: 10.1016/j.atech.2024.100639.

Pastell, M., Takko, H., Groehn, H., Hautala, M., Poikalainen, V., Praks, J., Veermäe, I., Kujala, M.A., Ahokas, J., 2006. Assessing cows' welfare : weighing the cow in a milking robot. Biosyst. Eng. 93, 81–87. https://doi.org/10.1016/j.biosystemseng.2005.09.009.

Paszke, A., Gross, S., Massa, F., Lerer, A., Bradbury, J., Chanan, G., Killeen, T., Lin, Z., Gimelshein, N., Antiga, L., Desmaison, A., Köpf, A., Yang, E., DeVito, Z., Raison, M., Tejani, A., Chilamkurthy, S., Steiner, B., Fang, L., Bai, J., & Chintala, S. (2019).

PyTorch: An Imperative Style, High-Performance Deep Learning Library. Neural Information Processing Systems. doi: 10.48550/arXiv.1912.01703.
Peiper, U.M., Edan, Y., Devir, S.E., Barak, M., Maltz, E., 1993. Automatic weighing of dairy cows. J. Agric. Eng. Res. 56, 13–24. https://doi.org/10.1006/jaer.1993.1057.
Podlahová, Š., Smutný, L., Šoch, M., 2011. Potential Utilization of Automatic Cows Weighing for Evaluation of Health and Nutritional Condition of Herd.
Schomburg, H., Malchow, J., Sanders, O., Knöll, J., Schrader, L., Elevated platforms with integrated weighing beams allow automatic monitoring of usage and activity in broiler chickens, Smart Agricultural Technology, Volume 3, 2023, 100095, ISSN 2772-3755, doi: 10.1016/j.atech.2022.100095.
Segerkvist, K.A., Höglund, J., Österlund, H., Wik, C., Högberg, N., Hessle, A., 2020. Automatic weighing as an animal health monitoring tool on pasture. Livest. Sci. 240, 104157. https://doi.org/10.1016/j.livsci.2020.104157.
Wei, H., Yang, M., Xiangdong, D., Gang, L., Tao, L., 2023. Two-stream cross-attention vision Transformer based on RGB-D images for pig weight estimation. Comput. Electron. Agric. 212, 107986. https://doi.org/10.1016/j.compag.2023.107986.
Yousefi, O., Azami, P., Sabahi, M., Dabecco, R., Adada, B., Borghei-Razavi, H., 2022. Management of Optic Pathway Glioma: A Systematic Review and Meta-Analysis. Cancers 14, 4781. https://doi.org/10.3390/cancers14194781.
Yousefzadeh, M., Hasanpour, M., Zolghadri, M., Salimi, F., Yektaeian Vaziri, A., Mahmoudi Aqeel Abadi, A., Jafari, R., Esfahanian, P., Nazem-Zadeh, MR., 2022. Deep learning framework for prediction of infection severity of COVID-19. Front Med (Lausanne), 9, 940960. doi: 10.3389/fmed.2022.940960.
Yuqing, H., Francesco, T., Jeremy, H., Christian, M., 2021. Predicting body weight in growing pigs from feeding behavior data using machine learning algorithms. Comput. Electron. Agric. 184, 106085. https://doi.org/10.1016/j.compag.2021.106085.
Zhijiang, H., Qian, L., Mengyuan, C., Gang, L., 2023. Dynamic weighing algorithm for dairy cows based on time domain features and error compensation. Comput. Electron. Agric. 212, 108077. https://doi.org/10.1016/j.compag.2023.108077.

Computers and Electronics in Agriculture 199 (2022) 107135

Contents lists available at ScienceDirect

Computers and Electronics in Agriculture

journal homepage: www.elsevier.com/locate/compag

Point cloud-based pig body size measurement featured by standard and non-standard postures

Yin Ling [a,b], Zhu Jimin [a], Liu Caixing [c,a], Tian Xuhong [a], Zhang Sumin [a,*]

[a] College of Mathematics and Informatics, South China Agricultural University, Guangzhou 510642, China
[b] National Engineering Research Center for Swine Breeding Industry, Guangzhou 510642, China
[c] Guangdong Wens Breeding Swine Technology Co, Ltd, XinXing 527400, China

ARTICLE INFO

Keywords:
Pig
Posture discriminant
Body size measurement
Regression model

ABSTRACT

Automatic body size measurement of livestock using 3D vision technology is one of the current research focuses. Point clouds obtained from freely walking livestock involve a variety of postures. However, measuring livestock body sizes requires their upright and straight standard postures, and non-standard measurement postures such as bending their body or lowering their head lead to inaccuracy in body size estimation. In this paper, we analyze 207 groups of point cloud data collected from 25 landrace pigs, and propose a standard posture classification algorithm. By using the algorithm based on the median skeleton extraction, 22 key points of the pig's skeleton were obtained and all joint point vector eigenvalue sets were calculated. Then Bagging-SVM Posture Classifier was constructed, and by three experts' votes, comparisons were made between the automatic classification results and the manual classification results based on standard and non-standard postures of pigs. According to the automatic calculation of four parameters including body length, body height, body width and abdominal girth in standard and non-standard postures, the experimental data showed that the body size measurement results in standard postures presented high stability and consistency, while the results in non-standard postures fluctuated considerably, which significantly affected the accuracy and stability. The experiment showed that the ratio of standard postures to non-standard postures was 1:3. Finally, based on joint point vectors eigenvalues, the regression models were applied to adjust body length, body height, body width and abdominal girth in non-standard postures. The linear regression and nonlinear regression methods such as BP regression and SVR support vector regression were used for comparison. The experimental results indicated that various regression methods can significantly improve the accuracy of automatic measurement by correcting the pig's body size measurement results in non-standard postures. Therefore, it is essential to classify and adjust the livestock point cloud postures to improve the accuracy of three-dimensional measurement.

1. Introduction

Accurately measuring pig body size can facilitate body condition scoring and pig's weight estimation, and also provide guidance to the growth and breeding of pigs, thus assisting pig farm owners in managing livestock more effectively and making decisions more efficiently. Currently, body size parameters of pigs are mainly measured manually, and at least two skilled stockmen are needed to obtain the body size data for each individual pig within 5–6 min after the pigs are driven in the measurement area (Chen et al., 2020). During the whole measuring process, the human-pig contact can easily cause stress for pigs (Statham et al., 2020; Yu et al., 2021). Therefore, pigs will often move impatiently, resulting in frequent changes of measurement postures and observation positions. Another problem is human fatigue in the time-consuming measurement process. All of these factors often lead to the inaccuracy of manual measurement (Nir et al., 2018; Wang et al., 2017; Xue et al., 2019) which is not adaptive to the large-scale livestock industry due to the nonstandard and subjective results. To solve these problems, there is an urgent need to adopt a more objective, standard, and non-contact method to conduct quick and accurate body size measurement of pigs.

Known by its non-contact features, computer vision has become one of the most promising solutions in intelligent livestock breeding and farming industry. Livestock posture and behavior changes recognition can assist the early detection of problems concerning animal health and welfare (Matthews et al., 2016; Spoliansky et al., 2016; Wang et al.,

* Corresponding author.

https://doi.org/10.1016/j.compag.2022.107135
Received 4 August 2021; Received in revised form 5 June 2022; Accepted 9 June 2022
Available online 17 June 2022
0168-1699/© 2022 Elsevier B.V. All rights reserved.

2020; Kim et al., 2020). Information about livestock body size measurement, weight estimation and body condition scoring can be obtained to record the individual body shape and body condition, so as to fulfill the automatic and accurate assessment of fine feeding, breeder screening (Hansen et al., 2018; Hemsworth, 2018; Rodríguez Alvarez et al., 2018; Zhang et al., 2021), breeding and reproducing. Relevant visual technologies include two-dimensional image technology and three-dimensional depth image technology. Video of the livestock and their image data are obtained by using a 2D camera, and the image processing has been applied to conduct the research mentioned above, with many research results accomplished (Jun et al., 2018; Riekert et al., 2020; Riekert et al., 2021). However, it is difficult to separate images from a complicated background due to the absence of one dimension information in two-dimensional images (Nir et al., 2018; Yu et al., 2021). Also, the system calibration is affected by the distance between livestock and camera. In addition, the measurement accuracy is influenced by illuminating conditions. As the consumer-grade 3D acquisition device develops rapidly, inexpensive and portable 3D collecting devices have been widely applied in the field of modern agriculture, for instance, Le Cozler et al. (Le Cozler et al., 2019a; Xavier et al., 2022) used Morpho3D to scan the entire cow in 3D images. By comparing the results between manual measurement and scanner measurement, they concluded that the dairy herd could be managed based on animal volume and surface area in the future, in complement to other scanner measurements such as usual morphological traits and body condition score. Ruchay et al. (Ruchay et al., 2020) utilized the depth camera KinectV2 to perform non-rigid 3D reconstruction and calculated the body size of the reconstructed model. Zhang et al. (Zhang et al., 2021) employed a convolutional neural network (CNN) with multiple output regression to estimate the weight and body size of pigs. Si et al. (Si et al., 2019) used KinectV2 to obtain the video data of the pig body, and proposed a posture detection algorithm for pig body, which improved the image utilization rate and the efficiency of body size measurement. Yin et al. (Shuai et al., 2020; Yin et al., 2019) collected point clouds of freely walking pigs, making it possible to accurately determine body size and other data. Pezzuolo et al. (Pezzuolo et al., 2018) developed linear and nonlinear models and applied them to Kinect and manual measurement data. Kongsro (Kongsro, 2014) estimated the weight of pigs through infrared depth images, and Le Cozler et al. (Le Cozler et al., 2019b) also determined body weight of cows thanks to 3D images with their device. The traditional weight scale can get more accurate weight, but the contactless 3D device may obtain more information. The weight and volume proportion of different parts of a pig such as its head, limbs, and rump are not easily measured through weight scale, and three-dimensional point clouds can assist in the calculation of these parameters. ASUS Xtion Pro (Fischer et al., 2015; Kuzuhara et al., 2015; Wang et al., 2018) are going into the research field of modern husbandry digitalization, extensively employing intelligent monitoring and measurement of pigs, cows and sheep.

There are mainly two methods of acquiring 3D data: locomotion and immobilization (Wang et al., 2018), either of which is completed by instantaneously capturing the state of free movement of livestock. Accordingly, images of a variety of livestock postures can be obtained, for instance, lowering head, turning head, raising head, walking and running, bending knees (not standing), lying on the ground, among others. However, in body size measurement, the animal needs to stand in a standard posture (Li et al., 2015): its head looks ahead horizontally, and its dorsal line between the starting point and the ending point presents a straight line, also its four hooves form a rectangle. Actually, it is quite difficult to collect the data of standard measurement postures due to the animal's habits of moving around and the external environment. The non-standard measurement postures will increase calculation error, and thus the application of 3D automatic body size measurement system is still limited (Frondelius et al., 2015; Nir et al., 2018; Yu et al., 2021).

In this paper, we propose a method to quantify point cloud-based pig postures. The pig point cloud skeleton is extracted by using L_1– Median skeleton extraction algorithm, and 22 joint points are evenly obtained from the pig's skeleton. The joint point vector eigenvalue sets are calculated from the joint point vector angles respectively with planes XOZ, XOY, YOZ. Then those eigenvalue sets are used to classify standard postures and non-standard postures through Bagging-SVM algorithm. In the experiments based on 207 groups of point clouds collected from 25 growing pigs, comparisons were made between the automatic classification results and the manual classification results based on standard postures and non-standard postures, and the body size measurement accuracy affected by standard postures and non-stand postures was analyzed. Three regression models were established and tested to adjust the results of pig's body size in non-standard postures. The effects of three models were evaluated by comparing the MSE (Mean Square Error), MAE (Mean Absolute Error), RMSE (Root Mean Square Error) and R^2.

2. Materials and methods

2.1. Data acquisition

In our experiment, all procedures were approved by the laboratory Animal Ethics Committee of South China Agricultural University (reference number 2020G008). To effectively compare different parameters of body size measurement for various pig postures, we proposed a data acquisition plan, adopting a walkway featured by a loop channel with a zig-zag walkway in a pig farm, which was temporarily set up to collect data, as shown in Figs. 1-2. The target pigs moved forward along the walkway, and we repeatedly acquired a pig's point clouds to ensure that several groups of point clouds could be obtained from a same pig in the same data acquisition area. The data acquisition experiment was completed in Jingjing Food Company, Guangdong Wens Foodstuff Co., Ltd. in Heyuan City, Guangdong Province from June 3 to June 5, 2020. After manual measurement, each target pig entered the zig-zag walkway and walked repeatedly at least three times, so that the data could be collected repeatedly in accordance with its state of cooperation. Three KinectV2 cameras were fixed in the best shooting area (including top view, left view and right view), and the distance between the target pig and the cameras was 1.2 m. The iron railings were used to separate the pig from the data acquisition devices. When the target pigs walked through the best acquisition area, the devices automatically detected them and synchronously collected the point cloud data in three directions, sending the data to the master controller. The target pigs' breed was the landrace pig, with their weight ranging from 80 kg to 150 kg. The number of target pigs was 25, and 221 groups of point cloud data were collected after repetitive data acquisition based on the actual condition of each target pig. Subtracting the registration failure data due to the pigs' hit on the railings or the partly missing data (involving the



Fig. 1. Zig-zag walkway (Loop channel 1).



Fig. 2. Zig-zag walkway (Loop channel 2).

target pigs' legs or rumps), 207 groups of point cloud data, complete and valid, were obtained.

The loop channel with a zig-zag walkway acquires two types of data: the target pig's individual identification data read from the electronic pig ear tag using the RFID card reader at the entrance; its instantaneous local point cloud data captured by three depth cameras simultaneously triggered when the pig approaches the best shooting area. With their respective conditions taken into consideration, each target pig walks through the walkway at least 3 times or at most 12 times for point cloud acquisition to select the standard postures and non-standard postures.

2.2. Defining standard measurement postures of pigs

The posture required for manually measuring livestock body size mainly refers to the animals standing naturally with their heads looking forward, the dorsal line from the head to the tail being a straight line, and their limbs standing in a rectangular shape (Frondelius et al., 2015; Nir et al., 2018; Yu et al., 2021). However, the posture of point clouds captured instantly is quite different when pigs are walking freely along the measurement walkway. Pigs may bow their heads slightly or dramatically, and twist their body to the left and right. Sometimes pigs are running, bending their knees or lying prone on the ground. The standard measurement posture defined in this paper is distinguished from top view, side view and leg posture. This posture is described as the standard standing posture: the straight body line is needed in the top view projection, and the head looks forward in the side view projection, also the leg projection allows a little stride. The other postures are defined as non-standard postures. In the process of obtaining 3D point clouds, the pig is walking freely, so it is difficult to obtain the standard posture.

2.3. Identification of standard postures of pigs

Identification of standard postures of pigs based on human judgments can be conducted by detecting the point clouds from top view, side view and pig legs projection. Top view point clouds mainly detect the degrees of body tilt or body twist. Side view point clouds determine whether the pig is standing and to what extent the pig's head lowers. The leg point cloud projection shows whether the pig has a big step posture or not.

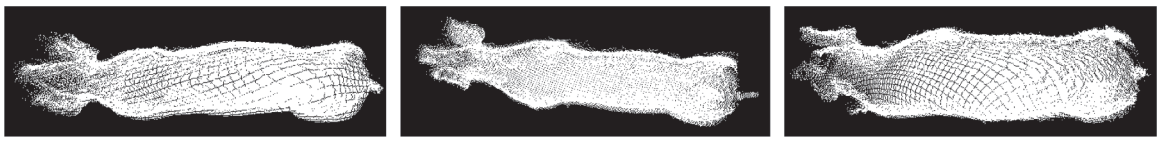
Top view point clouds present a pig's back contour, and this paper summarizes three types of pig postures based on dorsal configuration: a straight line posture (as shown in Fig. 3), a L-shape posture (as shown in Fig. 4), and a C-shape posture (as shown in Fig. 5). In Fig. 3 (a), the pig posture, which is parallel to the railings with its head and tail presenting a straight line, is a standard posture for top view point clouds. The pig posture is tilt to the railings, however, its head and its tail approximate a straight line (as shown in Fig. 3 (b)). This posture can be quickly rotated back to the standard posture. Fig. 3 (c) shows the pig posture with its head slightly turning to left or to right, but it can also be classified as a standard posture.

If the pig's head tilt makes a L-shape posture with its body, this is defined as a non-standard posture (as shown in Fig. 4). For the L-shape posture, the pig's trunk is straight, but its head tilts to one side, which may cause inaccuracy of body length and body width in body size measurements. Fig. 4 shows the L-shape posture in which the pig's head tilts to different directions and in varying degrees. Another C-shape posture (as shown in Fig. 5) is that the pig's body bends greatly, and its head and its rump bend to the same side, presenting a C posture. This is a non-standard posture that can lead to inaccuracy of body length and body width in body size measurements.

The point clouds of a pig from left side view or right side view can help to observe the pig's moving state and whether it is lowering its head. The postures of the pig's lowering head or striding decrease the accuracy of body length, body height and abdominal girth in pig body size measurements. A cloud point posture from side view featured by the pig's looking ahead horizontally is a standard posture, in which its head is straight and forward, and its four hooves basically form a rectangular (as shown in Fig. 6 (a)); the pig's head is straight and forward, but its forelegs are obviously in the position of stepping forward, and this may affect the accuracy of body height measurement (as shown in Fig. 6 (b)); if the pig's forelegs are slightly in the position of stepping forward, this is basically a point cloud standard posture from side view (as shown in Fig. 6 (c)).

The side view point cloud postures featured by lowering head are shown in Fig. 7. When the pig slightly lowers its head, the accuracy of body length measurement can be affected, so it is defined as a non-standard posture of pigs (as shown in Fig. 7 (a)); when the pig obviously lowers its head, with its head being close to the ground and its four hooves taking a wide stance, the boundaries of body length, body height, and abdominal girth can be significantly affected, so it is also defined as a non-standard posture of pigs (as shown in Fig. 7 (b), (c)).

Currently, no specific standards or regulations for pig body size measurement are available as all standard postures of body measurements are verbal descriptions. Therefore, point cloud standard postures for pig body size measurement should be quantified in a specific way. To specify the quantification of standard postures of pigs, the following points deserve special attention: ① Certainty: the feature vector of the standard posture of pigs should represent only one posture feature to avoid ambiguity; ② Geometric transformation independence: the feature vector of the standard posture of pigs does not change with different pig body shapes or coordinate positions; ③ Completeness: the feature vector of the standard posture of pigs can completely show the



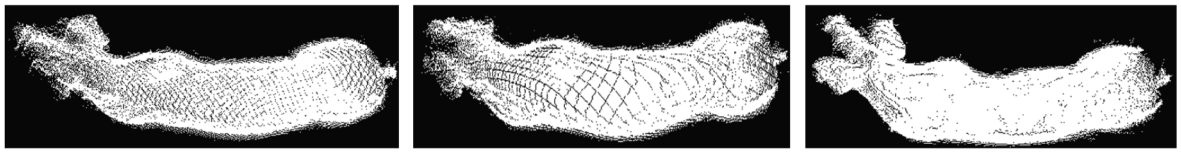
(a) Straight line posture (b) Tilt straight line posture (c) Adjustable straight line posture

Fig.3. Straight line postures based on top view point clouds.



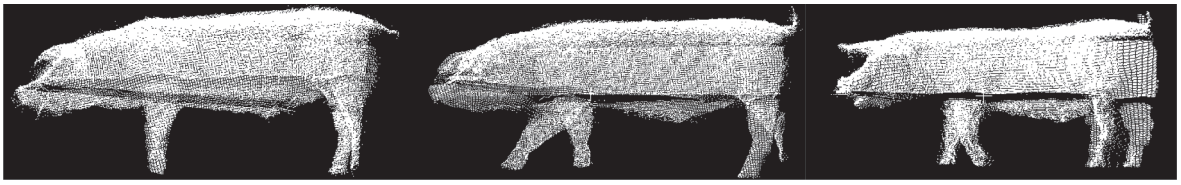
(a) Downward L-shape posture (b) Upward L-shape posture (c) Large L-shape posture

Fig. 4. L line postures based on top view point clouds.



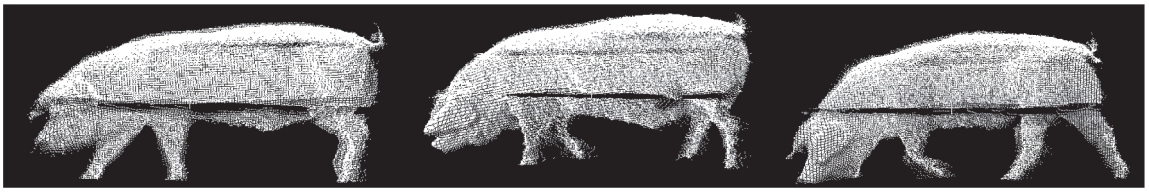
(a) Slight C-shape posture (b) Moderate C-shape posture (c) Drastic C-shape posture

Fig. 5. C line postures based on top view point clouds.



(a) Standard posture (b) Big-step posture (c) Small-step posture

Fig. 6. Point cloud postures of pigs featured by looking ahead horizontally from side view.



(a) Slightly lowering head (b) Lowering head (c) Excessively lowering head

Fig. 7. Point cloud postures featured by lowering head from side view.

information of pig postures.

2.3.1. Classifying standard postures of pigs

In our experiment, the acquired point clouds of target pigs involved all different postures. Three experts in the livestock industry classified these point clouds into standard postures and non-standard postures based on observation from different views via the 3D interactive program: Cloudcompare. Standard posture sample sets and non-standard posture sample sets for point cloud measurements were also established respectively based on the principle of expert voting. In addition, all sample sets for each target pig were divided into several subsets.

2.3.2. Defining posture features of pigs

The feature vector of pig postures is defined as eigenvalues set of the vector between pig's skeleton joint. Unlike the human skeleton with 25 bone points that have been both clearly discriminated and definitely defined, it is hard to specifically distinguish a pig's bone points due to its round body shape. However, a pig's point cloud skeleton can depict its body shape and provide the topological information of the skeleton. Different geometric structures of a pig skeleton model (such as the relative positions of skeletal nodes and the difference between various angles) can reflect various postures. Therefore, feature extraction from the skeleton point data can effectively identify standard or non-standard postures.

We extracted the point cloud skeleton of pigs to make point cloud convergence by using the L_{1-} Median skeleton extraction algorithm (Huang et al., 2013), a method which plays a vital role in all concentration fixed point problems and has been verified in many experiments in recent years due to its resistance against the interference of noise and outlier. This algorithm can be described as follows: there is an input point set $Q = \left\{q_j\right\}, j \in J \subset \Omega^3$, a sampled point set $X = \{x_i\}, i \in I \subset \Omega^3$, and a chain of skeletal points can be obtained using the optimal formula (1):

$$\underset{X}{argmin} \sum_{i \in I} \sum_{j \in J} \left\| x_i - q_j \right\| \theta\left(\left\| x_i - q_j \right\| \right) + R(X) \tag{1}$$

$$R(X) = \sum_{i \in I} \gamma_i \sum_{i' \in I \setminus \{i\}} \frac{\theta(\|x_i - x_{i'}\|)}{\sigma_i \|x_i - x_{i'}\|} \tag{2}$$

$$\theta(r) = exp\left[-4(r/h)^2\right] \tag{3}$$

In formula (1), the first part determines the shrinking skeletal points in local L_{1-} Median. Specifically, targeted at sampling points, neighborhood point gravitational effect is added to the input point set and transferred to local median value. The second part is the regularized term, making repulsive force based on the neighborhood points in the sampling point set to avoid shrinking overly. In formula (2), γ_i is the parameters of equilibrium gravitational force and repulsive force. $\theta(r)$ is a Gaussian weight function, and it can be found in formula (3) that under the fixed neighborhood radius, the weight contribution decreases as the distance from the sampling point increases, thus median filtering is applied. σ_i is distribution measure: the closer σ_i is to 1, the point is more likely to be located on the middle line of a skeleton; the closer σ_i is to 0, the point is more likely to be located on a skeleton branch. Point clouds are segmented into different regions based on size, shape and point set density, and the initial neighborhood is specifically determined according to self-adaptive regions. Generally, the initial neighborhood radius is computed based on the region size and the number of source points h_0, $h_0 = 3 \times d_b / \sqrt[3]{J}$, where d_b is the diagonal line length of point cloud bounding box in this region. J refers to the number of points in the source point cloud set in this region, with its convergence result being a skeleton point set.

After the L_{1-} Median skeleton extraction is conducted, a pig skeleton can be divided into six parts: head, body, two front legs and two hind legs. As no explicit bone data of pigs is available, the number of skeleton branches and joint points are not consistent in skeleton extraction. Thus, data normalization should be conducted to get unified scale traits for different skeleton sequences.

22 points were evenly obtained from all parts of the pig skeleton. 3 points were taken from the head skeleton, 7 points were taken from the body part, and 3 points were taken from each leg (4 legs, 12 points) as illustrated in Fig. 8.

Three joint points are evenly selected from the skeleton of a pig's head and its four legs. Seven joint points are evenly selected from the skeleton of a pig's body. A coordinate system with $g_i = \{x_i, y_i, z_i\}$ as the ith joint point is set, and the complete pig point clouds involve $G = \{g_1, g_2, \cdots, g_k\}, K = 22$, that is, 22 joint points are connected in proper order from the pig's tail root to its head, from the pig's leg to its abdomen, constructing a vector $v_{i,i+1}$, which is formulated as (4):

$$v_{i,i+1} = \{g_{i+1} - g_i | i = 1, 2, \cdots, K-1\} \tag{4}$$

Joint point vectors respectively form vector angles θ, α,β with planes *XOZ*, *XOY*, *YOZ*, in other words, they are the angular range of joint point vectors in various plane directions. The contribution degrees vary with each individual joint point vector in the posture expression. Different weights are given to the feature vector of different joint points according to the contribution degree. As for weights selection, we consider that the leg joint points have little impact on the accuracy, and the major influencing factor is on the head and trunk center joint points. After manual primary selection, the weights are optimized through experiments. Therefore, accurate vector angle eigenvalues of difference degree between joint points can be obtained by using weight operation:

$$E_\theta = \sum_{i=1}^{K-1} \omega_i \theta_{i,i+1} \tag{5}$$

$$E_\alpha = \sum_{i=1}^{K-1} \omega_i \alpha_{i,i+1} \tag{6}$$

$$E_\beta = \sum_{i=1}^{K-1} \omega_i \beta_{i,i+1} \tag{7}$$

Therefore, in a point cloud pig skeleton, the 22 joint points vector set is $V = \{v_{1,2}, v_{2,3}, \cdots, v_{21,22}\}$; the jointpoint vector eigenvalue set is $E = \{E_\theta, E_\alpha, E_\beta\}$, which are defined as the quantitative index of characteristic measurement for standard postures of pigs. $\{E_\theta, E_\alpha, E_\beta\}$ as posture quantitative eigenvector is the input of classifier for identifying pig's postures.

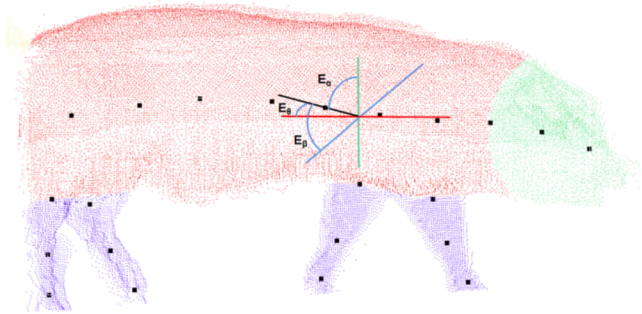


Fig. 8. 22 points of pig skeleton.

2.3.3. Bagging-SVM posture classifier

Bagging algorithm is an algorithm based on bootstrap sampling, whose core operating principle is sampling with replacement. In the sampling process, samples are randomly taken from the initial data set, and put into the new data set for further sampling. In this research project, samples of standard postures from the same pig have a limited number, so replacement sampling can ensure that the samples appear repeatedly in the sampling subsets. In T datasets, each sampling subsets respectively are designated to the base classifiers for training; each dataset of sampling generates a weak classifier $\phi(x, D_k)$, and T weak classifiers are integrated as a strong classifier. In the test phase, the classification results made by the strong classifier are the simple voting results made by the T weak classifiers, which means the category with majority of voting is used as the category of test sample (as shown in Fig. 9,).

In each group of point cloud pig skeleton extraction with 22 joint points, the vector set is $= \{v_{1,2}, v_{2,3}, \cdots, v_{21,22}\}$; the eigenvalue set of the joint points is $E = \{E_\theta, E_\alpha, E_\beta\}$, which is a Bagging-SVM algorithm-based input feature set. After T rounds of training by using the base classifier algorithm and support vector machine, a model of pig point clouds is built to discriminate standard postures of pigs from non-standard ones. As the sampling subsets in the Bagging-SVM algorithm are not identical, the base classifiers trained by each sampling subset are different. Meanwhile, the replacement sampling ensures that the same sample appears multiple times in different sampling subsets, which will avoid inadequate training effect caused by using only a small part of training data in each base classifier. Accordingly, the performance of an integrated algorithm is enhanced.

2.4. Regression prediction of body size

2.4.1. Predictor and predictand data

The pig point clouds in non-standard postures will reduce the accuracy of body size measurement. Adjusting the non-standard posture point clouds to the standard posture for measurement is a solution, which will get a better performance on body size measurement accuracy. In this paper, the correcting body size measurement results by regression model is considered to reduce the body size measurement error.

Since the pig limbs have relatively little influence on posture classification, 9 vector eigenvalues composed by 10 joint points of head and body parts are selected as predictors in regression prediction. And automatic measurement of body length is also a predictor. Using the linear regression and nonlinear regression methods, the 9 eigenvalues of related joint point and body size measurement in standard postures are

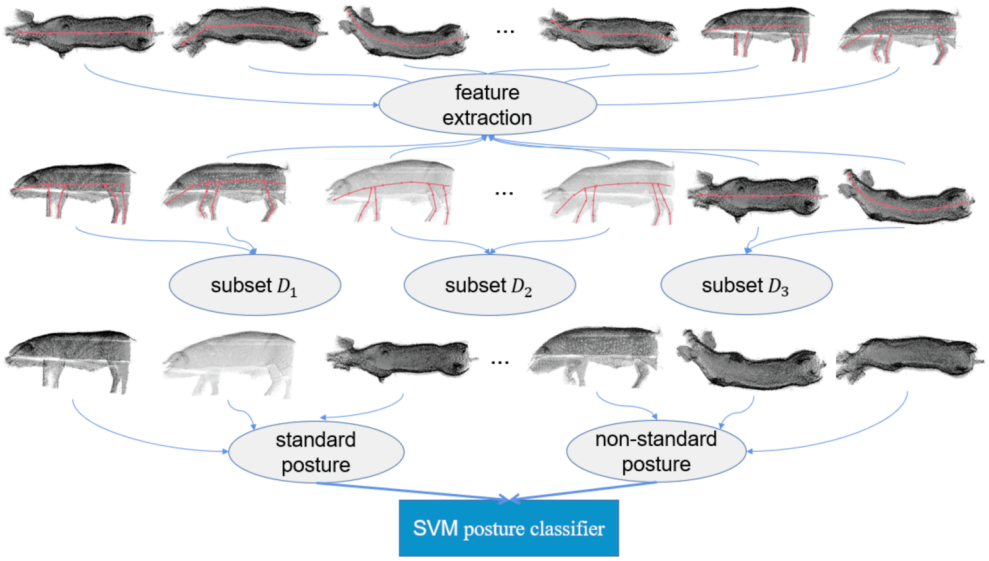


Fig. 9. Schematic of Bagging-SVM posture classifier.

analyzed, and the measurement results in non-standard postures are predicted.

2.4.2. Linear regression

Among the multiple variables, the predicted body length is represented by Å·; the independent variables $x_1, x_2, \cdots, x_n$ are the 9 joint point vector eigenvalue set of a pig's head and body $\{E_1, E_2 \cdots E_9\}$; β_0 is the body size automatic measurement, and the linear regression equation is as follows:

$$\mathring{A}\cdot = \beta_0 + \beta_1 x_1 + \beta_2 x_2 + \cdots + \beta_n x_n + \varepsilon \tag{8}$$

2.4.3. Nonlinear regression

In this paper, two nonlinear regression methods are adopted: SVR support vector regression, BP neural network regression. In those regression analyses, the 9 joint point vector eigenvalue set and automatic measurement of body length are predictor variables.

3. Results and analyses

3.1. Comparison of results and data analyses of different postures

207 groups of pig point clouds were manually classified by observing the point clouds from top view and side view; the percentages of different type distributions of pig postures are shown in Tab.1. There are three types of postures based on top view point clouds: straight line posture (accounting for 68.59%), L-shape posture (accounting for 10.14%), and C-shape posture (accounting for 21.26%). That is, two-thirds of the pig's point clouds obtained were comparatively straight from top view; one-third of the pig's point clouds presented twisted postures, which were non-standard postures. By contrast, only 32.85% of the target pigs could keep looking ahead horizontally from side view in a standard posture. In general, 51.69% of the target pigs would slightly lower their head. Furthermore, 15.46% of the target pigs bowed their head very close to the ground, which is attributed to pigs' poor eyesight and their habitual way of sensing the environment via olfaction. Many pig postures featured by their looking down movement have been captured as pigs tend to lower their head and sniff around. Obvious inaccuracy of body length measurement would be caused if the target pig excessively bowed its head, with the maximum deviation being 12 cm in manual measurement of body length in our experiment. Besides, the accuracy of body height measurement was affected, with the error being 2–4 cm in body height. In the manual classification of pig leg postures, a perfect rectangular presented by a pig's four hooves is very rare, because this posture requires that a target pig should happen to stop walking and keep standing in the walkway for measurement. However, in actual situations, most target pigs walk through the walkway quickly or run through it, with their legs in the state of striding forward. By manual statistics, a target pig's four hooves make a rectangular region if its two legs (front legs; hind legs) are basically in a straight line. Even so, only 23 groups of point cloud data were obtained with a rectangle presented by four hooves, merely accounting for 11.11% among 207 groups of point cloud data. A posture featured by taking a step will affect the accuracy of body height, causing errors in abdominal girth and thoracic circumference. As shown in Table 1, standard postures, which strictly met the standards set from top view, side view, and leg posture, accounted for less than 10% in the actual point cloud data. Therefore, lower discrimination standards were followed in automatic body size measurements: standard postures also included postures featured by the pig's taking a small step or slightly lowering its head from side view. Automatic discrimination results are shown in Table 2.

Table 2 lists the results of manual posture classification, SVM automatic posture classification without leg joint points, and SVM automatic posture classification with leg joint points. Manual posture classification adopts a majority decision principle to obtain the cumulative voting results independently made by three experts from top view, side view, and leg posture. The joint point vector eigenvalue sets were used to classify the postures by using Bagging-SVM automatically. Two different results were obtained according to the joint point vector eigenvalue set containing the pig leg joint points and without containing the pig leg joint points. Only 52 pig postures in manual classification were classified as standard postures, while 49 pig postures were classified automatically without leg joint points information. And there were 6 non-standard postures classified as standard postures. The main reasons for the difference between manual posture classification and automatic posture classification are as follows. Firstly, there were subjective differences in manual discrimination, as there were only slight differences between mild C type, L type and straight type postures, and subtle differences between postures of slightly lowering heads and postures of looking ahead horizontally. Second, some pig bodies presented a straight line that was only insignificantly skewed by their heads, which is regarded as a non-standard posture in the human eye. This would be automatically classified as a standard posture because the calculation of its eigenvector is very close to that of a straight line posture.

Figs. 10 and 11 respectively show the joint point vector eigenvalue

Table 1
Results of manual classification of pig point clouds.

Type	Manual classification of pig postures from top view			Manual classification of pig postures from side view			Manual classification of pig leg posture	
	Straight line posture	L line posture	C line posture	Looking ahead horizontally	Slightly lowering head	Excessively lowering head	Rectangle presented by four hooves	Pig legs taking a step
Number	142	21	44	68	107	32	23	184
Percentage	68.6%	10.1%	21.3%	32.8%	51.7%	15.5%	11.1%	88.9%

Table 2
Discrimination results of point clouds of pig postures.

Manual classification of postures		Automatic classification of postures (without pig legs)		Automatic classification of postures (with pig legs)	
		Standard postures	Non-standard postures	Standard postures	Non-standard postures
Standard postures	52	49	6	48	7
Non-standard postures	155	3	149	5	147

sets with or without the point clouds of pig legs calculated. Obviously, without calculating the pig leg point clouds, the discrimination of the joint point vector eigenvalue set increases significantly, which can clearly distinguish between standard postures and non-standard postures. The reason is that the point clouds of pig legs were collected when pigs were walking. Vector eigenvalue of pig legs would increase the fundamental value of each component and reduce the discrimination. E_θ showed no apparent differentiation, however, E_α was different in top view and E_β presented significant discrimination in side view.

3.2. Contrastive analysis of body size data

Pig body size measurement method was provided according to references (Yin et al., 2019). The body length, body height, body width, and abdominal girth of the classified postures were calculated, as illustrated in Figs. 12-15. Four groups of point cloud data were obtained from target pig No. 15. For the rest of target pigs, point cloud data groups ranged between six and ten groups. Figs. 12-15 compare the results between the automatic measurements and manual measurements of body length, body height, body width, and abdominal girth in both standard and non-standard postures of each target pig. The yellow and blue bars are automatic measurement results in standard and non-standard postures, respectively; the red asterisks are the results of manual measurement and red plus signs are outliers. Fig. 12 illustrates that the blue bar fluctuates significantly, which means the body length measurement results of the same pig in a non-standard posture varies wildly. And No. 3, No. 6 and No.9 pigs also show outliers which deviated significantly from the median value. In non-standard postures, the pig's neck stretch may naturally bring considerable differences in body length measurement, if it lowered or turned around its head. In most cases, the fluctuations of body length measurement results in non-standard postures were more significant than those in standard postures, as can be seen from Figs. 12-15. The automatic body length results in standard postures presented high consistency, and their median values were much closer to those of manual measurement. The same results were shown in body height, body width and abdominal girth measurements. Fig. 15 shows that the fluctuation amplitude of abdominal girth in both standard and non-standard postures was relatively larger than that for measurement of body height and body width. Due to the incomplete data of pig abdomen, the accuracy of automatic measurement of abdominal girth was relatively low. At the same time, when the target pig's body tilted or twisted, the acquired shape of the abdominal girth slice was not close to the circle, and the polar coordinate transformation algorithm based on circle fitting would lead to more errors. Comparisons of automatic measurement results were made between standard postures and non-standard postures through the overall analysis of body length, body height, body width, and abdominal girth in Figs. 12-15. It is obvious that the body length and abdominal girth measurement results fluctuated significantly, and the measurement results of body height and

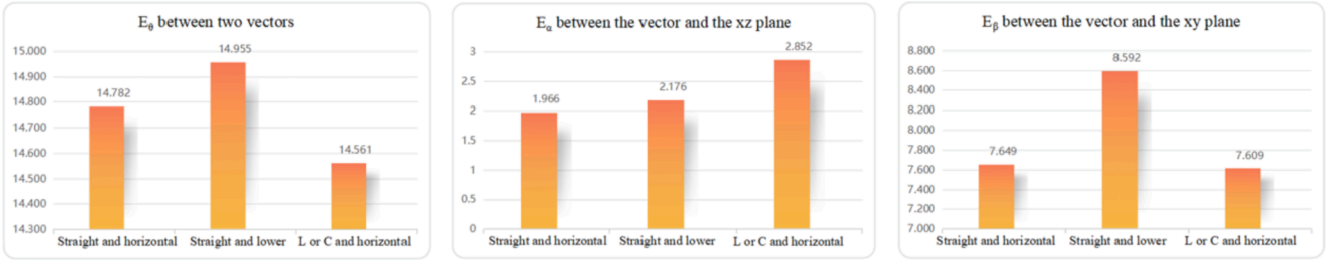


Fig. 10. Joint point vector eigenvalue set with the point clouds of pig legs calculated.

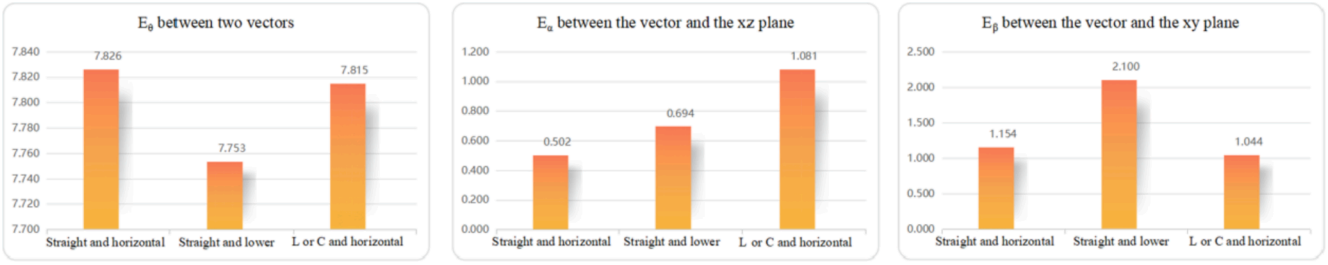


Fig. 11. Joint point vector eigenvalue set without the point clouds of pig legs calculated.

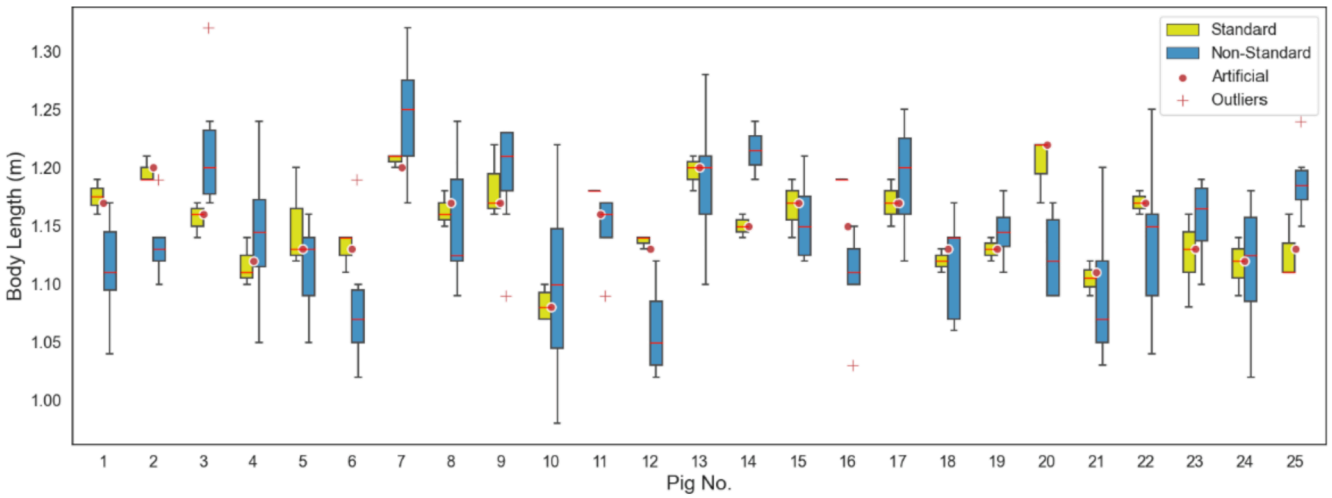


Fig. 12. Automatic measurement and manual measurement of body length in standard and non-standard postures.

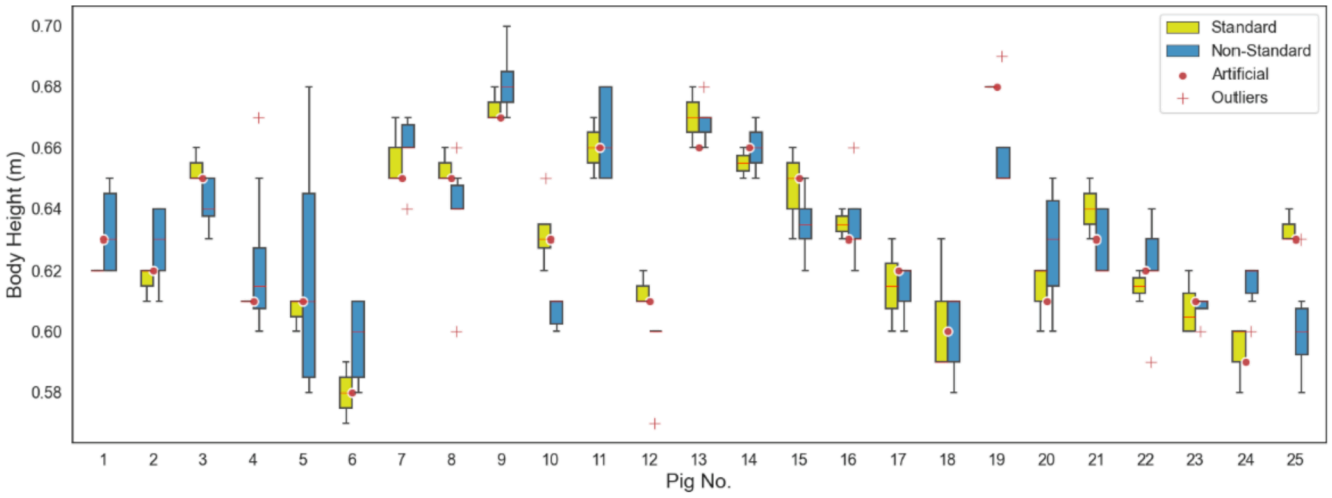


Fig. 13. Automatic measurement and manual measurement of body height in standard and non-standard postures.

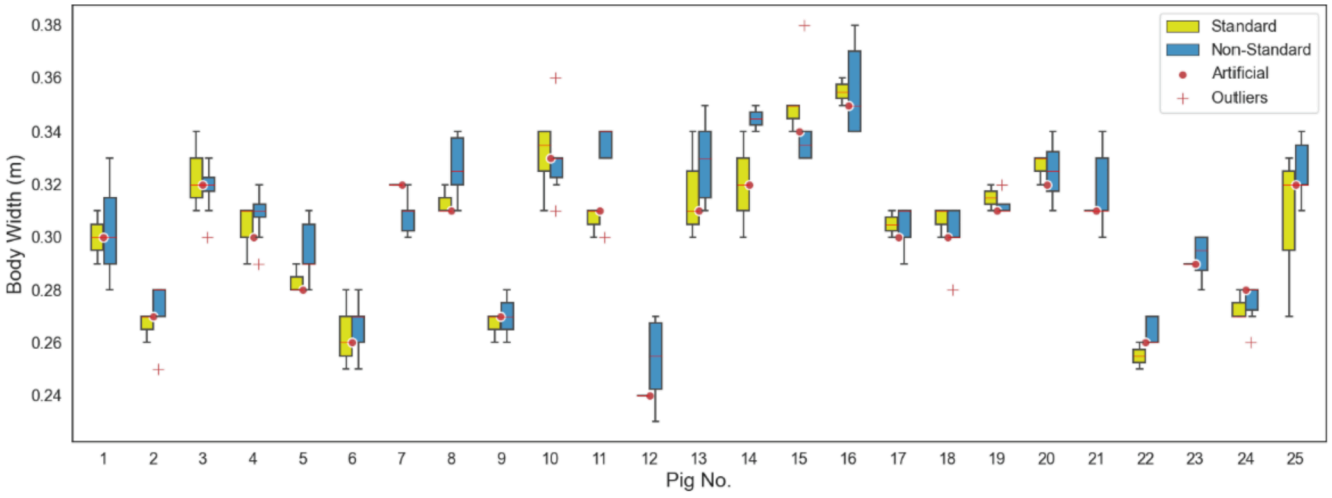


Fig. 14. Automatic measurement and manual measurement of body width in standard and non-standard postures.

body width were relatively consistent. The measurements of body length and abdominal girth are calculated by the curve length along the body surface, and the nonrigid deformation has a great influence on those results. Body height and body width are calculated in linear distance, and the influence of nonrigid deformation on them is relatively insignificant. Generally, two points can be illustrated: (1) The body size

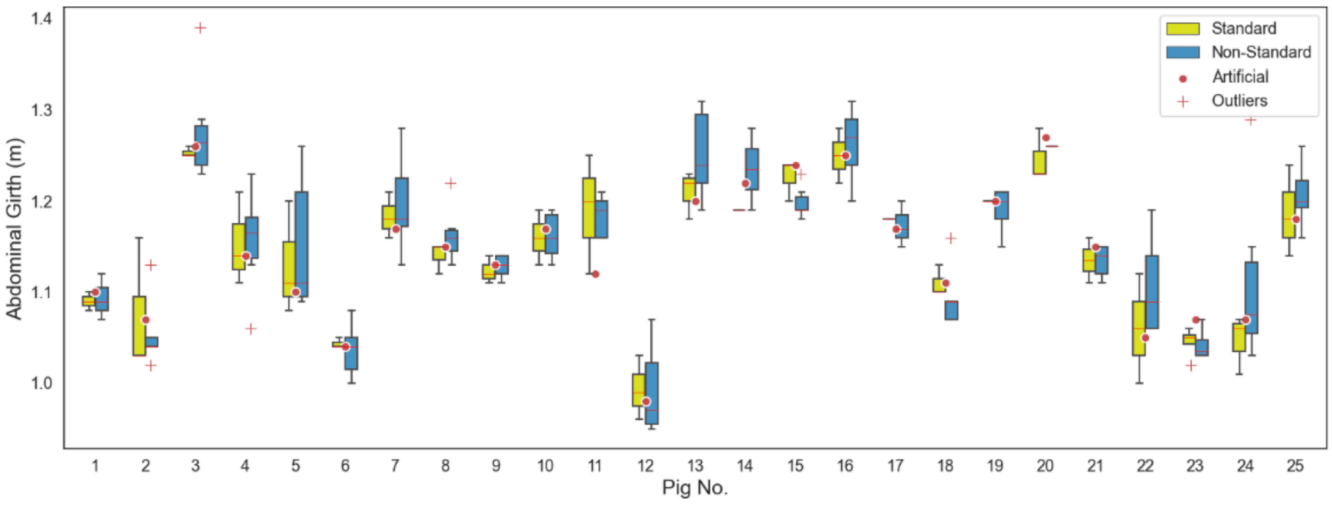


Fig. 15. Automatic measurement and manual measurement of abdominal girth in standard and non-standard postures.

automatic measurement results were more stable and robust in standard postures. (2) When the same pig passed through the walkway for data acquisition, different postures would have an enormous impact on the measurement data. The accuracy and the stability of the measurement results in standard postures were significantly higher than those in non-standard postures. Meanwhile, when pigs twisted their body, it was difficult to fit the abdominal girth slice with the circle, so the algorithm for repairing missing data of abdominal girth needs to be further improved, and the stability of the algorithm is expected to be enhanced.

3.3. Comparisons and analyses of linear and nonlinear regression

In this experiment, 207 groups of point cloud data collected from 25 target pigs were selected as the specific research object, including 52 groups of point cloud data in standard postures and 155 groups of point cloud data in non-standard postures. Three models for predicting the pig body size were established, including multiple linear regression model, SVR regression model and BP regression model, with 52 groups of point cloud data in standard postures and 92 groups of point cloud data in non-standard postures in the training set, and the remaining 63 groups of point cloud data in non-standard postures functioned as the test set.

3.3.1. Comparing prediction results of body height and body width in regression models

Figs. 16-17 show the comparisons of prediction results of body height and body width in three regression models. The red line is the average length of pig body automatically measured in standard postures. The pink line is the prediction results of linear regression. The green and blue lines are the prediction results of the BP, SVR model regression, respectively. These prediction results satisfy the requirements of standard postures, and the prediction results obtained by using a non-linear regression method were better than those by a linear regression method. The main reason may be that body height and body width are measured in linear distance. The skeleton extracted from pig point clouds does not cause significant differences in body height and body width measurement results between standard postures and non-standard postures.

3.3.2. Comparing prediction results of abdominal girth in regression models

In Fig. 18, the predicted values of various regression models are quite different from the results in standard postures, although the trend of these three regression models is close to standard posture value, besides, it is difficult to estimate which regression model shows better effect. Two factors may be responsible for this phenomenon: the impact on the abdominal girth measurement differs in different non-standard postures, for example, lowering the head has little impact on the abdominal girth

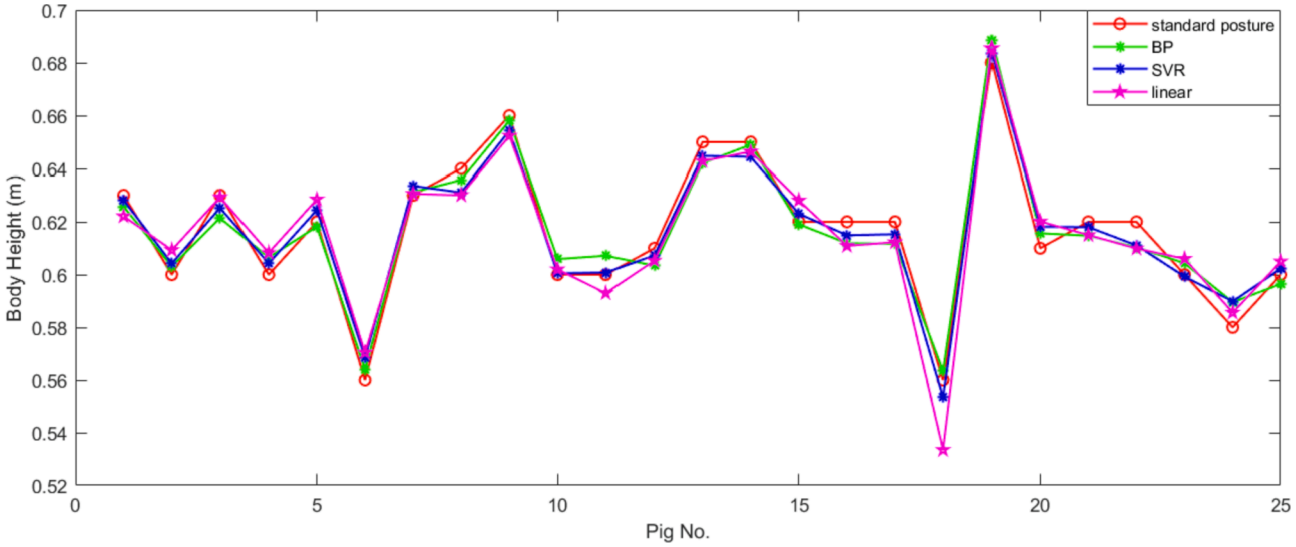


Fig. 16. Comparisons of prediction results in various regression models (body height).

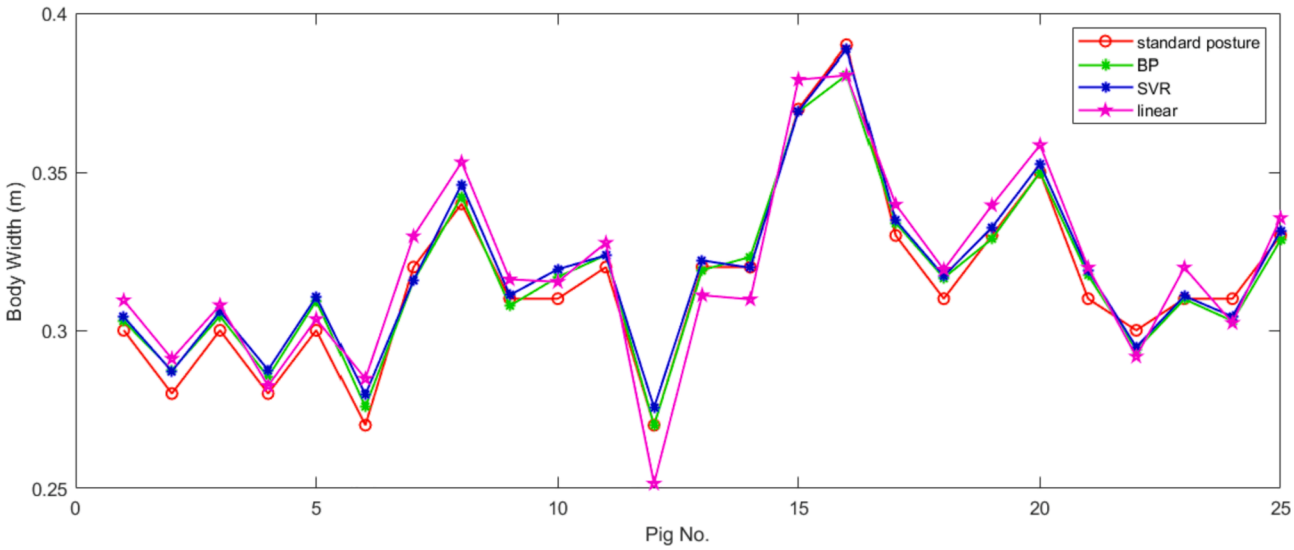


Fig. 17. Comparisons of prediction results in various regression models (body width).

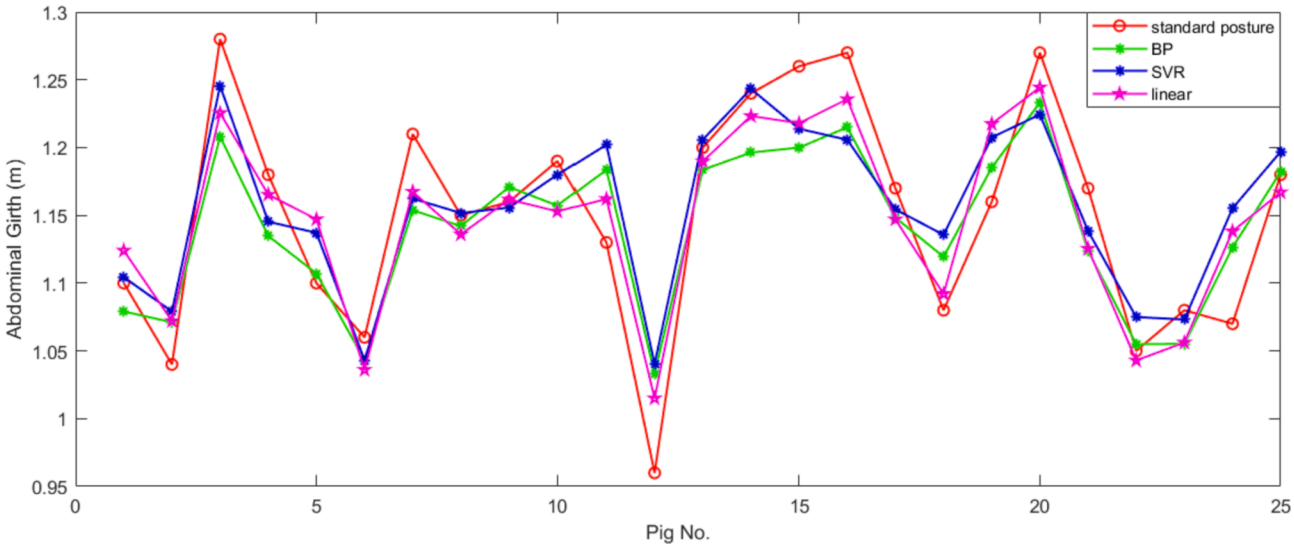


Fig. 18. Comparisons of prediction results in various regression models (abdominal girth).

measurement, but twisting the body will have significant impact, because different postures will change the position of abdominal girth slice. Therefore, it is necessary to further classify non-standard postures. Another reason is that there is a severe loss of point clouds on a pig's abdomen due to the railings in the walkway. Even if the point clouds on the pig's abdomen are completed by using a hole repairing algorithm (Zhikun et al., 2022), the predicted values are quite different.

3.3.3. *Comparing prediction results of body length in regression models*

Fig. 19 shows the comparisons of prediction results of average body length for each pig in standard postures in various regression models. Whichever regression method is used, its adjustment trend will follow the automatic measurement result in standard postures, but the deviation value is still very large.

Table 3 is the detailed analysis of error evaluation in these three regression models. Four evaluation methods, including MSE, MAE, RMSE, and R^2 are adopted to evaluate the training effects, respectively.

The data in Table 3 specifically reflects that linear regression had a better prediction impact, while BP neural network regression was slightly inferior. The skeleton line extracted from pig point clouds reflects the non-rigid deformation trend of body length. Therefore, linear regression shows better performance. However, some outliers (like No.10 or No.21) can make the R-Squared statistic much smaller than what is appropriate to describe the overall pattern in the data. In summary, the R^2 of these three regression models were all above 82%, indicating that extracting the joint point vector to classify and adjust pig postures have desirable effects and reference significance in the actual situation. Meanwhile, the present study is of guiding significance for the development of non-contact body size measurement for livestock.

4. Discussion

The experimental results in the present study indicate that the proportion of standard postures was only 25% in the actual data acquisition of pig body size measurements. Besides, non-standard postures can create considerable uncertainty in body size measurements. Therefore, to improve the accuracy of body size measurement, we first need to improve the ratio of standard postures in data acquisition. According to the experimental data, the target pigs tend to lower their head and sniff around (Yan et al., 2019). Consequently, non-standard postures,

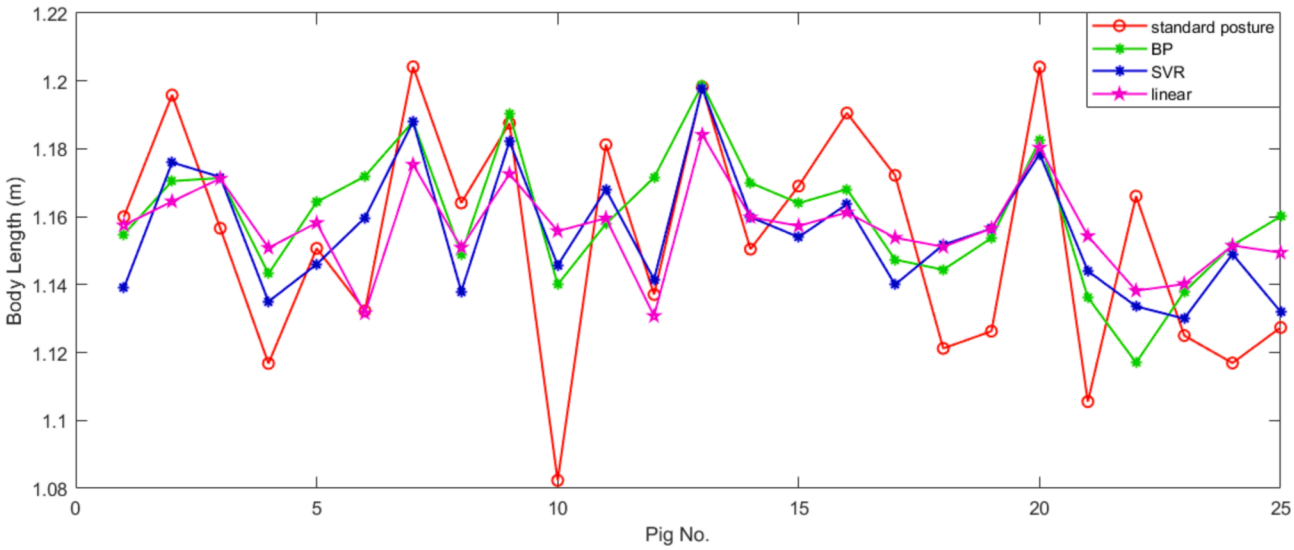


Fig. 19. Comparisons of prediction results in various regression models (body length).

Table 3
Analyses of error evaluation in various regression models Model quality was assessed with a coefficient of determination (R^2), mean absolute error (MAE), mean square error (MSE) and root mean square error (RMSE).

Algorithm	MSE	MAE	RMSE	R^2
SVR Support Vector Regression	0.00407	0.05136	0.06385	0.8289
BP Neural Network Regression	0.00434	0.05271	0.06588	0.8263
Linear Regression	0.001	0.03047	0.03373	0.8835

featured by pigs' bowing their heads, taking a step, or twisting their bodies, frequently appear during the data collection process. Accordingly, it may be feasible to properly place a feeder so that the target pig may keep looking ahead horizontally when walking through the walkway. But the difficulty lies in the position where this feeder should be mounted to ensure that the pig moves through the walkway without knocking over the devices. Another critical issue is to capture more point cloud data groups for an ideal pig posture, which will pose a new challenge to the capture timing and the data transmission. The third problem is how to adjust the point clouds of non-standard postures to make them become those of standard postures. Adjusting the body size automatic measurement results directly is a more efficient solution, for it does not require any additional restrictions to acquire data of standard postures, and it can compute the results more accurately, even for the point clouds of arbitrary postures. But the difficulty lies in how to make the adjustment in a precise way. In most of the literature about body size measurements, manual measurement data is principally adopted as the standard of accuracy, however, in actual manual measurement, each target pig will keep swinging, and its respective measurement results are possibly obtained in various postures. The fourth problem is the regression method which adjusts the body size measurement results concerning non-standard postures, but whether we can replace the measurement results concerning standard posture is not settled. The existing experiments show that linear and nonlinear regression methods can have a better adjustment effect. However, these methods require a large number of samples. In addition, whether or not the regression model parameters of different pig breeds are distinct still needs to be verified. The fifth problem is that pig postures have different effects on the measurement of body size. For example, lowering head makes body height measurement results smaller but has little impact on the body width measurement results. The C-shape posture does not affect body height measurement, but it will affect body width measurement. As the body width line becomes skewed if the pig body twists, the C-shape posture will also affect the abdominal girth measurement. Last but not least, the missing point cloud is another important factor in measurement error. At present, the classification of standard and non-standard postures alone is insufficient to comprehensively describe different postures. Considering these facts, the gold standard in body size measurements remains unknown. Further research is expected for practical solutions.

5. Conclusion

In this paper, we endeavored to classify standard postures and non-standard postures of pig point clouds by employing quantitative calculation methods. We obtained 207 groups of valid point cloud data from 25 target pigs that freely passed through the same walkway, with the maximum being 12 groups of point clouds and the minimum being three groups of point clouds from an individual target pig. Meanwhile, we presented a discriminant algorithm for standard postures of pigs based on Bagging-SVM via skeleton eigenvector extraction, distinguishing between standard postures and non-standard postures from pig point clouds obtained. The automatic discriminant algorithm distinguished 55 groups of point cloud data in standard postures and 152 groups of point cloud data in non-standard postures from 207 groups of point cloud data obtained in an experiment farm, and comparisons were made between 52 groups of standard postures and 155 groups of non-standard postures. The body size of target pigs was measured according to the posture classification results.

Based on the data of body length, body height, body width, and abdominal girth, the following conclusions can be reached: (1) The body size measurement results show relatively high stability and consistency in the point cloud calculation of standard postures, and the rank orders of stability are body width > body height > body length > abdominal girth. (2) The body size measurement results show relatively high volatility in the point cloud calculation in non-standard postures; the stability and the consistency reflected by mean, standard deviation are both significantly lower than those in the point cloud calculation of standard postures, consequently affecting the accuracy and stability of body size measurement. (3) According to the experimental data, only 25% of the postures obtained in actual measurement environment are standard postures. Therefore, it is essential to use 3D body size measurements for livestock so as to select standard postures or adjust non-standard postures. (4) Comparisons of prediction results of body size measurements in non-standard postures from this study demonstrate that both linear and nonlinear regression methods can correct the non-

standard body size measurement results to the standard posture results. Linear regression can be a better option, and the preliminary comparison test reveals a high correlation.

Declaration of Competing Interest

The authors declare that they have no known competing financial interests or personal relationships that could have appeared to influence the work reported in this paper.

Acknowledgements

The authors thank Guangdong Wens Foodstuff Co., Ltd. for providing us materials to conduct the experiment. We thank everyone who has helped us to obtain data and manually measure pigs. This project is sponsored by the National Natural Science Foundation of China [32172780], Key Area R&D Plan of Guangdong Province [2019B020219001] and by National Engineering Research Center for Breeding Swine Industry and by the Key Laboratory of Guangzhou for Intelligent Agriculture[201902010081], Key Laboratory of Smart Agricultural Technology in Tropical South China, Ministry of Agriculture and Rural Affairs, P.R. China.

References

Rodríguez Alvarez, J., Arroqui, M., Mangudo, P., Toloza, J., Jatip, D., Rodríguez, J.M., Teyseyre, A., Sanz, C., Zunino, A., Machado, C., Mateos, C., 2018. Body condition estimation on cows from depth imagesusing ConvolutionalNeuralNetworks. Comput. Electron. Agric. 155, 12–22. https://doi.org/10.1016/j.compag.2018.09.039.

Chen, H., Wang, C., Li, X., Bao, J., 2020. Effects of Long-Term gentle handling on behavioral responses production performance and meat quality of pigs. 37 (09), 18–22. https://doi.org/10.3969/j.issn.1673-5358.2020.09.004.

Fischer, A., Luginbühl, T., Delattre, L., Delouard, J., Faverdin, P., 2015. Rear shape in 3 dimensions summarized by principal component analysis is a good predictor of body condition score in holstein dairy cows. J. Dairy Sci. 98 (7), 4465–4476. https://doi.org/10.3168/jds.2014-8969.

Frondelius, L., Järvenranta, K., Koponen, T., Mononen, J., 2015. The effects of body posture and temperament on heart rate variability in dairy cows. Physiol. Behav. 139, 437–441. https://doi.org/10.1016/j.physbeh.2014.12.002.

Hansen, M.F., Smith, M.L., Smith, L.N., Abdul Jabbar, K., Forbes, D., 2018. Automated monitoring of dairy cowbody condition, mobility and weight using a single 3D video capture device. Comput. Ind. 98, 14–22. https://doi.org/10.1016/j.compind.2018.02.011.

Hemsworth, P.H., 2018. Key determinants of pig welfare: implications of animal management and housing design on livestock welfare. Animal Production. Science 58 (8), 1375. https://doi.org/10.1071/AN17897.

Huang, H., Wu, S., Cohen-Or, D., Gong, M., Zhang, H., Li, G., Chen, B., 2013. L1-Medial Skeleton of Point Cloud. ACM Trans. Graphics 35 (4), 65. https://doi.org/10.1145/2461912.2461913.

Jun, K., Kim, S.J., Ji, H.W., 2018. Estimating pig weights from images without constraint on posture and illumination. Comput. Electron. Agric. 153, 169–176.

Kim, Y., Park, D., Park, H., Kim, S., 2020. Pig datasets of livestock for deep learning to detect posture using surveillance camera. In: 2020 International Conference on Information and Communication Technology Convergence. https://doi.org/10.1109/ICTC49870.2020.9289401.

Kongsro, J., 2014. Estimation of pig weight using a Microsoft Kinect prototype imaging system. Comput. Electron. Agric. 109, 32–35. https://doi.org/10.1016/j.compag.2014.08.008.

Kuzuhara, Y., Kawamura, K., Yoshitoshi, R., Tamaki, T., Sugai, S., Ikegami, M., Kurokawa, Y., Obitsu, T., Okita, M., Sugino, T., Yasuda, T., 2015. A preliminarily study for predicting body weight and milk properties in lactating Holstein cows using a three dimensional camera system. Comput. Electron. Agric. 111, 186–193. https://doi.org/10.1016/j.compag.2014.12.020.

Le Cozler, Y., Allain, C., Caillot, A., Delouard, J.M., Delattre, L., Luginbuhl, T., Faverdin, P., 2019a. High precision scanning system for complete 3D cow body shape imaging and analyzing morphological traits. Comput. Electron. Agric. 157, 447. https://doi.org/10.1016/j.compag.2019.01.019.

Le Cozler, Y., Allain, C., Xavier, C., Depuille, L., Caillot, A., Delouard, J.M., Delattre, L., Luginbuhl, T., Faverdin, P., 2019b. Volume and surface area of Holstein dairy cows calculated from complete 3D shapes acquired using a high-precision scanning system: Interest for body weight estimation. Comput. Electron. Agric. 165, 104977. https://doi.org/10.1016/j.compag.2019.104977.

Li, Z., Mao, T., Liu, T., Teng, G., 2015. Comparison and optimization of pig mass estimation models based on machine vision. Transactions of the Chinese Society of Agricultural Engineering. 31 (2), 155–161. https://doi.org/10.3969/j.issn.1002-6819.2015.02.022.

Matthews, S.G., Miller, A.L., Clapp, J., Plötz, T., Kyriazakis, I., 2016. Early detection of health and welfare compromises through automated detection of behavioural changes in pigs. Vet. J. 217, 43–51. https://doi.org/10.1016/j.tvjl.2016.09.005.

Nir, O., Parmet, Y., Werner, D., Adin, G., Halachmi, I., 2018. 3D Computer-vision system for automatically estimating heifer height and body mass. Biosyst. Eng. 173, 4–10. https://doi.org/10.1016/j.biosystemseng.2017.11.014.

Pezzuolo, A., Guarino, M., Sartori, L., González, L.A., Marinello, F., 2018. On-barn pig weight estimation based on body measurements by a Kinect v1 depth camera. Comput. Electron. Agric. 148, 29–36.

Riekert, M., Klein, A., Adrion, F., Hoffmann, C., Gallmann, E., 2020. Automatically detecting pig position and posture by 2D camera imaging and deep learning. Comput. Electron. Agric. 174, 105391. https://doi.org/10.1016/j.compag.2020.105391.

Riekert, M., Opderbeck, S., Wild, A., Gallmann, E., 2021. Model selection for 24/7 pig position and posture detection by 2D camera imaging and deep learning. Comput. Electron. Agric. 187, 106213. https://doi.org/10.1016/j.compag.2021.106213.

Ruchay, A., Kober, V., Dorofeev, K., Kolpakov, V., Miroshnikov, S., 2020. Accurate body measurement of live cattle using three depth cameras and non-rigid 3-D shape recovery. Comput. Electron. Agric. 179, 105821. https://doi.org/10.1016/j.compag.2020.105821.

Shuai, S., Ling, Y., Shihao, L., Haojie, Z., Xuhong, T., Caixing, L., Aidong, S., Hanxing, L., 2020. Research on 3D surface reconstruction and body size measurement of pigs based on multi-view RGB-D cameras. Comput. Electron. Agric. 175, 105543. https://doi.org/10.1016/j.compag.2020.105543.

Si, Y., An, L., Liu, G., Li, B., 2019. Ideal Posture Detection and Body Size Measurement of Pig Based on Kinect. Transactions of the Chinese Society for Agricultural Machinery. 50 (1), 58–65. https://doi.org/10.6041/j.issn.1000-1298.2019.01.006.

Spoliansky, R., Edan, Y., Parmet, Y., Halachmi, I., 2016. Development of automatic body condition scoring using a low-cost 3-dimensional kinect camera. J. Dairy Sci. 99 (9), 7714–7725.

Statham, P., Hannuna, S., Jones, S., Campbell, N., Colborne, G., Browne, W., Mendl, M., 2020. Quantifying defence cascade responses as indicators of pig affect and welfare using computer vision methods. Scienfific reports. 10 (1), 1–13. https://doi.org/10.1038/s41598-020-65954-6.

Xue, Y., Yang, X., Zheng, C., Chen, C., Gan, H., Li, S., 2019. Lactating sow high-dangerous body movement recognition from depth videos based on hidden Markov model. Transactions of the Chinese Society for. Agricultural Engineering. 35 (13), 184. https://doi.org/10.11975/j.issn.1002-6819.2019.13.021.

Wang, K.e., Guo, H., Ma, Q., Su, W., Chen, L., Zhu, D., 2018. A portable and automatic Xtion-based measurement system for pig body size. Comput. Electron. Agric. 148, 291–298.

Wang, K., Guo, H., Liu, W., Ma, Q., Su, W., Zhu, D., 2017. Extraction method of pig body size measurement points based on rotation normalization of point cloud. Transactions of the Chinese Society of. Agricultural Engineering. 33 (1), 253. https://doi.org/10.11975/j.issn.1002-6819.2017.z1.038.

Wang, K., Liu, C., Duan, Q., 2020. Identification of sow oestrus behavior based on MFO-LSTM. Transactions of the Chinese Society of Agricultural Engineering. 36 (14) https://doi.org/10.11975/j.issn.1002-6819.2020.14.026.

Zhikun, W., Jincheng, Y.u., Ling, Y., Sumin, Z., Yehao, C., Caixing, L., Xuhong, T., 2022. Improved hole repairing algorithm for livestock point clouds based on cubic B-spline for region defining. Measurement 190, 110668. https://doi.org/10.1016/j.measurement.2021.110668.

Xavier, C., Le Cozler, Y., Depuille, L., Caillot, A., Lebreton, A., Allain, C., Delouard, J.M., Delattre, L., Luginbuhl, T., Faverdin, P., Fischer, A., 2022. The use of 3-dimensional imaging of Holstein cows to estimate body weight and monitor the composition of body weight change throughout lactation. J. Dairy Sci. 105 (5), 4508–4519.

Yan, H., Liu, Z., Cui, Q., Hu, Z., Li, Y., 2019. Detection of facial gestures of group pigs based on improved Tiny-TOLO. Transactions of the Chinese Society of Agricultural Engineering. 35 (18), 169–179. https://doi.org/10.11975/j.issn.1002-6819.2019.18.021.

Yin, L., Cai, G., Tian, X., Sun, A., Shi, S., Zhong, H., Liang, S., 2019. Three dimensional point cloud reconstruction and body size measurement of pigs based on multi-view depth camera. Transactions of the Chinese Society of. Agricultural Engineering. 35 (23), 201. https://doi.org/10.11975/j.issn.1002-6819.2019.23.025.

Yu, H., Lee, K., Morota, G., 2021. Forecasting dynamic body weight of non restrained pigs from images using an RGB-D sensor camera. 5 (1), txab006. https://doi.org/10.1093/tas/txab006.

Zhang, J., Zhuang, Y., Ji, H., Teng, G., 2021. Pig Weight and Body Size Estimation Using a Multiple Output Regression Convolutional Neural Network: A Fast and Fully Automatic Method. Sensors 21 (9), 3218. https://doi.org/10.3390/s21093218.

证书号第6221642号

发明专利证书

发 明 名 称：一种牲畜表面点云智能分割方法及其系统

发　明　人：张素敏;尹令;田绪红;刘财兴;蔡更元;吴珍芳

专　利　号：ZL 2021 1 0983285.5

专利申请日：2021年08月25日

专 利 权 人：华南农业大学

地　　址：510642 广东省广州市天河区五山路483号

授权公告日：2023年08月08日　　授权公告号：CN 113724270 B

国家知识产权局依照中华人民共和国专利法进行审查，决定授予专利权，颁发发明专利证书并在专利登记簿上予以登记。专利权自授权公告之日起生效。专利权期限为二十年，自申请日起算。

专利证书记载专利权登记时的法律状况。专利权的转移、质押、无效、终止、恢复和专利权人的姓名或名称、国籍、地址变更等事项记载在专利登记簿上。

局长
申长雨

国家知识产权局
2023年08月08日

其他事项参见续页

证书号第6221642号

专利权人应当依照专利法及其实施细则规定缴纳年费。本专利的年费应当在每年08月25日前缴纳。未按照规定缴纳年费的，专利权自应当缴纳年费期满之日起终止。

申请日时本专利记载的申请人、发明人信息如下：

申请人：

华南农业大学

发明人：

张素敏;尹令;田绪红;刘财兴;蔡更元;吴珍芳

证书号第4632496号

发明专利证书

发明名称：一种基于椭圆拟合的原木板材孔洞缺陷检测与定位方法

发明人：张素敏;尹令;孙爱东;夏玥;王永福

专利号：ZL 2018 1 0260055.4

专利申请日：2018年03月27日

专利权人：华南农业大学

地址：510642 广东省广州市天河区五山路483号

授权公告日：2021年08月24日　　授权公告号：CN 108537153 B

国家知识产权局依照中华人民共和国专利法进行审查，决定授予专利权，颁发发明专利证书并在专利登记簿上予以登记。专利权自授权公告之日起生效。专利权期限为二十年，自申请日起算。

专利证书记载专利权登记时的法律状况。专利权的转移、质押、无效、终止、恢复和专利权人的姓名或名称、国籍、地址变更等事项记载在专利登记簿上。

局长

申长雨

国家知识产权局

2021年08月24日

其他事项参见续页

证 书 号 第 4632496 号

国家税务总局北京市海淀区税务局 印花税 代扣专用章

专利权人应当依照专利法及其实施细则规定缴纳年费。本专利的年费应当在每年 03 月 27 日前缴纳。未按照规定缴纳年费的，专利权自应当缴纳年费期满之日起终止。

申请日时本专利记载的申请人、发明人信息如下：

申请人：

华南农业大学

发明人：

张素敏；尹令；孙爱东；夏玥；王永福

证书号第4375945号

发明专利证书

发明名称：一种基于原木弯曲度的木材切分点定位方法和装置

发明人：张素敏;尹令;刘财兴;田绪红;夏玥

专利号：ZL 2018 1 0973742.0

专利申请日：2018年08月24日

专利权人：华南农业大学

地址：510642 广东省广州市天河区五山路483号

授权公告日：2021年04月23日　　授权公告号：CN 109215019 B

国家知识产权局依照中华人民共和国专利法进行审查，决定授予专利权，颁发发明专利证书并在专利登记簿上予以登记。专利权自授权公告之日起生效。专利权期限为二十年，自申请日起算。

专利证书记载专利权登记时的法律状况。专利权的转移、质押、无效、终止、恢复和专利权人的姓名或名称、国籍、地址变更等事项记载在专利登记簿上。

局长

申长雨

国家知识产权局

2021年04月23日

其他事项参见续页

证 书 号 第 4375945 号

国家税务总局北京市海淀区税务局 印花税 代扣专用章 国家知识产权局

专利权人应当依照专利法及其实施细则规定缴纳年费。本专利的年费应当在每年 08 月 24 日前缴纳。未按照规定缴纳年费的，专利权自应当缴纳年费期满之日起终止。

申请日时本专利记载的申请人、发明人信息如下：

申请人：

华南农业大学

发明人：

张素敏；尹令；刘财兴；田绪红；夏玥

证书号第8415257号

专利公告信息

发明专利证书

发明名称：基于色彩化点云多视角关键点定位的牛只体尺测量方法

专利权人：华南农业大学

地　　址：510642 广东省广州市天河区五山路483号

发 明 人：张素敏;李志坤;彭锦发;尹令;刘庆友;罗西尔

专　利　号：ZL 2024 1 1272041.6　　授权公告号：CN 119380041 B

专利申请日：2024年09月11日　　授权公告日：2025年10月31日

申请日时申请人：华南农业大学

申请日时发明人：张素敏;李志坤;彭锦发;尹令;刘庆友;罗西尔

国家知识产权局依照中华人民共和国专利法进行审查，决定授予专利权，并予以公告。

专利权自授权公告之日起生效。专利权有效性及专利权人变更等法律信息以专利登记簿记载为准。

局长
申长雨

国家知识产权局
2025年10月31日

证书号第7925179号

专利公告信息

发明专利证书

发明名称：一种基于双目光学图像的水下三维全景重构方法和系统

专利权人：华南农业大学

地　　址：510642 广东省广州市天河区五山路483号

发 明 人：张素敏;尹涛;江彦鹏;黄琼;尹令;张足生;古万荣

专　利　号：ZL 2024 1 1469960.2　　授权公告号：CN 119379810 B

专利申请日：2024年10月21日　　授权公告日：2025年05月09日

申请日时申请人：华南农业大学

申请日时发明人：张素敏;尹涛;江彦鹏;黄琼;尹令;张足生;古万荣

国家知识产权局依照中华人民共和国专利法进行审查，决定授予专利权，并予以公告。

专利权自授权公告之日起生效。专利权有效性及专利权人变更等法律信息以专利登记簿记载为准。

局长
申长雨

国家知识产权局
2025年05月09日

证书号第8188991号

专利公告信息

发明专利证书

发明名称：一种牲畜体重测量方法、装置、系统及计算机设备

专利权人：华南农业大学

地　　址：510642 广东省广州市天河区五山路483号

发 明 人：张素敏;彭锦发;李志坤;尹令;田绪红;刘汉兴;吴珍芳
蔡更元

专 利 号：ZL 2023 1 1072245.0　　授权公告号：CN 117281061 B

专利申请日：2023年08月23日　　授权公告日：2025年08月22日

申请日时申请人：华南农业大学

申请日时发明人：张素敏;彭锦发;李志坤;尹令;田绪红;刘汉兴;吴珍芳
蔡更元

国家知识产权局依照中华人民共和国专利法进行审查，决定授予专利权，并予以公告。

专利权自授权公告之日起生效。专利权有效性及专利权人变更等法律信息以专利登记簿记载为准。

局长
申长雨

国家知识产权局
2025年08月22日

证书号第4651762号

发明专利证书

发明名称：一种基于三维曲面的原木直径测算方法

发明人：尹令;张素敏;孙爱东;夏玥;王永福

专利号：ZL 2018 1 0168862.3

专利申请日：2018年02月28日

专利权人：华南农业大学

地址：510642 广东省广州市天河区五山路483号

授权公告日：2021年08月31日　　授权公告号：CN 108428219 B

国家知识产权局依照中华人民共和国专利法进行审查，决定授予专利权，颁发发明专利证书并在专利登记簿上予以登记。专利权自授权公告之日起生效。专利权期限为二十年，自申请日起算。

专利证书记载专利权登记时的法律状况。专利权的转移、质押、无效、终止、恢复和专利权人的姓名或名称、国籍、地址变更等事项记载在专利登记簿上。

局长

申长雨

国家知识产权局

2021年08月31日

其他事项参见续页

证书号第4651762号

国家税务总局北京市海淀区税务局 印花税 代扣专用章 国家知识产权局

专利权人应当依照专利法及其实施细则规定缴纳年费。本专利的年费应当在每年02月28日前缴纳。未按照规定缴纳年费的，专利权自应当缴纳年费期满之日起终止。

申请日时本专利记载的申请人、发明人信息如下：

申请人：

华南农业大学

发明人：

尹令；张素敏；孙爱东；夏玥；王永福

证书号第5106625号

发明专利证书

发明名称：一种区域限定的改进三次B样条插值修补方法

发明人：尹令;温志坤;张素敏;刘财兴;田绪红;蔡更元;吴珍芳

专利号：ZL 2021 1 0897570.5

专利申请日：2021年08月05日

专利权人：华南农业大学

地址：510642 广东省广州市天河区五山路483号

授权公告日：2022年04月26日　　授权公告号：CN 113610726 B

国家知识产权局依照中华人民共和国专利法进行审查，决定授予专利权，颁发发明专利证书并在专利登记簿上予以登记。专利权自授权公告之日起生效。专利权期限为二十年，自申请日起算。

专利证书记载专利权登记时的法律状况。专利权的转移、质押、无效、终止、恢复和专利权人的姓名或名称、国籍、地址变更等事项记载在专利登记簿上。

局长
申长雨

国家知识产权局
2022年04月26日

其他事项参见续页

证 书 号 第 5106625 号

国家税务总局北京市海淀区税务局 印花税 代扣专用章 国家知识产权局

专利权人应当依照专利法及其实施细则规定缴纳年费。本专利的年费应当在每年 08 月 05 日前缴纳。未按照规定缴纳年费的，专利权自应当缴纳年费期满之日起终止。

申请日时本专利记载的申请人、发明人信息如下：

申请人：

华南农业大学

发明人：

尹令；温志坤；张素敏；刘财兴；田绪红；蔡更元；吴珍芳

证书号第5524158号

发明专利证书

发明名称：一种基于深度学习的仔猪乳头计数方法

发明人：尹令;吴振邦;李熙雅;田绪红;张素敏;刘财兴

专利号：ZL 2022 1 0199936.6

专利申请日：2022年03月01日

专利权人：华南农业大学

地址：510642 广东省广州市天河区五山路483号

授权公告日：2022年10月21日　　授权公告号：CN 114550069 B

国家知识产权局依照中华人民共和国专利法进行审查，决定授予专利权，颁发发明专利证书并在专利登记簿上予以登记。专利权自授权公告之日起生效。专利权期限为二十年，自申请日起算。

专利证书记载专利权登记时的法律状况。专利权的转移、质押、无效、终止、恢复和专利权人的姓名或名称、国籍、地址变更等事项记载在专利登记簿上。

局长

申长雨

国家知识产权局

2022年10月21日

其他事项参见续页

证 书 号 第 5524158 号

专利权人应当依照专利法及其实施细则规定缴纳年费。本专利的年费应当在每年 03 月 01 日前缴纳。未按照规定缴纳年费的，专利权自应当缴纳年费期满之日起终止。

申请日时本专利记载的申请人、发明人信息如下：

申请人：

华南农业大学

发明人：

尹令；吴振邦；李熙雅；田绪红；张素敏；刘财兴

证书号第5013997号

发明专利证书

发明名称：一种基于三维重构牲畜体点云的标准姿态鉴定方法

发明人：尹令;张素敏;田绪红;刘财兴;朱纪民;刘汉兴

专利号：ZL 2021 1 0517086.5

专利申请日：2021年05月12日

专利权人：华南农业大学

地址：510642 广东省广州市天河区五山路483号

授权公告日：2022年03月22日　　授权公告号：CN 113516756 B

国家知识产权局依照中华人民共和国专利法进行审查，决定授予专利权，颁发发明专利证书并在专利登记簿上予以登记。专利权自授权公告之日起生效。专利权期限为二十年，自申请日起算。

专利证书记载专利权登记时的法律状况。专利权的转移、质押、无效、终止、恢复和专利权人的姓名或名称、国籍、地址变更等事项记载在专利登记簿上。

局长

申长雨

国家知识产权局

2022年03月22日

其他事项参见续页

证 书 号 第 5013997 号

国家税务总局北京市海淀区税务局 印花税 代扣专用章 国家知识产权局

专利权人应当依照专利法及其实施细则规定缴纳年费。本专利的年费应当在每年 05 月 12 日前缴纳。未按照规定缴纳年费的，专利权自应当缴纳年费期满之日起终止。

申请日时本专利记载的申请人、发明人信息如下：

申请人：

华南农业大学

发明人：

尹令；张素敏；田绪红；刘财兴；朱纪民；刘汉兴

证书号第5725653号

发明专利证书

发明名称：一种牲畜体积计算方法、系统、可读存储介质

发明人：尹令;林润恒;刘财兴;田绪红;张素敏;刘汉兴;蔡更元
叶健

专利号：ZL 2022 1 0412288.8

专利申请日：2022年04月19日

专利权人：华南农业大学

地址：510642 广东省广州市天河区五山路483号

授权公告日：2023年02月03日　　授权公告号：CN 114742880 B

国家知识产权局依照中华人民共和国专利法进行审查，决定授予专利权，颁发发明专利证书并在专利登记簿上予以登记。专利权自授权公告之日起生效。专利权期限为二十年，自申请日起算。

专利证书记载专利权登记时的法律状况。专利权的转移、质押、无效、终止、恢复和专利权人的姓名或名称、国籍、地址变更等事项记载在专利登记簿上。

局长
申长雨

国家知识产权局
2023年02月03日

其他事项参见续页

证 书 号 第 5725653 号

专利权人应当依照专利法及其实施细则规定缴纳年费。本专利的年费应当在每年 04 月 19 日前缴纳。未按照规定缴纳年费的，专利权自应当缴纳年费期满之日起终止。

申请日时本专利记载的申请人、发明人信息如下：

申请人：

华南农业大学

发明人：

尹令；林润恒；刘财兴；田绪红；张素敏；刘汉兴；蔡更元；叶健

W68

中华人民共和国国家版权局

计算机软件著作权登记证书

证书号：软著登字第10019275号

软件名称：基于多传感的全方位牲畜智测系统 V1.0

著作权人：华南农业大学

开发完成日期：2022年05月01日

首次发表日期：2022年05月01日

权利取得方式：原始取得

权利范围：全部权利

登记号：2022SR1065076

根据《计算机软件保护条例》和《计算机软件著作权登记办法》的规定，经中国版权保护中心审核，对以上事项予以登记。

中华人民共和国国家版权局 计算机软件著作权登记专用章

No. 11282217

2022年08月10日

合同编号：

技术转让（专利权）合同

项目名称：基于软激光测距的牲畜体型轮廓重构方法及体况评分方法等 8 个专利

受让方（甲方）：安徽哈泰智能科技有限公司

让与方（乙方）：华南农业大学

签订时间：2024-12-10

签订地点：广州

有效期限：

中华人民共和国科学技术部印制

填 写 说 明

一、本合同为中华人民共和国科学技术部印制的技术转让（专利权）合同示范文本，各技术合同认定登记机构可推介技术合同当事人参照使用。

二、本合同书适用于一方当事人（让与方、原专利权人）将其发明创造专利权转让受让方，受让方支付约定价款而订立的合同。

三、签约一方为多个当事人的，可按各自在合同关系中的作用等，在“委托方”、“受托方”项下（增页）分别排列为共同受让人或共同让与人。

四、本合同书未尽事项，可由当事人附页另行约定，并作为本合同的组成部分。

五、当事人使用本合同书时约定无需填写的条款，应在该条款处注明“无”等字样。

技术转让（专利权）合同

受让方（甲方）：安徽哈泰智能科技有限公司

住所地：安徽省合肥市经济开发区宿松路 3963 号智能装备科技园 A3 栋 20 楼 2004-2006 室

法定代表人：蔡家柱　　项目联系人：蔡家柱

联系方式：[redacted]

通讯地址：安徽省合肥市经济开发区宿松路 3963 号智能装备科技园 A3 栋 20 楼 2004-2006 室

电话：0551-63829661　　传真：0551-63829661

电子信箱：[redacted]1@qq.com

让与方（乙方）：华南农业大学

住所地：广东省广州市天河区五山路 483 号

法定代表人：薛红卫

项目联系人：尹令

联系方式：[redacted]

通讯地址：广东省广州市天河区五山路 483 号数学与信息学院 613

电话：020-85285393　　传真：020-85285393

电子信箱：yin_ling@scau.edu.cn

本合同乙方将其基于软激光测距的牲畜体型轮廓重构方法及体况评分方法，一种基于三维点云牲畜表型体尺数据的自动测量方法，

一种牲畜三维重构移动式设备的自动标定配准方法，一种区域限定的改进三次 B 样条插值修补方法，一种基于三维重构牲畜体点云的标准姿态鉴定方法，一种牲畜表面点云智能分割方法及其系统，一种牲畜体积计算方法、系统、可读存储介质，一种基于深度学习的仔猪乳头计数方法共 8 项专利权转让甲方，甲方受让并支付相应的转让价款。双方经过平等协商，在真实、充分地表达各自意愿的基础上，根据《中华人民共和国民法典》的规定，达成如下协议，并由双方共同恪守。

第一条：本合同转让的专利权包含以下：

1．转让发明专利 1：

1.1 为 基于软激光测距的牲畜体型轮廓重构方法及体况评分方法（发明）专利。

1.2 发明人/设计人为： 尹令，刘财兴，李娇娇，吴贤奇 。

1.3 专利权人： 华南农业大学 。

1.4 专利授权日： 2019-07-19 。

1.5 专利号： ZL201610289390.8 。

1.6 专利有效期限： 2036-05-03 。

1.7 专利年费已交至： 2025-05-03

2．转让发明专利 2：

2.1 为 一种基于三维点云牲畜表型体尺数据的自动测量方法（发明）专利。

2.2 发明人/设计人为： 尹令；钟浩杰；石帅；田绪红；刘财兴；吴珍芳；蔡更元 。

2.3 专利权人：华南农业大学。

2.4 专利授权日：2020-10-23。

2.5 专利号：ZL201911116935.5。

2.6 专利有效期限：2039-11-15。

2.7 专利年费已交至2025-11-15。

3．转让发明专利 3:

3.1 为一种牲畜三维重构移动式设备的自动标定配准方法（发明）专利。

3.2 发明人/设计人为：尹令；石帅；田绪红；刘财兴；吴珍芳；蔡更元；钟浩杰；梁世豪。

3.3 专利权人：华南农业大学。

3.4 专利授权日：2020-08-07。

3.5 专利号：ZL201910964130.X。

3.6 专利有效期限：2039-10-11。

3.7 专利年费已交至2025-10-11。

4．发明专利 4:

4.1 为一种区域限定的改进三次 B 样条插值修补方法（发明）专利。

4.2 发明人/设计人为：尹令,温志坤,张素敏,刘财兴,田绪红,蔡更元,吴珍芳。

4.3 专利权人：华南农业大学。

4.4 专利授权日：2022-04-26。

2.3 专利权人：华南农业大学。

2.4 专利授权日：2020-10-23。

2.5 专利号：ZL201911116935.5。

2.6 专利有效期限：2039-11-15。

2.7 专利年费已交至2025-11-15。

3．转让发明专利 3：

3.1 为一种牲畜三维重构移动式设备的自动标定配准方法（发明）专利。

3.2 发明人/设计人为：尹令；石帅；田绪红；刘财兴；吴珍芳；蔡更元；钟浩杰；梁世豪。

3.3 专利权人：华南农业大学。

3.4 专利授权日：2020-08-07。

3.5 专利号：ZL201910964130.X。

3.6 专利有效期限：2039-10-11。

3.7 专利年费已交至2025-10-11。

4．发明专利 4：

4.1 为一种区域限定的改进三次 B 样条插值修补方法（发明）专利。

4.2 发明人/设计人为：尹令,温志坤,张素敏,刘财兴,田绪红,蔡更元,吴珍芳。

4.3 专利权人：华南农业大学。

4.4 专利授权日：2022-04-26。

4.5 专利号：ZL202110897570.5。

4.6 专利有效期限：2041-08-05。

4.7 专利年费已交至 2025-08-05。

5. 发明专利 5:

5.1 为 一种基于三维重构牲畜体点云的标准姿态鉴定方法（发明）专利。

5.2 发明人/设计人为： 尹令，张素敏，田绪红，刘财兴，朱纪民，刘汉兴。

5.3 专利权人： 华南农业大学。

5.4 专利授权日： 2022-03-22。

5.5 专利号： ZL202110517086.5。

5.6 专利有效期限：2041-05-12。

5.7 专利年费已交至 2025-05-12。

6. 发明专利 6:

6.1 为 一种牲畜表面点云智能分割方法及其系统（发明）专利

6.2 发明人/设计人为： 张素敏,尹令,田绪红,刘财兴,蔡更元,吴珍芳。

6.3 专利权人： 华南农业大学。

6.4 专利授权日： 2023-08-08。

6.5 专利号： ZL202110983285.5。

6.6 专利有效期限：2041-08-25。

6.7 专利年费已交至 2025-08-25。

7. 发明专利 7:

7.1 为 一种牲畜体积计算方法、系统、可读存储介质（发明）专利。

7.2 发明人/设计人为： 尹令，林润恒，刘财兴，田绪红，张素敏，刘汉兴，蔡更元，叶健 。

7.3 专利权人： 华南农业大学 。

7.4 专利授权日： 2023-02-03 。

7.5 专利号： ZL202210412288.8 。

7.6 专利有效期限： 2042-04-19。

7.7 专利年费已交至 2025-04-19 。

8. 发明专利 8:

8.1 为 一种基于深度学习的仔猪乳头计数方法（发明）专利。

8.2 发明人/设计人为： 尹令，吴振邦，李熙雅，田绪红，张素敏，刘财兴 。

8.3 专利权人： 华南农业大学 。

8.4 专利授权日： 2022-10-21 。

8.5 专利号： ZL202210199936.6 。

8.6 专利有效期限： 2042-03-01。

8.7 专利年费已交至 2025-03-01 。

第二条：乙方在本合同签署前实施或许可本项专利权的状况如下:

1．乙方实施本项专利权的状况（时间、地点、方式和规模）：_

只进行项目验证，无使用专利权。

2．乙方许可他人使用本项专利权的状况（时间、地点、方式和规模）：无许可使用专利权。

3．本合同生效后，乙方有义务在3日内将本项专利权转让的状况告知被许可使用本发明创造的当事人。

第三条：甲方应在本合同生效后，保证原专利实施许可合同的履行。乙方在原专利实施许可合同中享有的权利和义务，自本合同生效之日起，由甲方承受。乙方应当在5日内通知并协助原专利实施许可合同的让与人与甲方办理合同变更事项。

第四条：本合同生效后乙方继续实施本项专利的，按以下约定办理：无。

第五条：为保证甲方有效拥有本项专利权，乙方应向甲方提交以下技术资料：

1．专利授权书；

2．权力说明书。

第六条：乙方向甲方提交技术资料的时间、地点、方式如下：

1．提交时间：本合同签署后3日内。

2．提交地点：安徽省合肥市。

3．提交方式：纸质及电子档。

第七条：本合同签署后，由乙方负责在15日内办理专利权转让登记事宜。

第八条：为保证甲方有效拥有本项专利，乙方向甲方转让与实施

本项专利权有关的技术秘密：

1．技术秘密的内容：乙方应向甲方提供转让专利全部技术内容，不得向第三方提供。

2．技术秘密的实施要求：乙方应向甲方提供转让专利全部技术实施要求，不得向第三方提供。

3．技术秘密的保密范围和期限：保密范围为所有专利全部授权技术内容；保密期限为转让专利有效期内。

第九条：乙方应当保证其专利权转让不侵犯任何第三人的合法权益。如发生第三人指控甲方侵权的，乙方应当对其承担法律责任。

第十条：乙方对本合同生效后专利权被宣告无效，不承担法律责任。

第十一条：甲方向乙方支付该项专利权转让的价款及支付方式如下：

1．专利权的转让价款总额为：人民币壹佰万元整（￥1，000,000.00）

2．专利权的转让价款由甲方分期（一次、分期或提成）支付乙方。

具体支付方式和时间如下：

(1)合同生效后 5 个工作日内，支付首批款项人民币贰拾万元整(￥200,000.00)；

(2)专利权人变更为甲方后，甲方收到所有专利后，支付款项叁拾万元整(￥300,000.00)；

(3)2025 年 10 月 1 日前支付剩余款项伍拾万元整(￥500,000.00)。

乙方开户银行名称、地址和账号为:

开户银行: 广州工行五山支行

地址: 广州市天河区五山路 483 号

账号: 3602 0026 0900 0310 520

第十二条:双方确定,在本合同履行中,任何一方不得以下列方式限制另一方的技术竞争和技术发展:

1. 不得限制乙方在该技术领域内文献发表及科研项目申报

2. 不得限制甲方在该专利技术的扩展、迁移和应用

第十三条:双方确定:

1.甲方有权利用乙方转让专利权涉及的发明创造进行后续改进。由此产生的具有实质性或创造性技术进步特征的新的技术成果,归甲方所有。

2.乙方有权在已交付甲方该项专利权后,对该项专利权涉及的发明创造进行后续改进。由此产生的具有实质性或创造性技术进步特征的新的技术成果,归双方所有。

第十四条:双方确定,按以下约定承担各自的违约责任:

1.若因乙方原因提前终止合同,甲方有权要求乙方退还首批价款,对甲方造成损失的,甲方有权向乙方追偿。

2.任何一方违反本合同约定的,还应赔偿对方全部损失。

第十五条:双方确定,在本合同有效期内,甲方指定蔡家柱为甲方项目联系人,乙方指定尹令为乙方项目联系人。项目联系

人承担以下责任:

1．负责对接双方团队完成专利所有权转让事宜

2．负责协调双方团队就专利权的使用和拓展对接相关问题

一方变更项目联系人的，应当及时以书面形式通知另一方。未及时通知并影响本合同履行或造成损失的，应承担相应的责任。

第十六条：双方确定，出现下列情形，致使本合同的履行成为不必要或不可能的，可以解除本合同:

因发生不可抗力和国家政策和法律违背本项专利不可实施情况下，可以解除本合同;

第十七条：双方因履行本合同而发生的争议，应协商、调解解决。协商、调解不成的，确定按以下第 2 种方式处理:

1．提交 广州 仲裁委员会仲裁;

2．依法向人民法院起诉。

第十八条：本合同一式 伍 份，具有同等法律效力。

第十九条：本合同自国家专利行政主管机关登记之日起生效。

甲方: 安徽哈泰智能科技有限公司 (盖章)

法定代表人／委托代理人: (签名)

2024 年 12 月 10 日

乙方: 华南农业大学 (盖章)

法定代表人／委托代理人: (签名)

2024 年 12 月 10 日

印花税票粘贴处：

（此页由技术合同登记机构填写）

合同登记编号：

1．申请登记人：_____

2．登记材料：（1）_____

（2）_____

（3）_____

3．合同类型：_____

4．合同交易额：_____

5．技术交易额：_____

技术合同登记机构（印章）

经办人：

年　　月　　日

"建行杯"“互联网+”
第九届中国国际大学生创新创业大赛 广东省分赛

荣誉证书

吕建达、冯嘉斌、刘婷婷、蔡泽曦、湛紫祺、蒙晓莹、陈科霖、朱易、赖宜余、陈家宝、李浪浪、黄启轩、安春羽、邓远豪、宁冬冬：

你们的项目《五羊开泰-引领南方黑山羊高质量发展新模式》，在第九届中国国际“互联网+”大学生创新创业大赛广东省分赛中荣获

银 奖

指导老师：柳广斌、刘德武、陈永晴、张素敏、黄国胜

特发此证，以资鼓励。

广东省教育厅

二〇二三年九月

蓝桥杯大赛

获奖证书

华南农业大学张素敏：

指导陈志杰荣获第十六届蓝桥杯全国软件和信息技术专业人才大赛广东赛区C/C++程序设计大学B组二等奖，被评为优秀指导教师。

特发此证，以资鼓励。

证书编号：1602058794

证件号码：430181197707183636

工业和信息化部
人才交流中心

蓝桥杯大赛组委会

2025年5月26日

蓝桥杯大赛

获奖证书

华南农业大学张素敏：

指导胡衍科荣获第十六届蓝桥杯全国软件和信息技术专业人才大赛广东赛区C/C++程序设计大学B组二等奖，被评为优秀指导教师。

特发此证，以资鼓励。

证书编号：1602058704

证件号码：430181197707183636

工业和信息化部
人才交流中心

蓝桥杯大赛组委会

2025年5月26日

蓝桥杯大赛

获奖证书

华南农业大学张素敏：

指导骆韵森荣获第十六届蓝桥杯全国软件和信息技术专业人才大赛广东赛区C/C++程序设计大学B组二等奖，被评为优秀指导教师。

特发此证，以资鼓励。

证书编号：1602058650

证件号码：430181197707183636

工业和信息化部
人才交流中心

蓝桥杯大赛组委会

2025年5月26日

蓝桥杯大赛

获奖证书

华南农业大学张素敏：

指导肖楚恒荣获第十六届蓝桥杯全国软件和信息技术专业人才大赛广东赛区C/C++程序设计大学B组二等奖，被评为优秀指导教师。

特发此证，以资鼓励。

证书编号：1602058425

证件号码：430181197707183636

工业和信息化部
人才交流中心

蓝桥杯大赛组委会

2025年5月26日

蓝桥杯大赛

获奖证书

华南农业大学张素敏：

指导郑家俊荣获第十六届蓝桥杯全国软件和信息技术专业人才大赛广东赛区C/C++程序设计大学B组二等奖，被评为优秀指导教师。

特发此证，以资鼓励。

证书编号：1602058410

证件号码：430181197707183636

工业和信息化部
人才交流中心

蓝桥杯大赛组委会

2025年5月26日

蓝桥杯大赛

获奖证书

华南农业大学张素敏：

指导蔡超群荣获第十六届蓝桥杯全国软件和信息技术专业人才大赛广东赛区C/C++程序设计大学B组三等奖，被评为优秀指导教师。

特发此证，以资鼓励。

证书编号：1602058875

证件号码：430181197707183636

工业和信息化部
人才交流中心

蓝桥杯大赛组委会

2025年5月26日

蓝桥杯大赛

获奖证书

华南农业大学张素敏：

指导徐诺宪荣获第十六届蓝桥杯全国软件和信息技术专业人才大赛广东赛区C/C++程序设计大学B组三等奖，被评为优秀指导教师。

特发此证，以资鼓励。

证书编号：1602058450

证件号码：430181197707183636

工业和信息化部
人才交流中心

蓝桥杯大赛组委会

2025年5月26日

荣誉证书

张素敏 同志：

在担任班主任工作期间，认真负责，表现优秀，

荣获华南农业大学信息学院、软件学院 2007 年度

“优秀班主任” 称号，特发此状，以资鼓励。

信息学院党委　软件学院党委

二〇〇八年一月六日